Takeshi Saito

# The effect of trace elements on precipitation in Al-Mg-Si alloys

A transmission electron microscopy study

Takeshi Saito

Doctoral Thesis

Doctoral theses at NTNU, 2014:171

**NTNU**
Norwegian University of
Science and Technology
Faculty of Natural
Sciences and Technology
Department of Physics

**NTNU – Trondheim**
Norwegian University of
Science and Technology

**NTNU**

Takeshi Saito

# The effect of trace elements on precipitation in Al-Mg-Si alloys

A transmission electron microscopy study

Thesis for the degree of Philosophiae Doctor

Trondheim, May 2014

Norwegian University of Science and Technology
Faculty of Natural Sciences and Technology
Department of Physics

**NTNU – Trondheim**
Norwegian University of
Science and Technology

# Abstract

Effects of trace elements on precipitation in Al-Mg-Si alloys have been investigated mainly using transmission electron microscopy in the context of aluminum recycling. Since Cu and Zn are two of the main alloying elements in other aluminum alloy systems, effects of Cu and Zn as trace elements have been focused in this thesis.

Influence of a Cu content of 0.01 wt% and below is negligible on hardness. With this level of Cu content, the precipitation kinetics is not influenced. However, an addition of ~0.1 wt% Cu leads to higher hardness corresponding to a higher number density of shorter precipitates, and an enhanced precipitation kinetics. With low quench rate from solution heat treatment, a double peak hardness is pronounced during isothermal heat treatment and wider precipitation free zones are observed. However, the addition of ~0.1 wt% Cu reduces these effects. While the precipitation sequence in the Al-Mg-Si system does not alter with the addition of ~0.1 wt% Cu, it gives the precipitates a partially disordered structure.

The disordered structure consists of a projected network of ordered Si atomic columns (the Si-network) which is common for all metastable precipitates. Fragments of known metastable precipitates in the Al-Mg-Si(-Cu) alloy system are found in the disordered precipitates. The disordered precipitates arise as a consequence of the Si-network. Cu atoms are found in specific atomic configurations around the Cu atomic columns. The position of Cu atomic columns can be divided into two types depending on the Si-network: 1. in-between the Si-network columns and 2: on the Si network columns. In both cases, Cu is the center in a three-fold rotational symmetry on the Si-network. 10% pre-deformation makes precipitates heterogeneously nucleated along dislocation lines. These precipitates also consist of a disordered structure having the same specific atomic configurations.

Zn additions of 0.1 wt% and below do not have a measurable influence on strength, microstructure or corrosion properties. However, an addition of ~1 wt% Zn slightly increases the hardness and lowers the conductivity during precipitation. This suggests a presence of Zn atoms in solid solution. With this level of Zn content, Zn atoms diffuse during precipitation to make a Zn film on the grain boundaries, leading to high susceptibility of intergranular corrosion. This effect is most pronounced at peak hardness and over-aged conditions.

Additions of ~1 wt% Zn do not alter the precipitation sequence in the Al-Mg-Si system, and no precipitates of the Al-Zn-Mg alloy system are formed. Instead, most precipitates have a disordered structure where Zn atoms are incorporated. It is revealed that the disordered structure consists of the Si-network and atomic configurations around Zn atoms depend on the Si-network. These disordered struc-

tures are similar to the disordered structures in alloys with Cu additions. In the Zn added alloys, however, Zn atomic columns take several different atomic columns compared to Cu atomic columns.

Although most precipitates are disordered, $\beta''$ precipitates can be observed in alloys added ~1 wt% Zn. The mean intensity of one Si site in the $\beta''$ phase is higher than the other Si sites, suggesting partial Zn occupancy. Theoretical calculations based on density functional theory support that this Si site is likely to have Zn incorporation. While simulations of high angle annular dark-field scanning transmission electron microscopy images show an influence of Zn distribution along the $\beta''$ main growth direction, total energy calculations predict a weak Zn-Zn interaction. This suggests that Zn atoms are not clustering, but uniformly distributed along the atomic columns. The Zn incorporation has a weak influence on the $\beta''$ phase where Zn is admitted as a "defect" according to the theoretical studies.

# Acknowledgement

# Preface

This thesis is submitted in partial fulfilment of the requirements for the degree of Ph.D. at the Norwegian University of Science and Technology (NTNU). The doctoral work has been carried out at the Department of Physics, Faculty of Natural Sciences and Technology, NTNU, from April 2011 to April 2014 in The TEM Gemini Centre. Parts of the results in the thesis were obtained during a 3 months visit at the Groupe de Physique des Matériaux (GPM) at the University of Rouen in France.

The thesis is divided into three parts. The first part is a general introduction to aluminum alloys, transmission electron microscopy and other techniques as a background for the papers in the second part. The second part consists of five papers discussing the results. In Paper I and Paper II, effects of Cu as a trace element on precipitation, precipitate microstructure and atomic structure in Al-Mg-Si alloys are discussed with different Cu additions and thermo-mechanical treatments. In Paper III, the detailed precipitate atomic structure is discussed in an alloy with a low Cu addition. In Paper IV, effects of Zn as a trace element on precipitate microstructure and atomic structure in Al-Mg-Si alloys are discussed with different Zn additions. In Paper V, the Zn containing $\beta''$ phase is discussed. The last part states conclusions and outlook. The following is a list of the papers and scientific achievements.

## Publications included in this thesis

- Paper I: <u>T. Saito</u>, C.D. Marioara, J. Røyset, K. Marthinsen and R. Holmestad, "The effects of quench rate and pre-deformation on precipitation hardening in Al-Mg-Si alloys with different Cu amounts", *Materials Science and Engineering A* 609 (2014), 72-79.

- Paper II: <u>T. Saito</u>, S. Muraishi, C.D. Marioara, S.J. Andersen, J. Røyset and R. Holmestad, "The Effects of Low Cu Additions and Predeformation on the Precipitation in a 6060 Al-Mg-Si Alloys", *Metallurgical and Materials Transaction A* 44 (2013), 4124-4135.

- Paper III: <u>T. Saito</u>, C.D. Marioara, S.J. Andersen, W. Lefebvre and R. Holmestad, "Aberration-corrected HAADF-STEM investigation of precipitate structures in Al-Mg-Si alloys with low Cu additions", *Philosophical Magazine* 94 (2014), 520-531.

- Paper IV: <u>T. Saito</u>, S. Wenner, E. Osmundsen, C.D. Marioara, S.J. Andersen, J. Røyset, W. Lefebvre and R. Holmestad, "The effects of Zn on precip-

itation in Al-Mg-Si alloys", *Philosophical Magazine*, in press (2014) DOI: 10.1080/14786435.2014.913819.

- Paper V: T. Saito, F.J.H. Ehlers, W. Lefebvre, D. Hernandez-Maldonado, R. Bjørge, C.D. Marioara, S.J. Andersen, and R. Holmestad, "HAADF-STEM and DFT investigations of the Zn-containing $\beta''$ phase in Al-Mg-Si alloys", Submitted (2014).

In these papers, the listed co-authors have contributed by either experimental work or interpretation of results. All experimental work and simulations have been done by the author with the following exceptions: Some of the TEM images have been taken by C.D. Marioara in Paper II, III, IV, by S. Muraishi in Paper II, and by S. Wenner and E. Osmundsen in Paper IV. The HAADF-STEM images have been taken by W. Lefebvre in Paper III, IV and V. The DFT calculations have been performed by F.J.H. Ehlers in Paper V. The statistical analysis of HAADF-STEM images have been performed by W. Lefebvre and D. Hernandez-Maldonado in Paper V.

## Other publications related to this thesis

- T. Saito, S. Muraishi C.D. Marioara and R. Holmestad, "Effect of low Cu amounts and pre-deformation on the precipitation in Al-Mg-Si alloys", *Proceedings of 13th International Conference on Aluminum Alloys (ICAA13)*, Edited by Hasso Weiland, Anthony D. Rollett and William A. Cassada, TMS (The Minerals, Metals and Materials Society), (2012), 1063-1068.

- T. Saito, S. Muraishi C.D. Marioara and R. Holmestad, "Influence of low Cu amounts in combination with pre-deformation on the precipitate structures in Al-Mg-Si alloys", *Proceedings of 7th International Conference on the Physical Properties and Application of Advanced Materials (ICPMAT 2012)*, Edited by: R. Bjørge, F.J.H. Ehlers and R. Holmestad, NTNU trykk, (2012), 126-129.

- T. Saito, C.D. Marioara, J. Røyset and R. Holmestad, "Influence of low Cu addition on quench sensitivity in Al-Mg-Si alloys", *Advanced Materials Research*, 922 (2014), 616-621.

- T. Saito, W. Lefebvre, C.D. Marioara, S.J. Andersen and R. Holmestad, "Structural investigation of precipitates with Cu and Zn atomic columns in Al-Mg-Si alloys by aberration-corrected HAADF-STEM", *Journal of Physics Conference Series*, in press (2014).

- <u>T. Saito</u>, C.D. Marioara, J. Røyset and R. Holmestad, "Effect of low Cu addition and thermo-mechanical history on precipitation in Al-Mg-Si alloys", *Materials Science Forum*, in press (2014).

## Presentations related to this thesis

- "Effect of low Cu amounts and pre-deformation on the precipitation in Al-Mg-Si alloys", 13th International Conference on Aluminum Alloys (ICAA13), Pittsburg USA, 3rd-7th June (2012). [Talk]

- "Influence of low Cu amounts in combination with pre-deformation on the precipitate structures in Al-Mg-Si alloys", 7th International Conference on the Physical Properties and Application of Advanced Materials (ICPMAT 2012), Trondheim Norway, 17th-20th June (2012). [Poster]

- "Cu and Zn atomic columns of precipitates in Al-Mg-Si alloys investigated by aberration-corrected scanning transmission electron microscopy", Microscopy Conference 2013 (MC 2013), Regensburg Germany, 25th-30th August (2013). [Poster]

- "Investigation of Cu and Zn atomic columns on the precipitates in Al-Mg-Si alloys by aberration-corrected scanning electron microscope", Electron Microscopy and Analysis Group Conference 2013 (EMAG 2013), York UK, 3rd-6th September (2013). [Talk]

- "The effect of low Cu additions on quench sensitivity of an Al-Mg-Si alloy", International Conference on Processing & Manufacturing of Advanced Materials (Thermec 2013), Las Vegas USA, 2nd-6th December (2013). [Poster]

Trondheim, May 2014

Takeshi Saito

斉藤　健

# List of abbreviations

| | |
|---|---|
| **APT** | Atom probe tomography |
| **BF** | Bright-field |
| **CTF** | Contrast transfer function |
| **DF** | Dark-field |
| **DFT** | Density functional theory |
| **EBSD** | Electron backscatter diffraction |
| **EDS** | Energy dispersive X-ray spectroscopy |
| **EELS** | Electron energy loss spectroscopy |
| **EFTEM** | Energy filtered transmission electron microscope/y |
| **FCC** | Face-centered cubic |
| **FFT** | Fast Fourier transform |
| **GP-zone** | Guinier-Preston zone |
| **HAADF** | High angle annular dark-field |
| **HRTEM** | High resolution transmission electron microscope/y |
| **IGC** | Intergranular corrosion |
| **NBD** | Nano beam diffraction |
| **SEM** | Scanning electron microscope/y |
| **SSSS** | Supersaturated solid solution |
| **STEM** | Scanning transmission electron microscope/y |
| **TDS** | Thermal diffuse scattering |
| **TEM** | Transmission electron microscope/y |

# Contents

# Part I

# Introduction

# Chapter 1

# Motivation

What do you think of when you hear the word *aluminum*? Aluminum beverage cans? Aluminum window profiles in your house? Or maybe an air plane? We realize that there are great amounts of aluminum used around us in daily life. This is because aluminum has attractive properties. One of the properties are high strength/weight ratio – *light weight* and *high strength* can be achieved [1]. To achieve the strength, aluminum is generally used in the form of *alloys* – where a few percent of other elements are added, commonly called *aluminum alloys*. Otherwise, pure aluminum is soft and has limited applications. One of the applications of pure aluminum is the 1 Japanese yen coin, see Figure 1.1. The author learned about *the concept of alloys* – thinking about the difference between a pure aluminum coin and an air plane made of aluminum alloys – when he was a child. Depending on the applications, different properties are required and certain aluminum alloys will be optimum.

Al-Mg-Si alloys are one of the aluminum alloys which have medium strength and good formability, and are widely used in industry [1], e.g. for automobile, transportation, building. The strength of Al-Mg-Si alloys can be achieved by formation of nano-sized fine particles called *precipitates* during heat treatment, due to additions of typically up to a total of ~2 wt% Mg and Si. This is called *precipitation hardening* and the alloys are called *age-hardenable*. Properties of the aluminum alloys depend highly on the precipitate microstructure and the atomic structure, which are governed by amounts of the alloy composition and the thermo-mechanical treatment.

Aluminum is *recyclable* – one of the important properties which can create a sustainable society. Recycling of aluminum alloys has attracted much attention due to the great fact that the energy used for recycling is only 5-7 % of its primary production [2, 3]. The use of recycled aluminum has increased with increasing total aluminum usage. During recycling – from scrap to recycled aluminum al-

loys, a certain amount of *trace elements* remains in the recycled aluminum. When using the recycled aluminum to produce secondary alloys, such elements could drastically influence on precipitate microstructure and atomic structure, and consequently strength and other properties of the alloys. In reality, it is difficult to determine the permitted *amounts* of trace elements since the influencing factors are diverse in a process of recycling. Hence, it is important to investigate *how much* of the trace elements influence the precipitate microstructure and atomic structure.

To investigate precipitate microstructure and atomic structure, the transmission electron microscope (TEM) is an important analytical tool, using high energy electrons. The high energy electrons scatter in different ways within a specimen [4], depending on the precipitate microstructure and the atomic structure. Since the scattered electrons can extract great amount of information, TEM enables precipitates to be investigated in details. Recent developments of spherical aberration-corrected TEM instrument can observe precipitates down to the picometer scale. In addition, the scanning TEM technique with a high angle annular dark-field (HAADF) detector is very advantages to investigate precipitates with amounts of other elements since it shows atomic number contrast [5].

The aims of this thesis include investigation of the effects of trace elements on precipitation, precipitate microstructure and precipitate atomic structure in Al-Mg-Si alloys. These are studied mainly by TEM techniques, including spherical aberratoin-corrected HAADF-STEM. Effects of Cu and Zn as trace elements have been investigated since these elements are two of the main alloying elements in other aluminum alloy systems. These are therefore some of the most common trace elements in recycled aluminum. The investigations will help to obtain more fundamental understanding of trace elements in aluminum alloys and can also help for further modelling of microstructure and atomic structure.

This introduction part consists of four chapters giving a general introduction to aluminum alloys and TEM, also including other techniques relevant as a background for the papers given in this thesis. The main part of the thesis consists of five papers in part II.



Figure 1.1: A picture of the 1 Japanese yen coin, made of pure aluminum with a weight of 1 gram. 1 Japanese yen $\approx$ 0.058 Norwegian krone in April 2014. The picture is taken by the author.

# Chapter 2

# Aluminum alloys

What makes aluminum alloys important and attractive? What are the features of aluminum alloys? In this thesis, all work has been done on one type of aluminum alloys, the Al-Mg-Si alloy. This chapter gives an introduction to aluminum alloys and the effects of typical trace elements including current recycling issues.

## 2.1 Alumimum alloys as metallic materials

Aluminum is the most produced "non-ferrous" metal in the world; it is the second most widely used metal after iron [1]. Aluminum has attracted much attention in industry since it started to be produced in 1827 [6]. This is due to the fact that it has strong beneficial properties over various other materials. Why? First of all, aluminum is *light*. Metallic aluminum has a face-centered cubic (FCC) structure and its density is 2.7 g/cm$^3$. It is in fact about three times lighter than iron (7.9 g/cm$^3$). This gives potential replacements of steels in industry. Second, aluminum is *abundant* on the earth in the form of bauxite; it is the third abundant element – about 8% of earth's crust, after oxygen and silicon [1]. There are also many other facts making aluminum attractive: high reflectivity, high electrical and thermal conductivity and high corrosion resistance.

Pure aluminum metal is in fact soft and has a low strength; therefore it has limited applications. However, additions of other elements make it possible to produce aluminum alloys having strength for various applications. Specific strength[1] is strongly required in e.g. automobile and aerospace industries. Furthermore, aluminum alloys have attracted much attention also because they are highly workable and recyclable.

---

[1]Strength divided by its density: strength/weight ratio.

## 2.2    Classification of aluminum alloys

Aluminum alloys are classified into two types: casting and wrought alloys. The casting alloys are produced without any plastic deformation. For wrought alloys, the plastic deformation is involved – "working processes" like hot and cold rolling, extrusion, drawing and forging are done during production. In general, the wrought alloys have higher elongation and strength than casting alloys. Therefore, about 75-80% of the industrial product of aluminum alloys are wrought alloys [7]. At present about 350 wrought alloys are commercially available [1], which are classified into eight types and designated with a four digit number, depending on alloying elements and compositions [8]. Table 2-1 shows the alloy designations based on the classification. The first digit number is decided by the main alloying elements and the following three digit numbers are given depending on alloy compositions.

Table 2-1: Designations of wrought aluminum alloys.

| Designations | Main alloying elements | Age-hardenable |
|---|---|---|
| 1xxx | Al $\geqq$ 99.00% | - |
| 2xxx | Cu | Yes |
| 3xxx | Mn | No |
| 4xxx | Si | No |
| 5xxx | Mg | No |
| 6xxx | Mg and Si | Yes |
| 7xxx | Zn and Mg | Yes |
| 8xxx | Others | - |

Among the series of aluminum alloys, the Al-Mg-Si alloys (6xxx series) have medium strength and good formability, and are mainly used for automotive, transportation and building purposes.

## 2.3    Strengthening mechanisms

What factors make aluminum alloys having strength? In theory, aluminum alloys have a shear strength between 0.9 and 2.62 GPa due to interatomic force (i.e. cohesive force) [9]. It is known that these levels of strength can not be reached in reality because of presence of *defects*. Hence, all strength mechanisms are based on *hindering* the movement of dislocations due to the defects (as well as precipitates in the case of age-hardenable aluminium alloys). There are several factors contributing to strength. Most aluminum alloys are polycrystalline consisting of many grains with different orientations. Grain boundaries are described as planar defects leading to strength. A dislocation is a line defect interacting with other

dislocations, resulting in strength. Vacancies, atoms in solid solution can give strength as point defects. Precipitates also play an important role to impede the movements of dislocations.

**Dislocation-Grain boundary interactions**  Grain boundaries give a strength contribution due to accommodation of accumulated dislocations during their travel from grain to grain. Strength increases with decreasing grain size as given by the well-known Hall-Petch relation [10, 11]:

$$\sigma_{gb} = \sigma_0 + \frac{k_y}{\sqrt{d}} \tag{2.1}$$

where $\sigma_0$ for a materials constant, $k_y$ for strengthening coefficient and $d$ for the average grain size.

**Dislocation-Dislocation interactions**  Dislocation density has a significant contribution, i.e. work hardening, due to interaction of dislocations [12]. An increase in yield strength caused by the dislocations can be expressed as follows:

$$\sigma_{dis} = Gb \sqrt{\rho} \tag{2.2}$$

where $G$ stands for the shear modulus, $b$ for the Burgers vector of the dislocation and $\rho$ for the dislocation density.

**Dislocation-Vacancy, -Solute atom and -Precipitate interactions**  Vacancies and solute atoms are called point defects or "lattice defects" generating local strain fields around themselves in the aluminum matrix [13, 14]. Figure 2.1 shows a schematic illustration of the local strain fields in the aluminum matrix caused by a vacancy and a solute atom. The vacancies create jogs which interact with dislocations [15]. The strain fields around solute atoms depend on the difference in size between the solute atom and the aluminum atom in the matrix [16]. The contribution to strength depends on their concentration which can be described as follows [17, 18]:

$$\sigma_{ss} = \sum_j k_j C_j^{2/3} \tag{2.3}$$

where $C_j$ is the concentration of a specific alloying element in solid solution and $k_j$ is the corresponding scaling factor.

Precipitates in aluminum matrix essentially play the same role – generating local strain fields around themselves in the aluminium matrix, which will be described in the next section. For the age-hardenable aluminum alloys, the precipitates have a significant contribution to the strength.
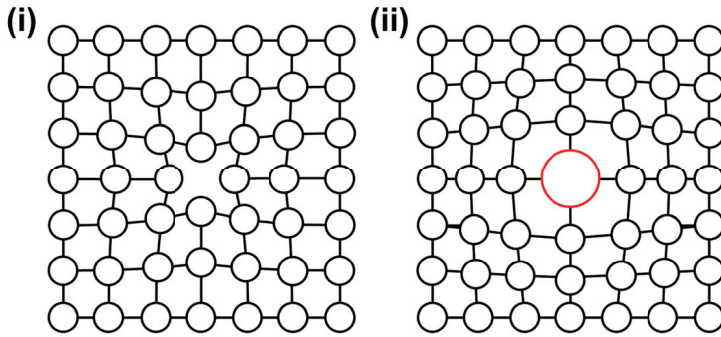
Figure 2.1: The strain fields in the aluminum matrix caused by existences of (i) a vacancy and (ii) a solute atom. Aluminum atoms are drawn in black circles. The vacancy exists in center of (i) and the solute atom is substituted (red circle) in a lattice position in the aluminum matrix in the center of (ii).

In summary, the following factors contribute to strength in aluminum alloys:

- Grain boundaries: $\sigma_{gb}$

- Dislocations (Work hardening): $\sigma_{dis}$

- Solid solution hardening: $\sigma_{ss}$

- Precipitation hardening: $\sigma_{ppt}$

The overall yield strength can be expressed as a sum of these strength contributions linearly with the intrinsic yield strength of pure aluminum $\sigma_i$[2] as follows [19].

$$\sigma_y = \sigma_i + \sigma_{dis} + \sigma_{ss} + \sigma_{ppt} \qquad (2.4)$$

Note that this is one of the plausible approximations, which is not always valid. Different approximations can be found e.g. in Ref. [20].

---

[2]This includes the contribution from grain size.

## 2.4 Precipitation hardening

Precipitation hardening, so called age hardening[3], is one mechanism for achieving strength in aluminum alloys as described above. It was discovered in 1906 by Alfred Wilm in Al-Cu-based alloys – hardness measurements were interrupted over a weekend and he realized the hardening effect [7]. Immediately after the discovery, the application of age-hardenable aluminum alloys started in aircrafts in 1919 [7] although the mechanism was unclear. Precipitates were firstly proven by Gunier and Preston in 1938 by X-ray scattering [21, 22].

The precipitation hardening is caused by formation of nano-sized precipitates consisting of alloying elements. The precipitates form by solid-solid phase transformation – including nucleation and growth – during heat treatments, which will be described in subsection 2.4.1. The precipitates have different crystal structures from the aluminum matrix, which gives strain fields in the matrix around the precipitates. Dislocation-precipitate interactions are complex: they depend on precipitate microstructure, morphology, orientation, size and precipitate/aluminum matrix interface (coherency).

When dislocations interact with precipitates, they move as either *bypassing* or *shearing*, depending on the size of the precipitates [23]. Bypassing results in the formation of a loop (called the Orowan loop [24]) around the precipitate to *store* dislocations. Figure 2.2 shows a schematic illustration of these interactions. Large precipitates are bypassed ("strong" non-shearable) while small ones are sheared ("weak" shearable). In general, we see both types of mechanisms in age-hardenable aluminum alloys.

Although the interactions are complex, contribution from precipitation hardening on yield strength can be estimated, assuming that the precipitates are simple spheres and mechanisms depend on their sizes [19]:,

$$\sigma_{ppt} = \frac{M}{\bar{r}}(2\beta G b^2)\left(\frac{3f}{2\pi}\right)^{1/2} \qquad (2.5)$$

where $M$ is the Taylor factor, $\bar{r}$ is the mean particle size, $G$ is the shear modulus of the aluminum matrix, $b$ is the Burgers vector, $f$ is the volume fraction and $\beta$ is a constant.

When the mean particle radius is smaller than the critical radius for shearing $r_c$, ($\bar{r} \leqq r_c$), the strength contributions become weaker, as follows [19].

$$\sigma_{ppt} = \frac{M}{\bar{r}}(2\beta G b^2)\left(\frac{3f}{2\pi}\right)^{1/2}\left(\frac{\bar{r}}{r_c}\right)^{3/2} \qquad (2.6)$$

---

[3]The hardness evolution occurs by formation of precipitates after "aging".
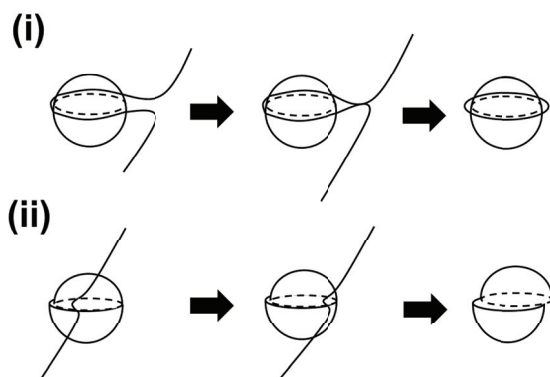
Figure 2.2: Two different mechanisms of dislocation-precipitate interaction, (i) dislocation bypassing to make *a loop* around a precipitate and (ii) shearing a precipitate. The precipitates are illustrated as spheres and dislocations move from left to right in the figure.

Recent development of the strength models could be expanded further to needle-shaped precipitates [25].

Coherency strain is one of the important factors in precipitation hardening. Figure 2.3 shows different structural relations of a precipitate/aluminum matrix interface. *Coherent interfaces* give the highest coherency strain, where the interface has a perfect match between atomic planes of precipitate and aluminum matrix. *Semi-coherent interfaces* have a misfit in the interface between precipitate/aluminum matrix by misfit dislocations. When the interfacial planes have very different atomic configuration, the interface is called *incoherent* which gives lowest coherency strain. The coherency is also important to understand precipitation mechanisms in the age-hardening aluminum alloy, which will be described in the next subsection.

### 2.4.1 Nucleation, clustering and precipitation

The nano-sized precipitates form by solid-solid phase transformations – which include nucleation and growth. A part of a phase diagram for binary aluminum alloys can be used to understand precipitation, and is shown in Figure 2.4. Solubility of alloying elements in aluminum is limited, depending on the elements. When the content of the alloying elements is higher than the solubility, stable phases form to minimize the energy of the system. The following is happening when hardening precipitates are formed: The alloy is solution heat treated at a high temperature,
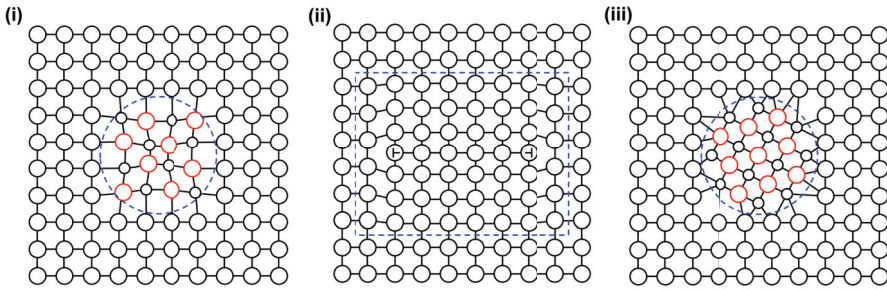
Figure 2.3: Structural relations of precipitate/aluminum matrix interface for (i) coherent interface, (ii) semi-coherent interface and (iii) incoherent interface. The blue dashed circles and rectangle represent these interfaces. The precipitate structure in (iii) is arbitrary chosen.

above the solvus temperature but below the melting temperature in point 1 in Figure 2.4. This point is in the single phase ($\alpha$ phase) region, which means that the alloying elements are in solid solution. Then, when the alloy is rapidly cooled (quenched) to the two phase region (from point 1 to point 2 in Figure 2.4), the alloying elements are in a state of non-equilibrium supersaturated solid solution (SSSS) [26]. In this process, a high number density of vacancies are created, called *quenched-in vacancies*. The alloying elements in the SSSS diffuse via the presence of the quenched-in vacancies to form the precipitates [27]. When temperature increases (from point to 2 to 3 in Figure 2.4), the precipitation is enhanced, and this is called *artificial aging*. The precipitation is controlled not only by thermodynamics, but also kinetics. The following gives a description of nucleation, clustering and growth of precipitates.

**Nucleation and clustering** In the beginning of precipitation, solute atoms diffuse to form solute rich region called *atomic clusters* which will be "nuclei" for nucleation. Solute atoms join the nuclei to grow a cluster. The growth of clusters occurs by statistical fluctuations toward the critical size of nucleation or dissolves to individual atoms [27]. The nucleation is driven by a negative free energy change. However, the growth is determined by two simultaneous opposing forces [26, 27]: matrix interfacial energy[4] and volume free energy. The interfacial energy varies due to change in crystal structure and/or composition of the nuclei from the surrounding aluminum matrix, which varies as a power of two of the size of the nuclei [26, 27]. On the other hand, volume free energy develops when the average vol-

---

[4]Here, strain energy due to coherency is neglected.
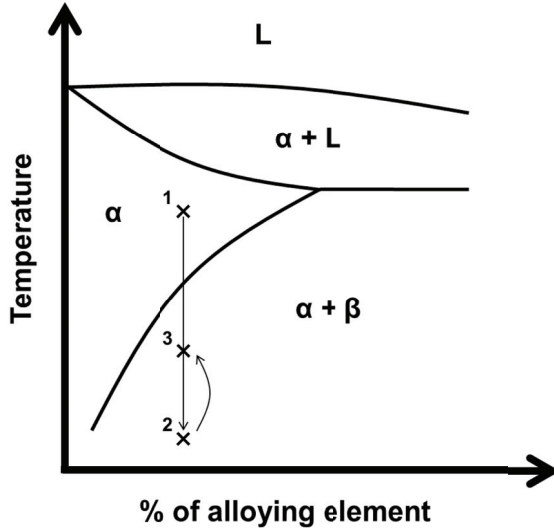
Figure 2.4: An example of a phase diagram for binary aluminum alloys. In the $\alpha$ region, the alloying elements are homogeneously distributed in the solid solution. The solubility depends on the alloying elements. When the alloy contains more than the solubility of a certain element, stable phases ($\beta$) form to minimize the energy.

ume per atom in the nuclei differs from that in the matrix, resulting in elastic strain energy, which varies as a power of three of the size of the nuclei [26, 27]. If we assume that the nuclei has a form of a sphere, total free energy change associated with the nucleation can be expressed as follows [26]:

$$\Delta G_{total} = -\frac{4}{3}\pi r^3 \Delta G_v + 4\pi r^2 \gamma \qquad (2.7)$$

where $\Delta G_{total}$ stands for the free energy change, $r$ for the radius of the sphere and $\gamma$ for the interfacial strain. Figure 2.5 shows the free energy change as a function of the size of the nuclei. The $r^*$ is known as *critical radius* where $\Delta G_{total} = \Delta G^*$ in Figure 2.5. When the size of the nuclei is larger than a critical size ($r > r^*$), the influence of the interfacial energy is minimized and the growth stage can be started.

In reality, nucleation is almost always heterogeneous [26]. This means that it preferentially occurs at non-equiblium sites such as defects, which decrease the total free energy of nucleation ($\Delta G^*$). Typical nucleation sites are [26]:
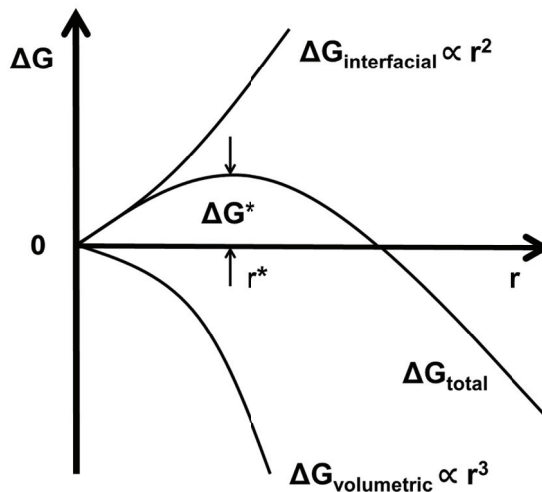
Figure 2.5: The free energy change associated with nucleation as a fuction of size of nuclei. This figure is adapted from Ref. [26, 27].

- Vacancies

- Dislocations

- Stacking faults

- Grain boundaries

- Interphase boundaries

**Precipitate growth** Precipitation is formation of *a phase* that differs in crystal structure and composition from the aluminum matrix by nucleation and growth. It consists of long-range diffusion of solute atoms [27]. In the precipitation sequence, *metastable precipitate phases* – the phases do not exist in the equilibrium phase diagram – initially form instead of equilibrium phase. This is because formation of the equilibrium phase is limited due to its high interface energy[5]. [27]. Equilibrium phases have usually high interface energy because they have incoherent interfaces, while metastable phases have (semi-)coherent interfaces as described in Figure 2.3. The (semi-)coherent interface has lower interface energy

---

[5]Interface energy consists of chemical interfacial energy (related to atomic types) and strain energy (related to coherency).

and the kinetic barrier can easily be overcome. At higher temperature, the precipitation is enhanced because the atomic diffusivity increases. Hence, the precipitates grow and equilibrium phases form eventually since the volume free energy is large enough to stabilize them. The diffusivity depends on the alloying elements. For example, in FCC aluminum matrix, the diffusivity $D$ for Si, Mg and Cu are $D_{Si} > D_{Mg} > D_{Cu}$ [28, 29]. There are higher diffusivity regions than the aluminum lattice [26]: for example, grain boundary and dislocation are considered to be high diffusivity paths.

### 2.4.2   Heat treatment

Heat treatment is essential to achieve precipitate microstructure for desired properties in age-hardenable aluminum alloys. A typical heat treatment involves the following steps:

- Solution heat treatment

- Quenching

- Natural aging

- Artificial aging

These heat treatment steps correspond to precipitation processes described in section 2.4.1. Natural aging means storage at room temperature. This reflects the industrial practice and involves e.g. transportation time from one process step to another. Nucleation and clustering occur even at room temperature since the SSSS is far from the stable equilibrium phase [7]. Figure 2.6 shows a typical heat treatment history for age-hardenable aluminum alloys.

## 2.5   Precipitation in Al-Mg-Si alloys

Al-Mg-Si alloys consists of a total amount of 1-2wt% of solute elements (Mg, Si) for forming precipitates. In addition, other elements are present in commercial industrial alloys such as Mn, Cr, Fe and Ti. These elements are added to form dispersoids to prevent recrystallization or grain growth after recrystallization [1, 30, 31].

A series of metastable precipitates are encountered during precipitation. All precipitates in the Al-Mg-Si alloys grow and keep the alignment (fully coherent) in <001> Al which is the main growth direction. As a consequence, they have needle/lath/rod morphologies extending along <001>Al. The precipitation is
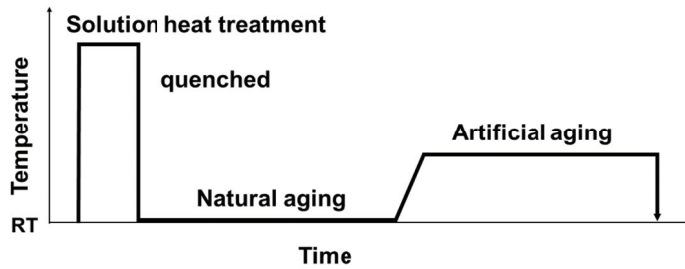
Figure 2.6: A typical heat treatment history for age-hardenable aluminum alloys, corresponding to the precipitation processes described in section 2.4.1. See also Figure 2.4. "RT" represents room temperature.

complex, depending on alloy compositions, vacancy concentrations, quench rate, natural aging time, artificial aging time/temperature/steps and deformation before artificial aging[6]. These factors influence each other and affect the precipitation in Al-Mg-Si, giving the complexity.

### 2.5.1 Precipitation sequence

The precipitation sequence of Al-Mg-Si alloys is as follows:

SSSS →atomic clusters →GP-zones (pre-$\beta$") →$\beta$" →$\beta$', U1, U2, B' →$\beta$, Si.
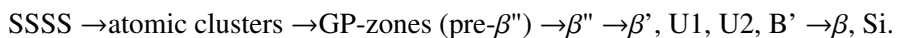
where SSSS and atomic clusters are described in subsection 2.4.1. The following describes these metastable phases and a structural overview is summarized in Figure 2.7 and Tables 2-2 and 2-3.

**GP-zones (pre-$\beta$")** This is an abbreviation of Guinier-Preston (GP) zones. In the early stage of precipitation, GP-zones form. These are sometimes called a precursor of the $\beta$" phase. They are coherent, needle like solute clusters occupying the aluminum FCC position with own crystal structure, which is close to $\beta$" [32, 33]. GP-zones are closely connected to atomic clusters and $\beta$" in the precipitation sequence. The Mg and Si ratio is close to 1 [32, 34, 35] and compositions could be dynamically fractionated in a range from $Mg_2Al_7Si_2$ to $Mg_{2+x}Al_{7-x-y}Si_{2+y}$ (1<x, y<3), depending on Mg/Si ratio [36].

---

[6]This is called *pre-deformation*.

$\beta$**" phase**    This is the main hardening precipitate phase in addition to GP-zones. $\beta$" is highly-coherent and needle shaped, forming the finest microstructure at peak hardness condition. The model of the crystal structure was firstly proposed by Andersen et al. [37, 38], showing monoclinic C-centred unit cell. The composition of the phase has been controversial. In the beginning, it was thought to be $Mg_5Si_6$ for various reasons: for example, alloys with Mg/Si ratio ~5/6 show the highest strength and it was supported by EDS quantification [38]. However, recent extensive studies proposed [39–42], by APT and/or DFT, that the composition varies with substitution of Al on Mg and/or Si sites. These results suggest that the Mg/Si ratio is close to 1.1, which favours $Mg_5Al_2Si_4$, $Mg_4Al_3Si_4$ or $Mg_6Al_1Si_4$. The most recent report [43] suggests that the $\beta$" phase could have compositional variation within a single precipitate.

**Post-$\beta$" phases**    These form after peak hardness, in over-aged condition, with rod-shaped morphology and are less coherent than the $\beta$" phase. They give less strength to the materials. The $\beta$' has a hexagonal unit cell [44–46] with a Mg/Si ratio close to 1.8 [45, 46]. The U1 phase has a hexagonal unit cell with the stoichiometry $MgAl_2Si_2$ [47, 48]. This phase is also known as Type A [45, 49]. The U2 phase has an orthorhombic structure [50], and the atomic configuration is similar to a part of the $\beta$" phase. The U2 phase is also known as Type B [45, 51]. The B' preferentially precipitates along dislocation lines [52], and has a hexagonal structure [53, 54]. The B' is also known as Type C [45]. The $\beta$ is the equilibrium phase and has an incoherent interface.

### 2.5.2   Effects of alloy compositions and other alloying elements

The alloy composition greatly influences the precipitate microstructure and types. While "Si-rich" alloys (Si/Mg ~6/5) make the $\beta$" phase stable, "Mg-rich" ones a coarse[7] precipitate microstucutre and the post-$\beta$" phases are developed in addition to the $\beta$" phase in the peak hardness condition [55]. Although clustering is boosted during natural aging [56], the type of clusters formed during natural aging decides the final precipitate types [57, 58]. The type of clusters depends on alloy composition, e.g. Mg + Si < 1 wt% makes clusters boosting a subsequent formation of precipitates during artificial aging while Mg + Si > 1 wt% makes a retarded development [59]. This is also correlated to natural aging time [60] and does significantly affect the strength of the alloy [61].

Effects of additional alloying elements in the Al-Mg-Si system are of key interest since they directly affect the precipitate microstructure and types. Some

---

[7]Here, "coarse" means that precipitates have longer length and larger cross section – not related to a grain size.

alloying elements are trapped in quenched-in vacancies and will retard cluster formation, while some act as effective nucleation cites for clustering [62]. In this thesis, effects of low amounts of selected additional alloying elements (Cu and Zn) are discussed, and work concerning this is described in Paper I, Paper II, Paper III and Paper IV.

The following gives overview of the effects of each alloying element. A structural overview is summarized in Figure 2.7 and Tables 2-2 and 2-4.

**Effects of Cu**    Additions of Cu (~0.4 wt%) increase strength of Al-Mg-Si alloys [63–65] by formation of a fine microstructure [66, 67]. In addition, it enhances precipitation kinetics [65, 67, 68]. Furthermore, if Cu ~0.4 wt% is added, it drastically alters the precipitation sequences in Al-Mg-Si alloys [69, 70]:

SSSS →atomic clusters →GP-zones (pre-$\beta$") →$\beta$", C, L, QP, QC →$\beta$', Q' →Q.

This shows that the formation of $\beta$" is suppressed, and other metastable precipitates such as C, L, QP, QC, Q' form at peak aged conditions.

The C phase has a plate like morphology with elongation along <001> and habit plane <100> determined by NBD and DFT [71]. The L phase has a lath morphology and a disordered structure [70], and displays strong compositional variations [72]. It is believed to be a precursor of the Q' phase. A recent study revealed that the disordered L precipitates lead to good thermal stability in alloys [73]. The QP and QC phases have been claimed to be hexagonal [74], but details are unknown. The Q' phase forms in over-aged conditions [70]. This phase is isostructural to B' [75, 76]. Q is the equilibrium phase.

**Effects of Ag**    Additions of Ag (~0.5 wt%) in Al-Mg-Si alloys lead to accelerated precipitation kinetics [77], and consequently an increase in strength and elongation [78] by means of a new Ag containing phase, called the $\beta$'$_{Ag}$ phase where Ag replaces one third of the Si columns [79, 80], see Figure 2.7. A combination of Ag and Cu is reported to give further improvements of mechanical properties and precipitation hardening response [81]. A recent report shows that precipitates in Al-Mg-Si-Cu-Ag alloys consist of Cu-rich and Ag-rich areas in a single precipitate, however interestingly Cu and Ag are not found to intermix [82].

**Effects of Ge**    Si can be replaced by Ge to make the Al-Mg-Ge alloy system. In these alloys the precipitation kinetics and mechanical properties are similar to that of the Al-Mg-Si alloys [83, 84]. However, the replacement leads to formation of Ge containing hardening phases which are isostructural with the $\beta$' and U1 phases while the main hardening phase, $\beta$", is not formed [85–87]. It was found that Ge

forms a network similar to the Si-network (See subsection 2.5.3) [88, 89]. When both elements are present in the alloys, the network columns are mixed (Si/Ge) [90].

**Effects of Ca**  Addition of Ca has negative influence of precipitation hardening. It lowers the precipitate number density by formation of large Ca-containing particles which absorb Si [91]. This reduces the amounts of Si *available* for precipitation.

**Effects of Zn**  Zn is the main alloying element in Al-Zn-Mn alloys (7xxx series). In this system, Zn atoms combine with Mg to form plate-like semi-coherent $\eta$' metastable precipitates and equibrium $\eta$-$MgZn_2$ precipitates on {111}Al planes [92–94]. These alloys have very low Si content. Knowledge of effects of Zn on precipitation in Al-Mg-Si alloys is limited. This is one of the main topics in this thesis, which will be discussed in Paper IV and Paper V.
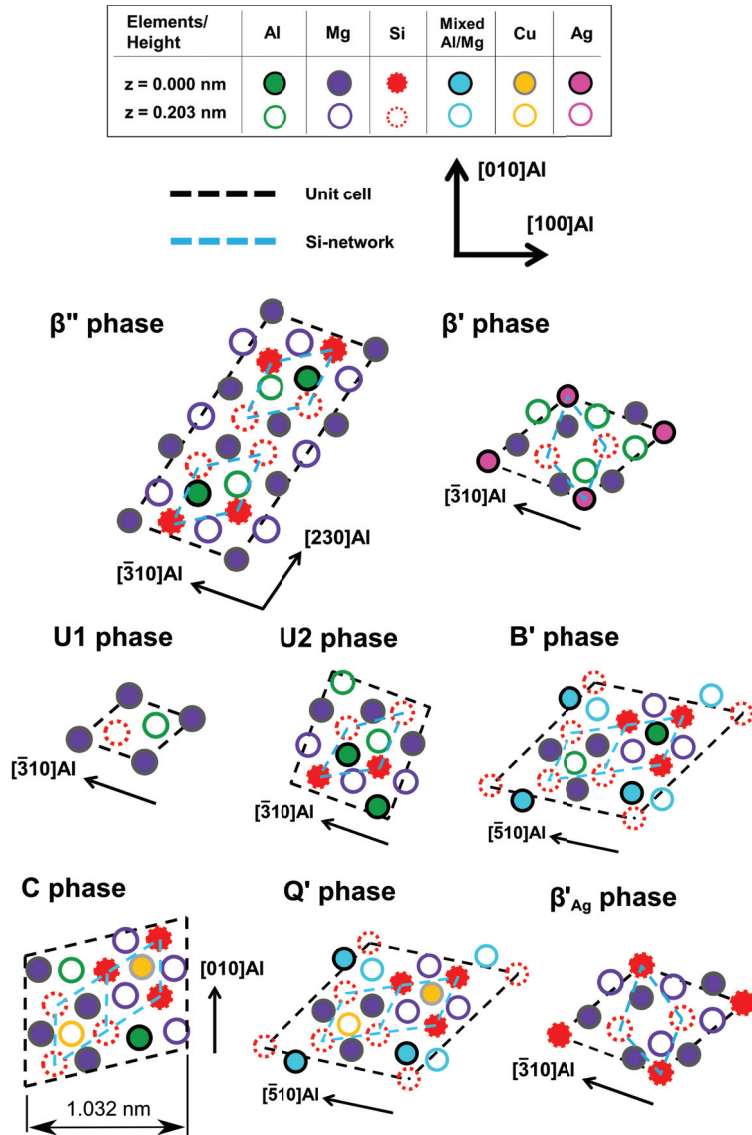
Figure 2.7: Structural models of metastable precipitate phases in Al-Mg-Si(-Cu, -Ag) alloys drawn to the same scale. The composition of the $\beta''$ phase given is the one mostly suggested [39–42] – $Mg_5Al_2Si_4$. The Si-network is a structural similarity in all metastable phases in the Al-Mg-Si alloy system, see subsection 2.5.3. This figure is partially adapted from Ref. [95, 96].

Table 2-2: Precipitate phases encountered in Al-Mg-Si(-Cu, -Ag) alloys.

| Alloys | Phases | Compositions | Space groups | Lattice parameters [nm] |
|---|---|---|---|---|
| Al-Mg-Si | GP-zones[32–36] | Fluctuated | *C2/m* | a = 1.48, b = 0.405, c = 0.648, $\beta$ = 105.3° |
| | $\beta$"[37–42] | $Mg_{6-x}Al_{1+x}Si_4$ (x=0,1,2) | *C2/m* | a = 1.516, b = 0.405, c = 0.674, $\beta$ = 105.3° |
| | $\beta$'[44–46] | $Mg_{1.8}Si$ | $P6_3/m$ | a = b = 0.715, c = 0.405, $\gamma$ = 120° |
| | U1[47, 48] | $MgAl_2Si_2$ | $P\bar{3}m1$ | a = b = 0.405, c = 0.674, $\gamma$ = 120° |
| | U2[48, 50] | MgAlSi | *Pnma* | a = 0.675, b = 0.405, c = 0.794 |
| | B'[45, 53, 54] | $Mg_9Al_3Si_7$ | Hexagonal | a = b = 1.04, c = 0.405, $\gamma$ = 120° |
| | $\beta$[97] | $Mg_2Si$ | $Fm\bar{3}m$ | a = 0.635 |
| Al-Mg-Si-Cu | C[70, 71] | $Mg_4AlSi_{3.3}Cu_{0.7}$ | $P2_{1}/m$ | a = 1.032, b = 0.405, c = 0.810, $\beta$ = 100.9° |
| | L[69, 70] | Fluctuated | Disordered | - |
| | QP[74] | Unknown | Hexagonal | Unknown |
| | QC[74] | Unknown | Hexagonal | Unknown |
| | Q'[69, 75] | $Al_3Cu_2Mg_9Si_7$ | $P\bar{6}$ | a = b = 1.032, c = 0.405, $\gamma$ = 120° |
| | Q[98] | $Al_3Cu_2Mg_9Si_7$ | $P\bar{6}$ | a = b = 1.039, c = 0.405, $\gamma$ = 120° |
| Al-Mg-Si-Ag | $\beta$'$_{Ag}$ [79, 80] | $Mg_3Al_3Si_2Ag$ | $P\bar{6}2m$ | a = b = 0.690, c = 0.405, $\gamma$ = 120° |

Table 2-3: Atomic positions of each metastable precipitate phase in Al-Mg-Si alloys[8], see schematic illustrations in Figure 2.7.

| Alloys | Phases | Atomic positions | | | |
|---|---|---|---|---|---|
| | | Atoms | x | y | z |
| Al-Mg-Si | β"[39] | Mg1 | 0 | 0 | 0 |
| | | Mg2 | 0.3419 | 0 | 0.099 |
| | | Mg3 | 0.4225 | 0 | 0.659 |
| | | Si1 | 0.0501 | 0 | 0.678 |
| | | Si2 | 0.1876 | 0 | 0.225 |
| | | Si3/Al | 0.2213 | 0 | 0.618 |
| | β'[46] | Mg1 | 0.5969 | 0.6807 | 1/4 |
| | | Mg2 | 0.651 | 0.725 | 1/4 |
| | | Si1 | 0 | 0 | 0.346 |
| | | Si2 | 2/3 | 1/3 | 1/4 |
| | U1[47] | Mg | 0 | 0 | 0 |
| | | Al | 1/3 | 2/3 | 0.6334 |
| | | Si | 1/3 | 2/3 | 0.2463 |
| | U2[50] | Mg | 0.056 | 0.25 | 0.689 |
| | | Al | 0.13 | 0.25 | 0.064 |
| | | Si | 0.25 | 0.25 | 0.375 |
| | B'[54] | Mg1 | 0.2559 | 0.0058 | 1/4 |
| | | Mg2 | 0.6297 | 0.1453 | 1/4 |
| | | Al1 | 0.2179 | 0.0066 | 1/4 |
| | | Al2 | 1/3 | 2/3 | 1/4 |
| | | Si1 | 0 | 0 | 1/4 |
| | | Si2 | 0.5876 | 0.8695 | 1/4 |

---

[8]The atomic positions of GP-zones are similar to those of β", except that the y position of Mg1 is 1/2[33].

Table 2-4: Atomic positions of each metastable precipitate phase in Al-Mg-Si-Cu, -Ag alloys, see schematic illustrations in Figure 2.7.

| Alloys | Phases | Atomic positions | | | |
|---|---|---|---|---|---|
| | | Atoms | x | y | z |
| Al-Mg-Si-Cu | C[71] | Mg1 | 0.615 | 0 | 0.03 |
| | | Mg2 | 0.615 | 0 | 0.53 |
| | | Mg3 | 0.925 | 0 | 0.36 |
| | | Mg4 | 0.925 | 0 | 0.86 |
| | | Al | 0.741 | 0.5 | 0.763 |
| | | Si1 | 0.5 | 0.5 | 0.25 |
| | | Si2 | 0.83 | 0.5 | 0.08 |
| | | Si3 | 0.83 | 0.5 | 0.58 |
| | | Cu | 0.703 | 0.5 | 0.355 |
| | Q'[76] | Al1/Mg1 | 0.233/0.207 | 0.985/0.005 | 0 |
| | | Al2/Mg2 | 0.6221 | 0.1292 | 0 |
| | | Si1 | 0 | 0 | 0 |
| | | Si2 | 0.5858 | 0.8653 | 0 |
| | | Cu/Al | 0.333 | 0.667 | 0 |
| Al-Mg-Si-Ag | $\beta'_{Ag}$[80] | Mg | 0.40 | 0.40 | 0 |
| | | Al | 0.74 | 0.74 | 1/2 |
| | | Si | 1/3 | 2/3 | 1/2 |
| | | Ag | 0 | 0 | 0 |

### 2.5.3   Structural similarities and the Si-network

It has been discovered [47, 70] that all metastable precipitate phases in the Al-Mg-Si alloy system are structurally connected through a common network of Si atomic columns (called the *Si-network*). The Si-network has a projected near hexagonal symmetry of a = b ≈ 0.4 nm, c = n × 0.405 nm (n is integer), with c being parallel to the needle/rod/lath direction, i.e. <001> aluminum, see Figures 2.7. The network is also present in the equilibrium Q phase in the Cu containing system. Therefore, all precipitates can be understood as stacks of elemental columns in a <001> aluminum. They have just different arrangements of Al, Mg (and Cu) atomic columns situated in-between the triangularly arranged (approximately 0.4 nm spaced) columns forming the Si-network. When this *column* arrangement is periodic, the precipitates are characterized by a well-defined unit cell. However, although the Si-columns appear triangularly arranged and periodic in projection, it has been demonstrated that the overall arrangement *on the network* can be nonperiodic in many metastable precipitates, leading to a disordred structure without a unit cell [70]. An exception from the above is the $\beta''$ phase, which has a *distorted* Si-network, see Figure 2.7. The distortion is probably attributed to the coherency with the aluminum matrix. As a result, the column arrangement of the Si-network forms locally square symmetry approaching the aluminum unit cell, although a triangular Si-network exists over part of the phase.

### 2.5.4   Effect of heat treatment

As mentioned, the precipitation in Al-Mg-Si alloys is complex. Heat treatment greatly influences the precipitation and the precipitate structure. In Paper I and Paper II, effects of quench rate and/or pre-deformation[9] are discussed in connection to the effect of trace elements. The following is a brief description of these effects.

**Effects of quench rate**   Quenching after solution heat treatment produces quenched-in vacancies which are essential for atomic diffusion during precipitation [99–102] as generally described in section 2.4.1. Slower quench rates lead to decreased supersaturation resulting in loss of vacancies [103] and consequently lower number density of precipitates [104] and lower strength [105].

**Effects of pre-deformation**   It is known that pre-deformation affects atomic diffusion during precipitation because of the introduced dislocations act as high-diffusivity paths [26] as described in section 2.4.1. Nucleation rates and precipi-

---

[9]Since the deformation is conducted before the artificial aging (after the solution heat treatment), it is called "pre-deformation".

tation kinetics are enhanced since the pre-deformation decreases the activation energy for growing precipitates [106, 107]. 10%-15% pre-deformation leads to formation of heterogeneous nucleation sites along dislocation lines. Different types of precipitates, except from $\beta''$, form a continuous decoration of the dislocation lines ("a string-like" precipitates) together with discrete precipitation along dislocation lines consisting mainly of B' [108–111], together with Q' [112, 113] if Cu is present in the alloys. With 0.5%-5% pre-deformation, on the other hand, $\beta''$ is dominant at peak hardness condition. This level of pre-deformation accelerates formation of $\beta''$ due to decreased activation energy [114–117]. This is because the pre-deformation leads to formation of atomic clusters transforming to $\beta''$ during natural aging [118].

## 2.6   Recycling and trace elements

Aluminum recycling has in recent years become a noteworthy activity in industry for a *sustainable society*. The demand for aluminum recycling is supported by the fact that the energy used for recycling is only 5-7% of its primary production [2, 3] and approximately 75% of the aluminum ever produced is still in use all over the world [2]. Based on this enormous energy saving and life time of aluminum, aluminum is called an "energy bank". The use of recycled aluminum has increased with increasing total aluminium usage, as shown in Figure 2.8 (i). Figure 2.8 (ii) and (iii) show the end-use market for finished aluminum products and the origin of recycled aluminum in 2007. Aluminum in transport (e.g. automotive parts) and packaging (e.g. beverage cans) contribute the most to aluminum recycling. For example, collection rate of beverage cans in 2009 was 92.0% in Norway [119], and interestingly they can be recycled, re-fabricated and put back on the supermarket in just ~60 days after collection [2].

The upper part of Figure 2.9 shows a brief description of the total aluminum cycle. In primary production, bauxite (hydrated forms of aluminum oxide) is refined to alumina ($Al_2O_3$). Aluminum is produced from the alumina by electrolysis [1, 120]. This provides aluminum ingots to produce end products. After life time of the products, it is recycled. In recycling, aluminum scrap consists of two types: *pre*-consumer scrap (also called "new scrap") and *post*-consumer scrap ("old scrap"). The former comes from the production process, while the latter comes from products after life-time usage. Today the global aluminum recycling is based on pre-consumer scrap (~32.8 Mt), which is roughly three times more than post-consumer scrap (~10 Mt) [121].

Scrap aluminum contains trace elements, and hence such elements inevitably remain in the recycled secondary aluminum. Since properties of aluminum alloys are generally sensitive to composition, controlling the content of trace elements is

important when making secondary aluminum from aluminum scrap during recycling. A list of such trace elements is quite large, including Si, Mg, Ni, Zn, Pb, Cr, Fe, Cu, V and Mn [122]. Some of these elements directly influence precipitation and precipitate structures in Al-Mg-Si alloys, as mentioned in the above sections.

Aluminum recycling – the whole process from scrap to secondary aluminum – consists of mainly two processes: physical separation and chemical separation. The former one is a pre-melt process after collecting the scrap and the latter one is a melt process to make secondary aluminum. The bottom part of Figure 2.9 shows a brief description of the recycling process and removal of possible elements for each process. The physical separation can roughly remove elements contained in the scrap. Chemical separation includes melting and refinement, metallurgical processes, which further remove elements that cannot be removed in the physical separation by e.g. common fluxing [122].

An important question is *the amounts of* trace elements that accumulate during recycling and will be contained in the secondary alloys. Although an estimation of chemical composition has recently been analysed, e.g. for alloys in the automobile industry [123], it is difficult to predict this value since it depends on aluminum scrap sources, the end products produced by the secondary aluminum and the recycling processes (which usually depend on the aluminum scrap source and the end products) [124–126] – the factors are *diverse*. Moreover, because of the variety of affecting factors, so called "recycling friendly alloys" have been developed. These make it easy to estimate the chemical composition of its secondary alloys and hence will be easily recyclable [3]. In this thesis, effects of selected trace elements (Cu and Zn) on precipitation hardening and precipitate structures are systematically investigated, since these elements are two of the main alloying elements in other aluminum alloy system (2xxx and 7xxx series, respectively). These are described in Paper I, Paper II, Paper III and Paper IV.
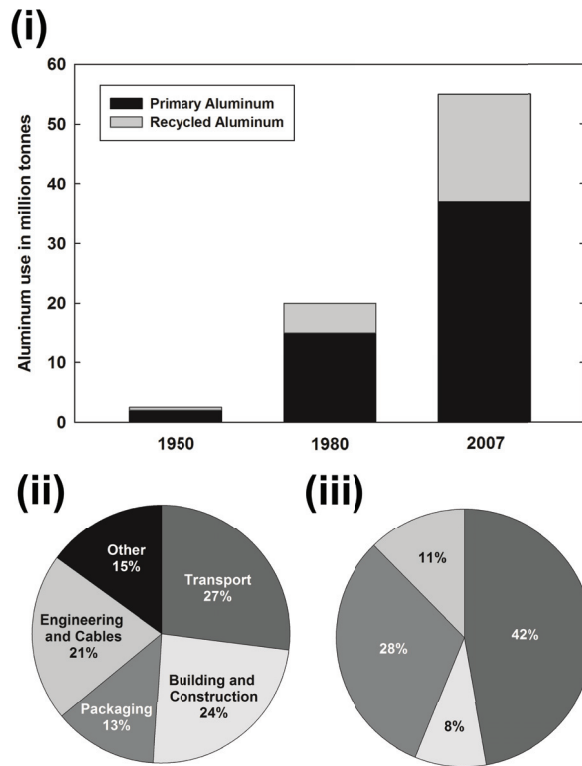
Figure 2.8: (i) Global aluminum use in 1950, 1980 and 2007 for primary aluminum and recycled aluminum, (ii) the end-use market of finished aluminum products in 2007 and (iii) origin of recycled aluminum produced from old scrap in 2007. Data are from Ref. [119]. The gray scale for each category in (iii) corresponds to that in (ii).
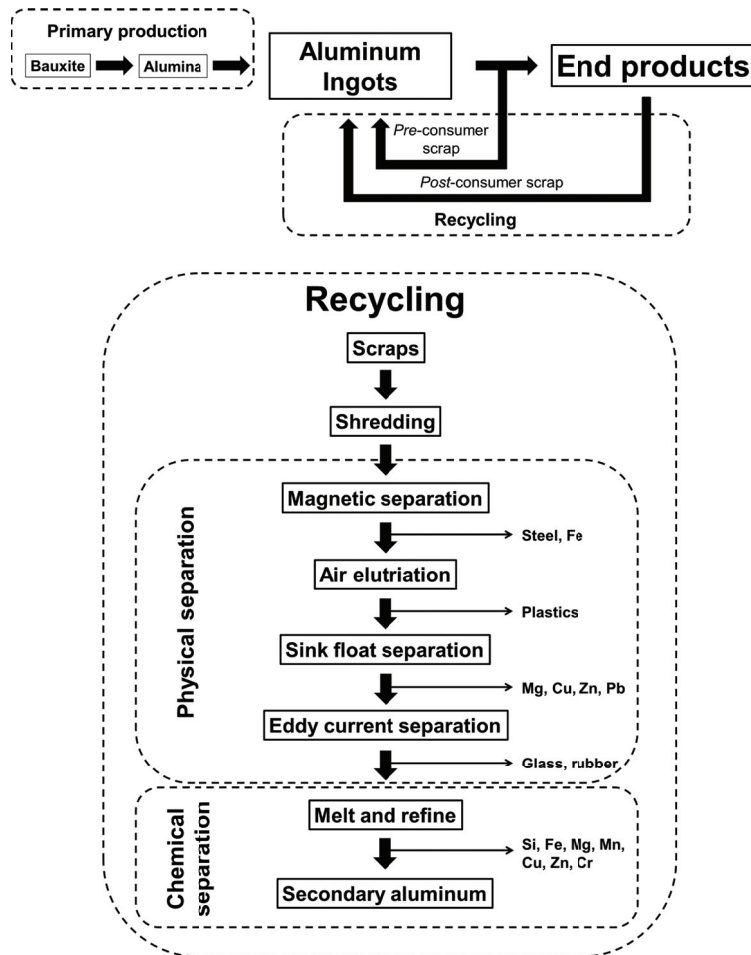
Figure 2.9: A brief description of the aluminum cycle (upper parts) and the recycling process removing elements for each process (bottom parts). This figure is partially adapted from Ref. [122].

# Chapter 3

# Transmission electron microcopy (TEM)

TEM is a very important analytical tool for *observing* microstructures and precipitate structures, using high energy electrons. The high energy electrons exhibit a *particle/wave duality* which gives the possibility to do a diversity of characterization and analysis techniques. Electrons can be observed as particles by transferring their impulse and energy and as waves by scattering and diffraction. This chapter provides the theory and principles of TEM and related techniques. The techniques are the main analytical tools in this thesis to *observe* microstructure and precipitate structure.

## 3.1 Characterization with electrons

What happens when accelerated high-energy electrons interact with a specimen? Figure 3.1 shows interactions between accelerated electrons and matter, and the following is an overview of what they are used for. As will be seen, some interactions are more suited than others to characterize and analyze the materials studied.

**Secondary & Backscattered electrons**  If the specimen is thick enough (typically more than 5 times the mean free path [127]), secondary and backscattered electrons are emitted. The emission of secondary electrons results from ejection from conduction or valence bands of atoms while backscattered electrons come from numerous elastic scattering events (interaction with the Coulomb potential) in order to return backward. They are mainly used for imaging in SEM, which creates image contrast like topological contrast for secondary electrons and atomic number contrast for backscatted electrons [127]. The backscattered electrons can
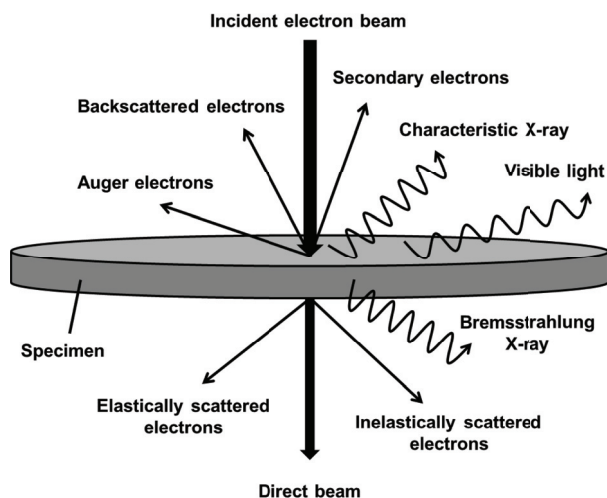
Figure 3.1: Electron-specimen interactions. The specimen is assumed to be thin. This figure is adapted from Ref [4].

also give crystallographic orientation, which is used in EBSD techniques.

**Characteristic X-ray & Auger electrons**    These are alternatives to each other, emitted by the result of the ejection of inner-shell electrons. When the inner-shell electrons are ejected by the incident electron beam, the ionized atom returns to its ground state by filling in the hole (of inner-shell) with an electron from an outer shell. The transition results in emission of either an X-ray or an Auger electron [4, 128]. This gives rise to characteristic energy (unique to the atom) as single X-ray photon (Characteristic X-ray) or one of the outer shell electrons ejected (Auger electron). Characteristic X-ray can be used for elemental analysis, e.g. EDS [4]. The Auger electrons can be used for chemical and compositional characterization of surface environments, e.g. Auger electron spectroscopy [129]. The probability of the characteristic X-ray emission against the Auger electrons is described by the *fluorescence yield* [4]. Heavy elements have higher fluorescence yield than light elements. This indicates that heavy elements tend to emit characteristic X-rays while light elements emit Auger electrons.

**Elastically scattered electrons**    The high energy incident electron beam inter-acts with either the electron cloud or the nucleus of materials, leading to elastic scattering. The elastic scattering occurs due to Coulomb forces. The interaction with the electron cloud results in small angular deviation and forward scattering,

while the interaction with nucleus is strong and backward scattering (backscattered electrons). The backward scattering is rare in TEM [4]. The elastically scattered electrons interact with the periodic potential in the materials to make interference and to form diffraction just like visible light – due to the wave nature of electrons. Here it is important to think about *coherency* of the elastically scattered electrons, i.e. phase relationship between scattered electrons: if it is *coherent* or *incoherent*. Coherent scattering can be used for high resolution TEM, which are described in section 3.3. On the other hand, incoherent scattering is known as Rutherford scattering [130], which can be used for HAADF-STEM described in section 3.6.

**Inelastically scattered electrons** Some electrons are scattered inelastically – accompanied by energy transfer. Incident electrons lose energy due to generation of X-ray and/or other electrons like Auger electrons, as mentioned. In addition to that, collective interactions with many atoms or electrons can be assumed as sources of the energy loss, e.g. plasmon excitation, specimen heating (so called beam damage). Inelastically scattered electrons can be used for EELS techniques and EFTEM imaging, which will be described in section 3.4.

## 3.2 Basic principles of TEM

The TEM instrument is a column consisting of an electron gun, electromagnetic lens systems and detectors. Figure 3.2 shows a typical TEM instrument. Electrons travel from top to bottom.

The electron "gun" is an electron source of high energy electrons. There are two types of electron sources: thermionic and field-emission filaments. A thermionic filament consists of tungsten or $LaB_6$ heated up to high temperature (~2700 K and ~1700 K, respectively [4]) to give electrons sufficient energy to leave from the surface. On the other hand, the field-emission filament is a fine needle tip made of tungsten exposed to a high electric field to extract electrons by the tunnelling effect. The field-emission filament is further divided into two types: Schottky emission and cold emission. The former makes a tungsten heated to enhance the tunnelling effect while the latter works at room temperature[1]. The resolution of a microscope is influenced by the electron gun (and accelerating voltage), depending on the energy spread in the beam, effective source size and beam coherency. For example, a cold field-emission filament has the lowest energy spread and a highly coherent beam which lead to highest resolution.

The lens system consists of electromagnetic lenses to focus the electron beam by a magnetic field adjusted by lens currents. The high energy electrons are first

---

[1]The term "cold" comes from "colder" than Schottky emission.
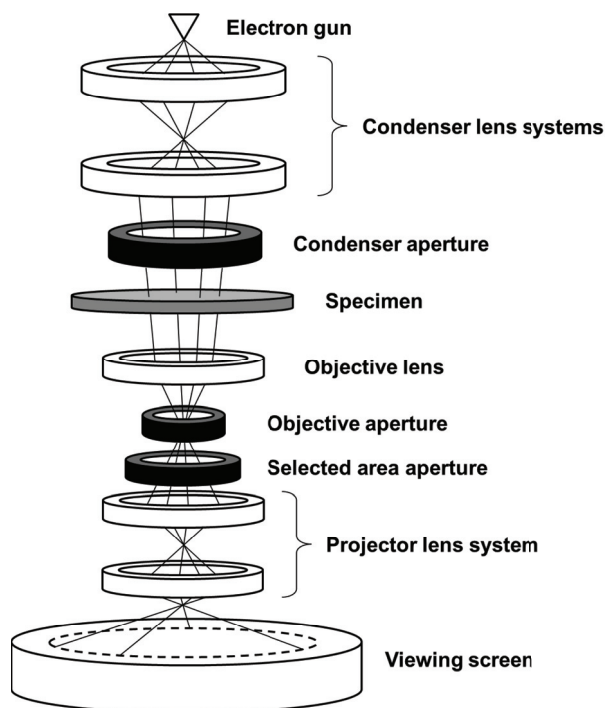
Figure 3.2: Schematic illustration of a typical TEM instrument. The electron beams come from top to bottom.

focused by the condenser lens system. Then the parallel electrons interact with the specimen. Transmitted electrons are focused by the objective lens to make an image. A diffraction pattern is made in the back focal plane of the objective lens where the objective aperture is located. Further, the projector lens system makes a projection on the viewing screen. There are two operation modes: imaging and diffraction. Both can be observed on the viewing screen by changing the lens current in the projector lens system. The selected area aperture can be inserted in the image plane to select the area for contributing to the diffraction pattern. The condenser, objective and selected area apertures can change in size and position so that needed image contrast can be achieved. The electromagnetic lenses are not perfect due to lens aberrations such as spherical aberration, chromatic aberration, coma, field astigmatism, field curvature and distortion[2]. The lens imperfections are analogue to light optics. Resolution of the microscopes is limited by aberrations.

---

[2]Spherical aberration, coma, field astigmatism, field curvature and distortion are called the *Seidel aberrations*, the same in light optics.

Recent aberration-correctors are important to improve resolution. Aberration correction will be described in section 3.8.

### 3.2.1 Image contrast

TEM image, it is important to understand image contrast – what are you observing? There are several types of image contrast: *mass-thickness*, *diffraction* and *phase contrast*. Phase contrast imaging is used for high-resolution TEM, which will be described in section 3.3. The following is an overview of mass-thickness contrast and diffraction contrast in TEM.

**Mass-thickness contrast** The mass-thickness contrast results from incoherent elastic scattering (Rutherford scattering). The Rutherford scattering cross section increases monotonically as a function of atomic number (Z). This means that high Z (high mass) atoms scatter more electrons than low Z, leading to dark for high mass region in the image. The thickness of a specimen acts in a similar manner; thicker regions scatter more electrons than thinner regions of the same average Z.

**Diffraction contrast** In crystalline specimens, the diffraction contrast comes from elastic scattering and its constructive interference along special angles (Bragg angles), i.e. Bragg's condition, also known as the Laue condition [131]. This gives characteristic diffraction patterns depending on crystal structures. There are two ways to image the diffraction contrast: *bright-field (BF)* or *dark-field (DF)*. Figure 3.3 shows a schematic illustration of a ray diagram with the BF imaging and DF imaging[3]. Only the directly transmitted beam passes through objective aperture to form the BF image while only the diffracted beam is used to form the DF image. In the BF image, the diffracted beam is blocked out so that the image is dark in the diffracted region. On the other hand, in the DF image, the diffracted beam passes through so that the image is bright in the regions which scatter to this beam. In Paper I, Paper II and Paper IV, investigations of precipitate microstructure have been performed by BF-TEM using a Philips CM30 operating at 150 kV.

## 3.3 High resolution TEM (HRTEM)

HRTEM comprises *phase contrast* imaging, one of the image contrasts mentioned in the last section. Phase contrast is an interference pattern in the image plane. The contrast is formed by the direct transmitted beam and (several) diffracted beams in

---

[3]Note that DF imaging is usually conducted by a tilted incident beam so that the objective aperture can stay on the optical axis. In Figure 3.3 (b), for easier description, the objective aperture is moved from the optical axis to pass the diffracted beam, for illustration purposes.
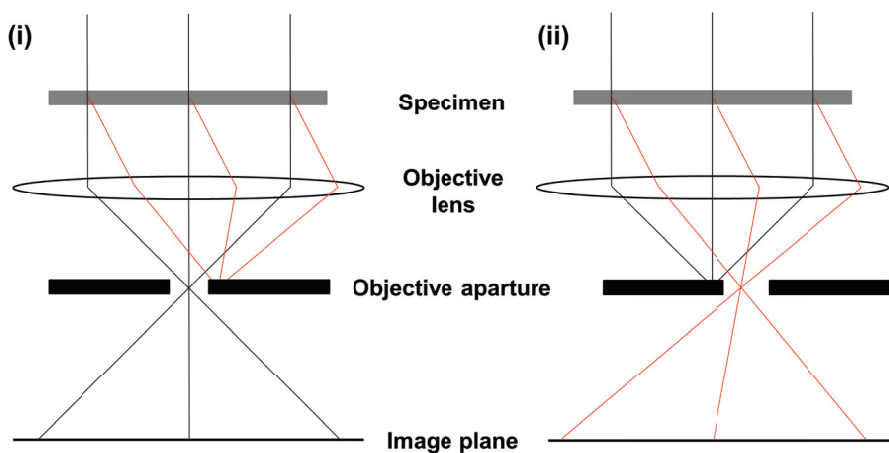
Figure 3.3: Schematic illustration of ray diagram of (a) BF imaging and (b) DF imaging. The black and red solid lines represent transmitted and scattered beams, respectively.

the image plane. Hence, the direct transmitted beam and the diffracted beams must pass through the objective aperture. Usually the objective aperture is not inserted or an aperture is inserted, which is large enough to pass both the direct beam and diffracted beams, so as to remove components of high spatial frequency. Figure 3.4 shows a schematic illustration of phase contrast image formation.

Since each diffracted beam experiences a specific phase shift (Bragg's condition), an electron wave after interaction with the specimen (called the *exit-plane wave*) contains structural information of the specimen. In general, a description of electron diffraction is complex because of the strong interaction between electrons and the specimen – dynamic diffraction should be considered, described by many Bloch waves [132]. However, if a specimen is thin, the dynamic diffraction can be ignored and the contrast mechanisms can simply be described by kinematic diffraction.

To describe the interference of beams with phase shifts by a specimen and eventually the contrast mechanism, the specimen is assumed to be an object altering the phase, but not the amplitude of the incident electron beam. In addition, the phase shift is assumed to be small. This is so called the *weak phase object approximation* [4]. Then a phase modulation of the incident electron beam can be expressed by $\exp\{-i\phi(\vec{r})\} \approx 1 - i\phi(\vec{r})$ [133] where $\phi(\vec{r})$ stands for the object (real) function reflecting the phase shift as a function of position $r$, which is associated with the projected electron potential of the specimen [4] and also called the trans-
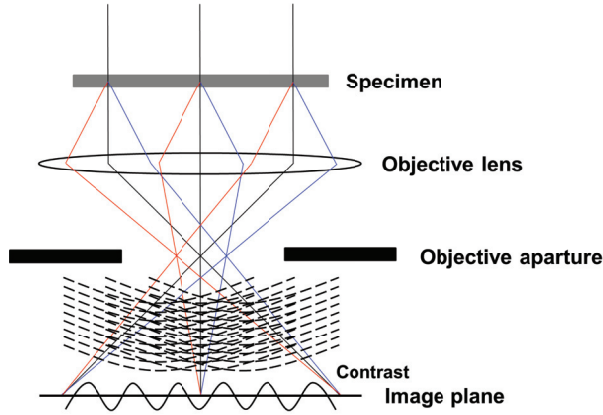
Figure 3.4: Schematic illustration of formation of phase contrast image.

mission function [134]. If a wave function of the incident electron beam is given as $\psi_{in} = 1$, the exit-plane wave function $\psi_{ep}$ can be expressed as the product of the incident electron beam and the phase shift, as follows [133]:

$$\psi_{ep}(\vec{r}) = 1 - i\phi(\vec{r}). \tag{3.1}$$

A diffraction pattern is made in the back focal plane of the objective lens (where the objective aperture is located). The electron wave function in the back focal plane $\psi_{bfp}$ can thus be written as the Fourier transform of the exit-plane wave function as follows [135]:

$$\psi_{bfp}(\vec{k}) = \mathcal{F}[\psi_{ep}(\vec{r})] = \psi_{ep}(\vec{k}) \tag{3.2}$$

$\mathcal{F}$ stands for the Fourier transform and $k$ for the reciprocal space vector, which is unique to the crystal lattice – *diffraction patterns*. Here it is easy to imagine that the wave function of the image plane is the inverse Fourier transform of the back focal plane wave function. *However*, in this process, transfer characteristic of the lens system for the imaging must be considered because of lens aberrations. Hence, the wave function in the image plane, $\psi_{ip}(\vec{r})$ can be expressed with so called the *contrast transfer function (CTF)* $f_{(CTF)}(\vec{k})$ as follows [131]:

$$\psi_{ip}(\vec{r}) = \mathcal{F}^{-1}[\psi_{ep}(\vec{k})f_{(CTF)}(\vec{k})] \tag{3.3}$$

where $\mathcal{F}^{-1}$ stands for inverse Fourier transform.

### 3.3.1 The contrast transfer function (CTF) $f_{(CTF)}(\vec{k})$

Since the spatial frequencies of the phase in the individual exit-plane wave $\psi_{ep}(\vec{r})$ are unequally transferred to the image plane, the CTF $f_{(CTF)}(\vec{k})$ is not constant [136, 137], but contains contributions determining the characteristics of the phase contrast images in HRTEM. The contributions contain diffraction from the objective aperture, $H(\vec{k})$, degrees of coherence (partial spatial and partial temporal coherence), $E(\vec{k})$ and aberrations of the lens system, $B(\vec{k})$. Considering the effects of these contributions, the CTF $f_{(CTF)}(\vec{k})$ can be written as a product of the individual terms as follows:

$$f_{(CTF)}(\vec{k}) = H(\vec{k})E(\vec{k})B(\vec{k}). \tag{3.4}$$

The following gives a description of each contribution of the CTF:

**Diffraction from the objective aperture:** $H(\vec{k})$   As mentioned, the objective aperture is located in the back focal plane of the objective lens. This gives a diffraction pattern. The effect of the objective aperture on the exit-plane wave function can be described by a *top-hat function*: one inside the objective aperture and zero outside.

   Alternatively, the objective aperture function can approximately be described by the *Fermi function*. In this way, a discontinuous edge can be avoided e.g. in numerical computation [134].

**Degree of coherence:** $E(\vec{k})$   The degree of coherence is important to have the interference because of its phase relation between individual waves. Ideally, an electron source produces a fully coherent incident electron beam. However, a *real* electron source has a finite size and produces electrons with slightly varying energies. This leads to partial spatial coherence and partial temporal coherence, giving damping envelope functions in the CTF, which reduce the information transfer at high spatial frequencies [138].

**Aberrations of lens system:** $B(\vec{k})$   The electromagnetic lenses are not perfect due to lens aberrations and the resolution of the microscope is limited by the aberrations. In fact, aberrations are essential for phase contrast imaging. The lens aberration gives a phase shift.

   The effect of aberrations on the CTF can be expressed as follows:

$$B(\vec{k}) = exp\{-i\chi(\vec{k})\} = \cos\{\chi(\vec{k})\} - i\sin\{\chi(\vec{k})\} \tag{3.5}$$

where $\lambda$ stands for wave length and $\chi(\vec{k})$ for the *aberration function* describing the phase shift induced by the objective lens. For aberration uncorrected TEM, spherical aberration, $C_s$, and defocus, $\Delta f$ of the objective lens dominate and determine the aberration function as follows:

$$\chi(\vec{k}) = \chi(k) = \frac{1}{2}k^2\lambda^2\Delta f^2 + \frac{1}{4}k^4\lambda^4 C_s^4 \tag{3.6}$$

Here, $C_s$ and $\Delta f$ are isotropic aberrations. Hence, $\chi$ is isotropic being able to substitute $\vec{k}$ with $k =| \vec{k} |$. Interestingly, if there are no aberrations, the aberration function is equal to zero and the contribution $B(\vec{k})$ to the CTF becomes zero. This means that aberration of the lens system is essential to the phase contrast imaging.

## 3.3.2 Image intensity

Now we can come back to the wave function in the image plane (eq. (3.3)) to describe image intensity. Considering the above mentioned CTF, the wave function in the image plane can be expressed as follows:

$$\psi_{ip}(\vec{r}) = \mathcal{F}^{-1}[\psi_{ep}(\vec{k})f_{(CTF)}(\vec{k})] = \psi_{ep}(\vec{r}) \otimes f_{(CTF)}(\vec{r}) \tag{3.7}$$

where $\otimes$ stands for the convolution. Since the exit plane wave is a complex wave function of a weak phase object, as mentioned, $1 -i\phi(\vec{r})$, the wave function in the image plane can be further deduced as follows [133]:

$$\psi_{ip}(\vec{r}) = 1 + \phi(\vec{r}) \otimes \mathfrak{I}\{f_{(CTF)}(\vec{r})\} - i\phi(\vec{r}) \otimes \mathfrak{R}\{f_{(CTF)}(\vec{r})\} \tag{3.8}$$

where $\mathfrak{R}$ and $\mathfrak{I}$ stand for real and imaginary parts, receptively. If quadratic term in $\phi(\vec{r})$ is neglected, the image intensity in the image plane, $I_{\text{ip}}$, is then expressed as follows [133]:

$$I_{ip}(\vec{r}) =| \psi_{ip}(\vec{r}) |^2= 1 + 2\{\phi(\vec{r}) \otimes \mathfrak{I}\{f_{(CTF)}(\vec{r})\}\}. \tag{3.9}$$

Hence, the spatial frequency of the image intensity in the image plane can be expressed as follows:

$$I_{ip}(\vec{k}) = \mathcal{F}[I_{ip}(\vec{r})] = \delta(\vec{k}) + 2\phi(\vec{k})\mathfrak{I}\{f_{(CTF)}(\vec{k})\}. \tag{3.10}$$

The important thing here is that the imaginary part of CTF contributes to phase contrast imaging in HRTEM. Considering the CTF (eq. (3.4)), the image intensity can finally be deduced as follows:

$$I_{ip}(\vec{k}) = \delta(\vec{k}) + 2\phi(\vec{k})H(\vec{k})E(\vec{k}) \sin\{\chi(\vec{k})\}. \tag{3.11}$$

This shows that the image intensity is oscillating as a function of spatial frequency due to a sine function which is affected by spherical aberration, $C_s$, and defocus, $\Delta f$. In addition, the degree of coherence, $E(\vec{k})$, gives a damping envelope function. Only the term, $E(\vec{k})\sin\{\chi(\vec{k})\}$, is commonly called the phase CTF[4]. Figure 3.5 shows the phase CTF.
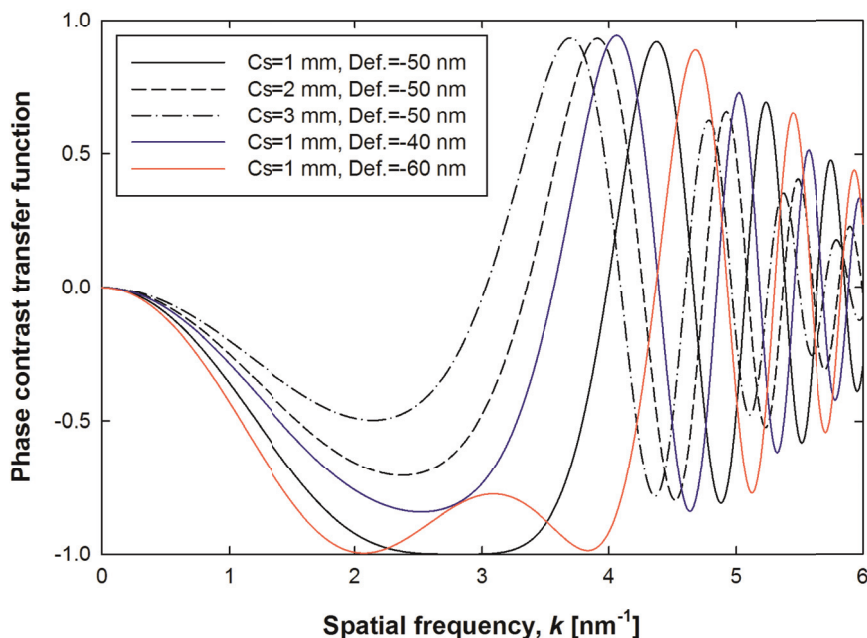


Figure 3.5: The phase CTF for 200 kV for different values of spherical aberration, $C_s$, and defocus, $\Delta f$. For an electromagnetic lens, the $C_s$ is always positive [139]. This figure is plotted with the code provided in Ref. [134].

As seen from Figure 3.5, the phase CTF becomes either positive or negative, depending on spatial frequency. This gives contrast reversal: atoms are bright on a dark background if it is positive, and *vice versa* if it is negative. In addition, it is sensitive to spherical aberration and defocus. In practice, since spherical aberration is fixed depending on the TEM instrument, defocus is adjusted to get directly interpretable images so that the CTF is "flat" – information can be transferred without any contrast reversal. There is so called the Scherzer defocus [139] which is an ideal defocus to compensate the effect of spherical aberration.

---

[4]Only the sine term is often called the *coherent* phase CTF.

Above described the contrast mechanism is for aberration *uncorrected* TEM. If the spherical aberration is corrected, the aberration function $\chi(\vec{k})$ must be considered with additional aberrations. This will be explained later in section 3.8.

In Paper II, investigations of precipitate atomic structure are performed by a JEOL 2010F operating at 200 kV and having 0.2 nm point resolution.

## 3.4 Electron energy loss spectroscopy (EELS)

EELS measures energy loss of inelastically scattered electrons after interaction with the specimen. Analysis of the energy loss spectrum is highly useful to understand how the incident electrons lose their energy. Energy loss electrons are detected by magnetic prism spectroscopy in which a uniform magnetic field is generated [140]. Figure 3.6 shows a schematic illustration of the magnetic prism spectrometer used for EELS. Electrons having different energies (due to the energy loss) are dispersed in magnetic prism in different deflection angle due to the Lorentz force. Hence, a spectrum comes depending on the electron energy loss after interaction with a specimen. The energy loss spectrum contains several intensity changes, depending on interactions. There are mainly three parts as follows.

**Zero loss peak**  The zero-loss peak comes from electrons which have lost zero energy, giving a sharp peak in the spectrum. The peak stands at 0 eV, including the incident direct beam electrons and elastically scattered electrons. The width of the zero loss peak contains information of the energy distribution of the electron source, e.g. 1-2 eV for $LaB_6$, 0.8 eV for Shottkey and 0.3 eV for cold field-emission filaments [140]. The zero loss peak also contains electrons which have lost energy to phonon excitations – atomic vibrations – giving small energy losses. This is usually smaller than the energy distribution of the electron source, which is hence not resolvable [4].

**Plasmon peak(s)**  The plasmon peak(s) result from inelastic scattering of weakly bound outer-shell electrons, conduction and valence electrons, known as quantized oscillations – *plasmon*. The peak(s) arise broadly in a second most dominant peak after the zero-loss peak, which is useful to measure thickness of the specimen.

**Core-loss peak**  The core-loss peak(s) result from inelastic scattering from inner-shell electrons. The peak(s) appear at so called the *ionization edges* at certain energy losses depending on elements. Hence, it can be useful to analyse e.g. elemental analysis [140]. The fine structure of the edges can be analysed, called energy-loss near-age structures (ELNES) which is analogous to X-ray absorption

fine structure (XAFS) in X-ray absorption spectroscopy.

**(i)**                              **(ii)**
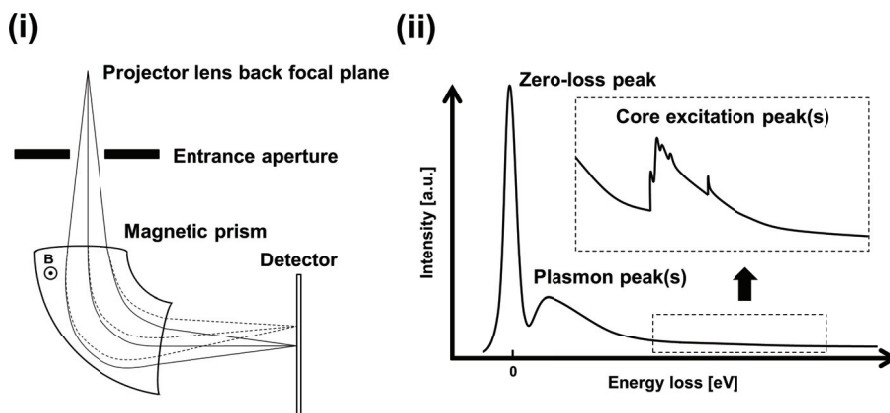
Figure 3.6: (i) Schematic illustration of the magnetic prism spectrometer of EELS and (ii) a typical energy loss spectrum. The dashed lines in (i) represent energy loss electrons while the solid lines are no loss electrons. The dashed rectangle shows a magnified region of core excitation peaks which are much lower than the zero-loss and plasmon peaks. This figure is partially adapted from Ref. [140].

If an additional lens system is installed after the magnetic prism, it is possible to form an image. In addition, a slit can be inserted so that a certain energy loss range is selected to form an image. This is so called energy-filtered TEM (EFTEM), which contains contrast associated with selected characteristic energy loss.

A reason for using the EELS technique in this thesis is to measure thickness of the specimen. The thickness is used for quantification of precipitate microstructure, which will be described in next subsection. The thickness can be measured by considering the probability of inelastic plasmon scattering (which can follow Poison statistics [140] – how many times the electrons are scattered). The measurement of the integrated intensities of the zero loss peak ($I_0$) and the whole spectrum ($I_t$) can deduce the thickness ($t$) as follows:

$$t = \lambda ln\left(\frac{I_t}{I_0}\right) \tag{3.12}$$

where $\lambda$ stands for the inelastic mean free path for plasmon scattering.

In Paper I, Paper II and Paper IV, thickness measurements for quantification of the microstructure are performed by a Gatan parallel electron energy loss spectrometer.

### 3.4.1 Quantification of microstructure from a combined TEM and EELS

Quantification of microstructure are conducted in this thesis described in Paper I, Paper II and Paper IV. Precipitate needle lengths, cross sections, number densities and volume fractions are calculated by a combination of BF-TEM images and thickness measured by EELS. The measurement is not straight-forward, since thickness of the specimen is usually 50-110 nm in which precipitate needles can be "cut" during sample preparation. Figure 3.7 shows a schematic illustration of the geometry of a TEM specimen, precipitates and the incident electron beam, and an example of a BF-TEM image. Some precipitates are seen as "cut" on the edge of specimen. This factor gives errors of the quantification. Hence, the quantification of the precipitate needle lengths and number densities must be conducted with corrections to estimate the actual values.

The precipitate number densities ($\rho$) are defined as the total number of precipitates over the volume in the TEM images as follows:

$$\rho = \frac{3N}{At} \tag{3.13}$$

where $N$ stands for the number of precipitates counted, $A$ for the corresponding area on the BF-TEM image, and $t$ for the thickness of corresponding area measured by EELS. The factor 3 arises because only needles viewed along one of the <001>Al are counted. Considering the correction of the errors, the calculation use the "effective thickness" ($t + \lambda$) showing the sum of the thickness and the average needle lengths $\lambda$, as follows:

$$\rho = \frac{3N}{A(t + \lambda)}. \tag{3.14}$$

The needle lengths measured on the BF TEM images should also be corrected because of the error. Hence, the average needle lengths $\lambda$ are calculated using a formula with the correction as follows:

$$\lambda = \frac{l_m}{1 - (l_m/t)\cos\theta\tan\phi} \tag{3.15}$$

where $l_m$ stands for the measured needle length, $\theta$ for the angle between the precipitate needles perpendicular to the incident electron beam and the specimen surface, and $\phi$ for specimen tilt angle in the microscope. $\theta$ can usually not be measured, but $\theta = 45°$ is used since this angle is reasonably accurate [141].

The methodology has been established and summarized elsewhere [55, 141].
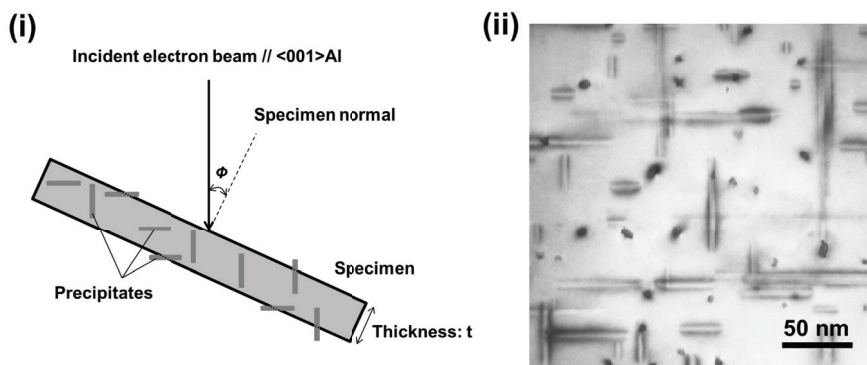
Figure 3.7: (i) Schematic illustration of geometry of specimen, precipitates and incident electron beam, and (ii) an example of a BF TEM image of precipitate microstructure in Al-Mg-Si alloys taken along <001>Al. The thickness is ~50 nm. The image is taken by the author.

## 3.5   Energy dispersive X-ray spectroscopy (EDS)

EDS is a technique for elemental analysis using characteristic X-rays. The technique enables chemical composition of the specimen to be determined qualitatively and quantitatively. Since the characteristic X-ray has an energy unique to an element, as mentioned, detection of the energy can answer which elements the X-ray originates from. The detector is made by a Si semiconductor detecting a single X-ray photon to generate electric charge. This is proportional to the energy of the photon [4]. However, quantitative analysis of precipitates by EDS is relatively problematic – accurate analysis is not straight-forward because of several error sources. For example, for precipitates in Al-Mg-Si alloys, the specimens have thickness giving overlapped areas of phases and Al matrix, which gives errors. Emission of the characteristic X-ray is limited to light elements because of fluorescence yield as mentioned. Hence, the EDS technique is good at analysis of heavier elements.

A combination of EDS and scanning TEM (which will be described in next section) can produce so called *elemental map* – which elements are there in corresponding images. The combination is used in Paper IV for qualitative elemental map by a JEOL 2010F operated at 200 kV and equipped with an EDS from Oxford Instruments (with INCA software).

## 3.6    Scanning transmission electron microscopy (STEM)

The STEM technique is described by a convergent electron beam forming a focused electron probe which scans on the specimen, and the transmitted electrons after the interaction with the specimen are detected. The electron probe is scanned in a rectangular area and *each scan position* gives results of the interaction in detector plane where the diffraction pattern forms. Compared to TEM, STEM uses a convergent electron beam instead of a parallel one. If you look carefully, the electron optics of STEM is interestingly identical to the TEM, just up side down – the convergent lens and the illumination aperture are analogues to the objective lens and the objective aperture, respectively. Figure 3.8 shows a schematic illustration of the STEM optics. There are mainly two types of detectors: BF[5] and high angle annular dark-field (HAADF)[6] detectors. The electron probe is focussed on the specimen, and forms a convergent-electron beam diffraction pattern in the detector plane. This gives diffraction discs for each diffracted beam, which overlap and interfere to form the STEM signal. The signal on the BF detector corresponds to the central disc and the overlapping first-order diffraction discs [4]. On the other hand, the HAADF detector picks up close to elastically scattered electrons which result from high angle incoherent scattering. This will be described in the next subsection.

In STEM, the size of the electron probe is important, as it determines resolution. If the probe size is smaller than the inter atomic spacing, the STEM image will directly correspond to the atomic structure – the smaller electron probe size, the better resolution. The electron probe size depends on the illumination aperture, the spherical aberration of the lens system and the coherence of electron source, which are briefly described in section 3.8.

### 3.6.1    High angle annular dark-field (HAADF)-STEM

A HAADF detector picks up the signal of elastically scattered electrons which results from high angle incoherent scattering. This means the Rutherford scattering from each atom contributes to the HAADF image – the image intensity is proportional to the atomic number (Z). Hence, the HAADF-STEM technique is often called "Z-contrast" imaging. The HAADF-STEM technique has advantages to more directly interpret atomic structure, compared to HRTEM, for further modelling. This greatly contributes the investigation of atomic structure of Al-Mg-Si alloys, as described in Paper II, Paper III, Paper IV and Paper V.

---

[5]Recent development also includes an annular bright-field (ABF) detector which has advantages to observe light elements [142, 143].

[6]The terminology sometimes varies depending on scattering angle; annular dark-field (ADF), low angle annular dark-field (LAADF) or middle angle annular dark-field (MAADF).
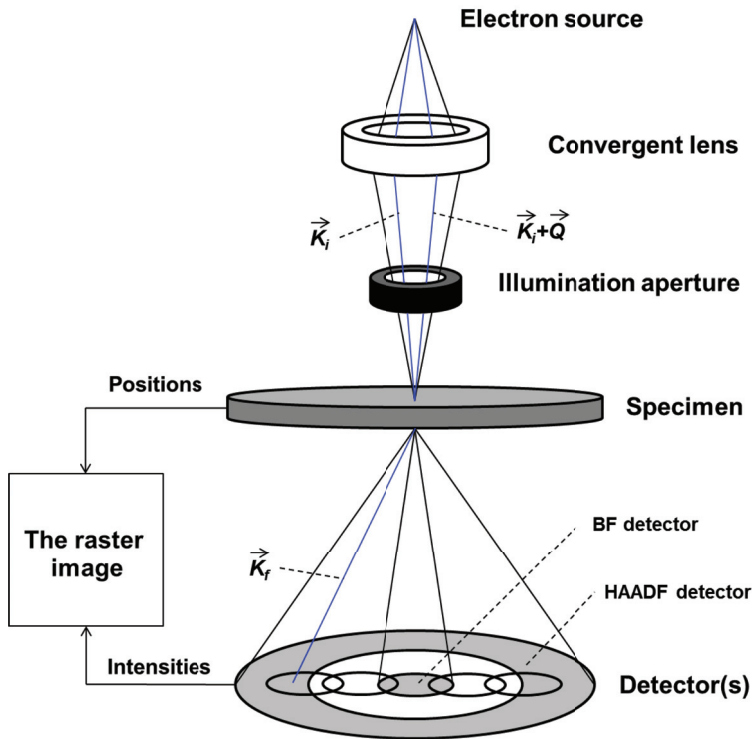
Figure 3.8: Schematic illustration of STEM. $\vec{K}_i$ is the perpendicular component of the reciprocal space vector and the final wave $\vec{K}_f$ is detected on the HAADF detector, resulting from the interference between the initial partial waves separated by $\vec{Q}$. See subsection 3.6.1. The electron probe is scanned in a rectangular area in a raster over the specimen to collect intensities at each probe position.

**The intensity of HAADF-STEM images**   As mentioned, HAADF-STEM images result from high-angle incoherent scattering. A mathematical description of the intensity of incoherent scattering can be written by convolution of probe function, $P(\vec{r})$ and object wave function, $\psi(\vec{r})$ as follows [5]:

$$I_{HAADF} =\mid P(\vec{r}) \mid^2 \otimes \mid \psi(\vec{r}) \mid^2 \qquad (3.16)$$

The probe function can be written as so called the aperture function [5]: $A(\vec{k}) = H(\vec{k})sin\{\chi(\vec{k})\}$ where $H(\vec{k})$ and $\chi(\vec{k})$ are a function affected by the aperture and the aberration function, respectively, as described in section 3.3. Note that a coherent electron source is assumed here for simplicity– no consideration of partial incoherence due to electron source is included. The probe function in the specimen

plane can be expressed as the inverse Fourier transform as follows:

$$P(\vec{r}) = \int A(\vec{k})exp\{2\pi i(\vec{k} \cdot \vec{r})\}d\vec{k} \qquad (3.17)$$

Since the electron probe is scanned across the specimen, the shift of the probe position $\vec{r}_0$ is employed as follows[5]:

$$P(\vec{r} - \vec{r}_0) = \int A(\vec{k})exp[2\pi i\{\vec{k} \cdot (\vec{r} - \vec{r}_0)\}]d\vec{k}. \qquad (3.18)$$

To describe the intensity of the HAADF-STEM image, electron scattering from a crystal must be considered. The electron scattering from a crystal can be expressed by so called the *Bloch wave* approach for dynamic electron diffraction [132]. Considering a crystal with a periodic potential, a solution of the Schrödinger equation gives the Bloch waves which reflect lattice periodicity as follows:

$$b^{(j)}(\vec{k}, \vec{r}) = \sum_g \Phi_g^{(j)} exp[2\pi i(\vec{k}_0^{(j)} + \vec{g}) \cdot \vec{r}] \qquad (3.19)$$

where $j$ =1, 2 .. n, represents different Bloch waves reflecting propagation of electron waves in a crystal, g stands for lattice points in reciprocal space, $k_0$ for wave vector in lattice points 0 in the reciprocal space and $\Phi_g^{(j)}$ is the amplitude factor.

From now on, the real and reciprocal space vectors can be further written in their components perpendicular and parallel to the optic axis: $\vec{r} = (\vec{R}, z)$ and $\vec{k} = (\vec{K}, k_z)$, and it is assumed that the components of the Bloch waves have no interaction with the crystal periodicity along the beam direction [5]. The total wave function within the crystal is a linear combination of the Bloch waves [132], describing the sum of many Bloch states propagating through the crystal and interfering with one another depending on the depth [144] as follows:

$$\psi(\vec{R}, z, \vec{K}_i) = \sum_j \sum_g \Phi_0^{(j)*}(\vec{K}_i)\Phi_g^{(j)}(\vec{K}_i)exp\{-2\pi i[(\vec{K}_i + \vec{g}) \cdot \vec{R} + k_z^{(j)}(\vec{K}_i)z]\} \quad (3.20)$$

where $\Phi_0^{(j)*}(\vec{K}_i)$ is the amplitude of excitation of the $j$ th Bloch state for plane-wave illumination. The total intensity of the incoherent scattering on the HAADF detector can be described with integrating over detector function in reciprocal space, combined with the probe function and the total wave function within the crystal as follows [5]:

$$I(\vec{Q}, z) = \sum_g D_g \int A(\vec{K}_i)A(\vec{K}_i + \vec{Q}) \sum_{j,k} \Phi_0^{(j)*}(\vec{K}_i)\Phi_Q^{(k)}(\vec{K}_i)\Phi_g^{(j)}(\vec{K}_i)\Phi_g^{(k)*}(\vec{K}_i)$$

$$\cdot exp\{-2\pi i[k_z^{(j)}(\vec{K}_i) - k_z^{(k)}(\vec{K}_i)]\}d\vec{K}_i \tag{3.21}$$

The $g$ summation represents Bragg beams on the HAADF detector, and it acts only on a product pair of the Bloch wave amplitude factor [5]:

$$C_{jk}(\vec{K}_i) = \sum_g D_g \Phi_g^{(j)}(\vec{K}_i) \Phi_g^{(k)*}(\vec{K}_i) \tag{3.22}$$

Here, contributions to the intensity on the HAADF detector only come from Bloch states that have frequency components of lattice points [5]. This shows hence, in thicker specimen (where dynamic diffraction must be considered), that *broader* Bloch states in reciprocal space – and therefore *sharper* states in real space – contributes to the intensity [5] on the HAADF detector. Because the tightly bound 1s states of electrons are highly localized in the crystal, the image intensity is dominated by scattering from the 1s states [144]. Because the 1s states do not overlap at a typical crystal spacing, the scattering is independent of the wave vector $\vec{K}_i$. Hence, the factor $C_{jk}(\vec{K}_i)$ can be removed from the integral over $\vec{K}_i$ and be approximated by the square of the atomic number, $Z^2$ value for Rutherford scattering [145] as follows:

$$I(\vec{Q}, z) \propto Z^2 \int A(\vec{K}_i)A(\vec{K}_i + \vec{Q}) \sum_{j,k} \Phi_0^{(1s)*}(\vec{K}_i)\Phi_Q^{(1s)}(\vec{K}_i)$$

$$\cdot exp\{-2\pi i[k_z^{(1s)}(\vec{K}_i) - k_z^{(1s)}(\vec{K}_i)]\}d\vec{K}_i \tag{3.23}$$

The above description assumes that the components of the Bloch wave have no interaction with the crystal periodicity along the beam direction. This does not give *longitudinal incoherence* to the HAADF intensity, but *transverse incoherence*. The longitudinal incoherence is provided by atomic vibrations. Thermal vibrations of atoms, known as phonons, lead to diffuse background intensity. This is called thermal diffuse scattering (TDS), which builds up longitudinal incoherence [5].

In Paper III, Paper IV and Paper V, investigations of precipitate atomic structure are performed by a spherical aberration probe corrected JEOL ARM 200F operated at 200 kV. The inner and outer collection angles of the HAADF detectorsare in the range of 45 and 150 mrad, respectively.

## 3.7    STEM image simulations

STEM image simulations can be done by numerical calculations. Simulation is a beneficial tool to comprehend the intensity in HAADF-STEM images. This is because the intensity of HAADF-STEM is dependent on several factors, which can easily be varied. For the numerical calculation, there are two methods [134]:

the *Bloch wave* method and the *multislice* method. The Bloch wave method is basically the description shown in section 3.6.1. The multislice method can be described with thin two-dimensional slices dividing a specimen along the electron beam direction, where the electron beam is transmitted through a slice and propagates to the next slice [134]. Since the slice is thin enough, the propagation can be assumed within a simple phase object.

There are two approximations used to treat TDS: *absorptive potential* [146] and *frozen phonon* approximations [147]. In the absorptive potential approximation, an integrated intensity falling on the HAADF detector is given by a sum of the probe intensity at each atomic column weighted by the corresponding TDS cross section [146]. The frozen phonon approximation assumes a random offset of the position of each atom due to the thermal vibration for each slice[7]. The final image intensity is averaged over several different configurations. The amplitude of the offset position is related to the Debye-Waller factor, based on an Einstein model of the density states for phonons [131]. In Paper V, the multislice method with the frozen phonon approximation is used for the STEM image simulations, using the QSTEM software package [148]. The following is a description of the musltislice frozen phonon simulation.

**Multislice frozen phonon simulation**    The electron beam is transmitted through a slice and propagated to the next slice. Figure 3.9 shows a schematic illustration of each slice. The mathematical expression is as follows [134]:

$$\psi_{n+1}(x, y) = p_n(x, y, \Delta z_n) \otimes [t_n(x, y)\psi_n(x, y)] \tag{3.24}$$

where $\psi_n(x, y)$ is the wave function before slice $n$, and $p_n(x, y, \Delta z_n)$ and $t_n(x, y)$ stand for propagator and transmission functions. Since each slice is thin, the propagator function is associated with the Fresnel diffraction[8] over the thickness of the slice, $\Delta z_n$ [134]. The transmission function is associated with the projected electron potential as mentioned in section 3.3. The propagator function can easily be expressed in the reciprocal space. In order to minimize computational time, the fast Fourier transform (FFT) algorithm is used. Using the convolution theorem, the formula can be expressed as follows:

$$\psi_{n+1}(x, y) = \mathcal{F}^{-1}\{p_n(k_x, k_y, \Delta z_n)\mathcal{F}[t_n(x, y)\psi_n(x, y)]\} \tag{3.25}$$

In the end of the slice, the final wave function is integrated over the HAADF-STEM detector to get the intensity.

---

[7]It is difficult to determine the exact phonon dispersion. Hence, the random offset is assumed here. This is actually called *frozen lattice approximation*.

[8]Near-field diffraction.
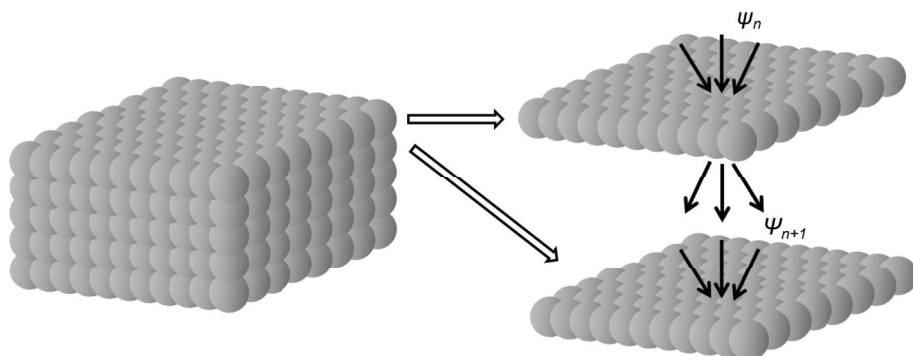
Figure 3.9: Schematic illustration of each slice of a multislice simulation. A slice is drawn as one layer of atoms. However, a slice is not necessarily one layer in the multislice simulation, but it should be as thin as being able to assume a simple phase object.

## 3.8 Aberrations of an electromagnetic lens and the correction

The resolution of TEM and STEM images is greatly influenced by aberrations of the electromagnetic lens system. The limitation and aberrations are analogue to light optics. In Paper III, Paper IV and Paper V, aberration-corrected HAADF-STEM is used to investigate precipitate structures. In this section, firstly the resolution limit due to diffraction is described. The wave nature of the electron gives the limitation of resolution. Secondly, spherical aberrations and chromatic aberrations are described, which are the main aberrations in aberration "uncorrected" microscopes. If these aberrations are corrected, different aberrations become important. Aberration correctors and higher-order aberrations are further described.

### 3.8.1 Diffraction limit

The resolution of STEM images is limited by the effect of diffraction. A circular illumination aperture, which decides the convergence semi-angle for an electron probe, gives the diffraction pattern. The electron probe is so called the *Airy pattern*[9] [149]. The probe size is decided by the first zero of the Airy pattern, and the radius $\delta_D$ can be written as follows [133]:

---

[9]It is also called as the *Airy disk*.

$$\delta_D = 0.61\frac{\lambda}{\alpha} \tag{3.26}$$

where $\lambda$ stands for the wave length of the electron and $\alpha$ for the convergence semi-angle. This is so called the *diffraction limit* by presence of an aperture, affecting the probe size of STEM and consequently the resolution of HAADF-STEM images. For TEM, the resolution is also limited by the Airy pattern, called the Rayleigh's criterion – defined by where distance between the center of an Airy pattern is at the minimum of another Airy pattern.

### 3.8.2 Spherical and chromatic aberrations

Spherical and chromatic aberrations are the main aberrations in an aberration "uncorrected" electron microscope. Figure 3.10 shows a schematic illustration of spherical and chromatic aberrations. These lens effects are the same for both TEM and STEM. The convergent lens is the one described for STEM, which is analogous to the objective lens for TEM. Spherical aberration is essential to form a phase contrast image for HRTEM, as mentioned in section 3.3. Considering the fact that an electromagnetic lens has a positive spherical aberration [139], the focal distance of the lens decreases with increasing off-axial distance of the electrons, see Figure 3.10 (i). This results in a small disk, so called the *disk of least confusion*. This gives presence of aberration in the Gaussian focal plane. The disk of least confusion $\delta_s$ can be expressed as follows [133]:

$$\delta_s = \frac{1}{4}C_s\alpha^3 \tag{3.27}$$

Chromatic aberration arises from the fact that the refraction index depends on the wavelength. As mentioned in section 3.2, the electron source has an energy spread – deviation of the wavelength. This deviation leads to a spread in the focus length, called the chromatic aberration, see Figure 3.10 (ii). The disk of least confusion due to the chromatic aberration $\delta_c$ can be expressed as follows [133]:

$$\delta_c = C_c\alpha\frac{\Delta E}{E_0} \tag{3.28}$$

where $C_c$ stands for the chromatic aberration coefficient, $\Delta E$ for the energy spread and $E_0$ for the nominal electron energy.

Here, we can understand that the disk of least confusion for the spherical and chromatic aberrations has relations with the convergence semi-angle: $\delta_s \propto \alpha^3$ and $\delta_c \propto \alpha$. Considering the effect of the Airy pattern mentioned in subsection 3.8.1 ($\delta_D \propto \alpha^{-1}$), the optimal electron probe size for STEM can be found by adjusting the convergence semi-angle.
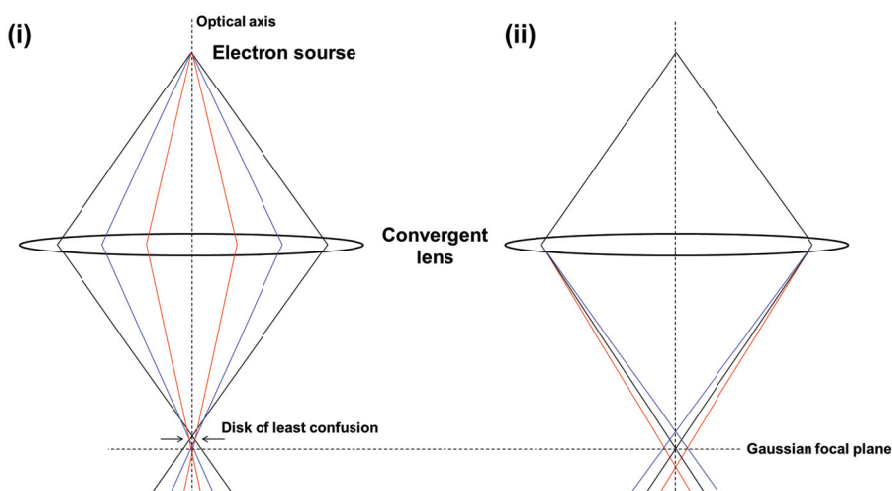
Figure 3.10: Schematic illustration of (i) spherical and (ii) chromatic aberrations. Vertical and horizontal dashed lines represent optical axis and the Gaussian focal plane, respectively. The convergent lens is a description for STEM, which is analogue to the objective lens for TEM. Hence the aberrations are the same for both TEM and STEM.

### 3.8.3   Higher-order aberrations and aberration correctors

In the previous subsection, the main aberrations – spherical and chromatic aberrations – are described. They always exist because some electrons pass through a lens far from the optical axis. So far, we have assumed that the lens effects on resolution are "homogeneous" within a lens. All electrons going through the lens are affected in the same lens. This assumption is called the *isoplanatic approximation*. However, it is not valid in reality because of the presence of off-axial aberrations. If the spherical aberration is corrected, impact of the off-axial aberrations become important. The off-axial aberrations include coma, field astigmatism, field curvature and image distortion[10]. When the off-axial aberrations are considered, the aberration function can be further expressed including them. If we introduce a geometrical parameter $\omega$ in the lens plane, which is a complex notation: $\omega = \theta_x + i\theta_y$ and $\bar{\omega} = \theta_x - i\theta_y$ where $\theta$ is the scattering angle $\approx \lambda\vec{k}$, the aberration function can be expressed as follows [133]:

$$\chi(\omega) = \Re\left\{ A_0\bar{\omega} + \frac{1}{2}C_1\omega\bar{\omega} + \frac{1}{2}A_1\bar{\omega}^2 + B_2\omega^2\bar{\omega} + \frac{1}{3}A_2\bar{\omega}^3 \right.$$

---

[10]These off-axial aberrations and the spherical aberration are called the *Seidel aberrations*, the same in light optics.

$$+\frac{1}{4}C_3(\omega\bar{\omega})^2 + S_3\omega^3\bar{\omega} + \frac{1}{4}A_3\bar{\omega}^4$$

$$+B_4\omega^3\bar{\omega}^2 + D_4\omega^4\bar{\omega} + \frac{1}{5}A_4\bar{\omega}^5$$

$$+\frac{1}{6}C_5(\omega\bar{\omega})^3 + S_5\omega^4\bar{\omega}^2 + R_5\omega^5\bar{\omega} + \frac{1}{6}A_5\bar{\omega}^6 + ...\Big\}$$  (3.29)

where $A_n$ is the n-th order astigmatism which has an (n+1)-fold symmetry, $C_n$ is the spherical aberration, $B_n$ is the axial coma, $S_n$ is the star aberration[11], $D_n$ is the three-lobe astigmatism[12], $R_n$ is the rosette aberration[13]. Here, the aberration notation is taken from [150]. $C_1$ and $C_3$ are the same as the defocus $\Delta f$ and the spherical aberration $C_s$ described in section 3.3. Different notations can also be found in [151]. This shows higher order aberration has to be considered when the spherical aberration is corrected.
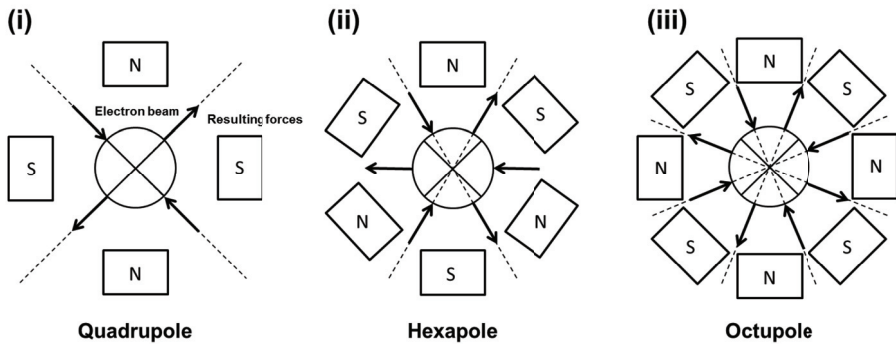


Figure 3.11: Schematic illustration of multipole lenses: (i) Quadrupole, (ii) hexapole and (iii) octupole lenses. Each center of the image represent the electron beam along the viewing direction. "N" and "S" represent magnetic poles of the electromagnetic lens. Solid arrows show the direction of the force acting on the electron beam.

The term, "aberration-corrected" is in general used for spherical aberration correction. For improving the energy resolution, monochromators are generally used such as Wien filter or Omega filter [4]. To correct spherical aberration, a general idea is to install a diverging lens to compensate for the effect of a converging lens. This can be achieved by multipole correctors. Figure 3.11 shows a schematic illustration of several multipole lenses. Resulting forces depend on

---

[11]Astigmatism of $C_n$.
[12]3-fold astigmatism.
[13]4-fold astigmatism of $C_n$.

the number of magnetic "poles" due to their rotational symmetry. A combination of these multipole lenses enables the spherical aberration to be corrected. Recent development of the spherical aberration corrector includes a double-hexapole system [152, 153] and multiple quadrupole-octupole system [151, 154]. At present, TEM/STEM instrument can be found with an image corrector, a probe corrector or a double corrector[14].

---

[14]Both image and probe correctors.

# Chapter 4

# Other techniques applied for characterization

To come closer to a complete characterization and understanding of aluminum alloys, it is important to combine the TEM characterization with other techniques. This chapter provides theory and principles of other techniques used in thesis, including hardness measurements (in Paper I, Paper II and Paper IV), conductivity measurements (in Paper IV), intergranular corrosion (IGC) testing (in Paper IV) and density functional theory (DFT) calculations (in Paper V).

## 4.1 Hardness measurements

Hardness is one parameter used to characterize materials, which represents "resistant of applied force". Numerical determination of a hardness value depends on the type of hardness test. There are three major tests, scratch, rebound and indentation. Vickers hardness, one of the indentation tests, is used to investigate the precipitation hardening. In the Vickers hardness measurement, varying the applied force on the test can give comparable hardness values on the same material, which is an unique feature compared to the other types of hardness testing [155]. Figure 4.1 shows schematic and indentation images for the Vickers hardness measurements.

The Vickers hardness value is calculated by dividing the applied force by the surface area of the indentation shown in the following [155]:

$$HV = \frac{F}{A} = \frac{2 \cdot \sin(\alpha/2)}{d^2} \qquad (4.1)$$

where $F$ stands for the applied force (kg), $A$ for the surface area of the indentation (mm$^2$), $\alpha$ for the angle of indicator (136°) and $d$ for the average length of diagonals in the square indentation.
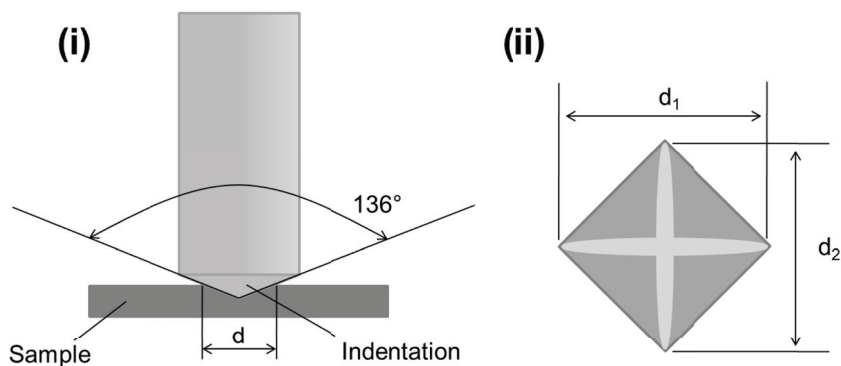
Figure 4.1: Schematic illustration of (i) the hardness indentation and (ii) the measurement of length of diagonals in the square indentation.

A Durascan-70 (Struers) machine is used for the Vickers hardness measurements in Paper I, Paper II and Paper IV to evaluate precipitation hardening. The hardness indenter is used with 5 kg load and a loading time for 15 seconds. Each data point corresponds to the average of ten hardness indentations, with the corresponding standard error. The measurements follow the ASTM E384 standard.

## 4.2  Conductivity measurements

Electric conductivity is one parameter used to describe the *mobility* of electrons. The mobility can be used to characterize precipitation of age-hardenable aluminum alloys. The conductivity depends on several factors: temperature, atoms in solid solution and precipitates. It is measured by Eddy currents, which is an easy, quick and convenient technique, compared to resistivity measurements which commonly use the four-point probe method [156]. Conductivity can be expressed as the inverse of the resistivity:

$$\sigma = 1/\rho \tag{4.2}$$

where $\sigma$ stands for electrical conductivity and $\rho$ for resistivity. The resistivity is greatly influenced by the temperature because of thermal vibration of the aluminum lattice. Known as the Matthiessen's rule [157], resistivity can be expressed as the sum of resistivity due to thermal vibrations in the lattice and other contri-

butions in the lattice. Assuming the other contributions are atoms in solid solution and precipitates in the case of age-hardenable aluminum alloys, resistivity can be expressed as follows [158]:

$$\rho = \rho_{pure}(T) + \sum_i \rho_i C_i + \rho_{ppt} \tag{4.3}$$

where $\rho_{pure}(T)$ stands for a contribution of the thermal vibrations of pure aluminum lattice at temperature $T$, the second summation term represents contributions from the specific resistivity of $i$th solute $\rho_i$, and concentration of this solute $C_i$, and $\rho_{ppt}$ stands for the contribution of precipitates.

In Paper IV, a SIGMATEST 2.069 operating at a frequency of 960 kHz is used. Each data point corresponds to the average of five conductivity measurements, with the corresponding standard error. Calibration of the machine is conducted several times during measurements at room temperature in order to minimize the error.

## 4.3   Intergranular corrosion (IGC)

Corrosion occurs due to electrochemical reactions in metallic materials. Corrosion resistance is one of the important properties for applications although aluminum alloys generally have high corrosion resistance. Among several different types of corrosion assumed in metallic materials, IGC is associated to precipitation in age hardenable aluminum alloys. IGC could result from diffusion of solute atoms towards and into grain boundaries [159]. IGC occurs due to a galvanic reaction adjacent to the grain boundaries. Grain boundary precipitates and/or solute atoms along the grain boundaries create an anode electrochemical potential. In general, aluminum alloys have good corrosion resistance – low susceptibility. However, the susceptibility varies with additional alloying elements and heat treatment conditions. For example, an addition of Cu in Al-Mg-Si alloys leads to IGC in under-aged conditions, but not peak hardness and over-aged conditions. This is because of Cu atoms diffuse to make a *Cu film* along grain boundaries during precipitation, but the film becomes discontinuous at peak hardness and over-aged conditions [160]. In addition, IGC susceptibility increases with increasing amounts of Cu in Al-Mg-Si alloys [161]. This example shows that it is important to investigate how solute elements diffuse associated with microstructure during precipitation.

In Paper IV, accelerated corrosion tests are conducted with a sodium chloride solution by following the British standard (BS 11846 method B). The IGC susceptibility is evaluated after the corrosion tests by optical microscopy.

## 4.4 Density functional theory (DFT) calculations

Density functional theory (DFT) is a standard theoretical framework for quantum mechanical calculations, performed to investigate the electronic structure in a condensed matter system. This enables electronic properties, e.g. energies of the system, to be calculated from information on the electron density. DFT is applied to calculate formation enthalpies of the $\beta''$ phase with Zn incorporation in Al-Mg-Si alloys in Paper V. The actual DFT calculations have not been done by the author. The principles of the theory and calculations are briefly described in the following.

It is complicated to determine three dimensional electron wave functions in a many body system. DFT has been developed to make this problem feasible. The properties of a many body system are determined by functionals of the electron density [162, 163], based on the Hohenberg-Kohn theorems [162]. The Hohenberg-Kohn theorems contain two-folds. First, the electron density for a system in its ground state can be used to determine the external potentials acting on the electrons. In other words, the ground state electron density uniquely corresponds to the external potentials. Second, for any external potential, a functional of the electron density can be determined. In addition, this functional[1] takes a minimum energy in the ground state of that given external potential. Based on the theorems, electronic properties can be calculated by the Schrödinger equation. The scheme underlying actual calculation is called the *Kohn-Sham equations* [163]:

$$\left(-\frac{\hbar^2}{2m}\nabla^2 + v_{eff}(\vec{r})\right)\phi_i(\vec{r}) = \epsilon_i\phi_i(\vec{r}) \tag{4.4}$$

where $\hbar$ stands for the Planck constant divided by $2\pi$, the Kohn-Sham orbital corresponding to orbital energy $\epsilon_i$, is called $\phi_i$. It can express the electron density of a N-body system as follows:

$$\rho(\vec{r}) = \sum_i^N \mid \phi_i(\vec{r}) \mid^2 \tag{4.5}$$

The effective potential at the position $\vec{r}$, $v_{eff}(\vec{r})$ is represented by a functional of the electron density as follows:

$$v_{eff}(\vec{r}) = v_{ext}(\vec{r}) + e^2 \int \frac{\rho(\vec{r'})}{r - r'}d\vec{r'} + v_{xc}(\vec{r}) \tag{4.6}$$

where $v_{ext}(\vec{r})$ is the external potential (from the nuclei) acting on the electrons and $v_{xc}(\vec{r})$ is the exchange-correlation potential.

---

[1]This is sometimes called the HK (*H*ohenberg*K*ohn) functional.

The total energy of the system can now be expressed as a functional of the electron density as follows:

$$E[\rho] = T_s[\rho] + \int v_{ext}(\vec{r})\rho(\vec{r})d\vec{r} + V_H + E_{xc}[\rho] \qquad (4.7)$$

where $T_s$ is the kinetic energy[2], $V_H$ is the Coulomb energy and $E_{xc}$ is the exchange-correlation energy which must be approximated in practical studies.

In Paper V, DFT calculations are applied to calculate the *energy gain* for Zn incorporation into the $\beta''$ phase, relative to Zn atoms in solid solution. These studies may describe how Zn atoms stabilize on a particular site in the $\beta''$ phase. The actual calculation have been performed using the plane wave based Vienna Ab-initio Simulation Package (VASP) [164, 165], employing Vanderbilt ultrasoft pseudopotentials [166]. The plane wave based calculation is assuming periodic potentials of crystals i.e. the Bloch waves approach as partially described in section 3.6. This enables the calculation in the reciprocal space, making it faster by the use of FFT algorithms. In addition the pseudopotential replaces the core electrons, reducing the size of the problem greatly. The exchange-correlation energy in Paper V is described by the Perdew-Wang generalized gradient approximation [167].

The DFT calculations have often been applied for investigations of Al-Mg-Si alloys. The following are examples where DFT calculations have contributed: determination of formation enthalpies for several metastable phases [168], determination of the lowest energy configuration of the $\beta''$ phase [39] and investigation of interface structures for the $\beta''$ phase [41].

---

[2]It is called the Kohn-Sham kinetic energy.

# Part II

# Papers

# Paper I

**The effects of quench rate and pre-deformation on precipitation hardening in Al-Mg-Si alloys with different Cu amounts**

Takeshi Saito, Calin D. Marioara, Jostein Røyset, Knut Marthinsen and Randi Holmestad
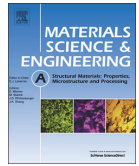
# The effects of quench rate and pre-deformation on precipitation hardening in Al–Mg–Si alloys with different Cu amounts

Takeshi Saito [a,*], Calin D. Marioara [b], Jostein Røyset [c], Knut Marthinsen [d], Randi Holmestad [a]

[a] Department of Physics, Norwegian University of Science and Technology (NTNU), N-7491 Trondheim, Norway
[b] SINTEF Materials and Chemistry, N-7465 Trondheim, Norway
[c] Hydro Aluminum Research and Technology Development, N-6601 Sunndalsøra, Norway
[d] Department of Materials Science and Engineering, Norwegian University of Science and Technology (NTNU), N-7491 Trondheim, Norway

## ARTICLE INFO

## ABSTRACT

The effects of quench rate after solution heat treatment in combination with 1% pre-deformation on precipitation hardening in three Al–Mg–Si alloys have been investigated by transmission electron microscopy and hardness measurements during an isothermal heat treatment. The alloys contain different Cu amounts (up to 0.1 wt%) and the same amounts of other solute elements. While a Cu amount below 0.01 wt% does not affect precipitation hardening, an addition of 0.1 wt% Cu increases hardness due to the formation of a fine microstructure having a high number density of short precipitates. A double peak hardness evolution was observed during isothermal heat treatment. This effect was most pronounced for alloys with low quench rate, and less pronounced for alloys with 1% pre-deformation and 0.1 wt% Cu addition. The low quench rate also led to wider precipitation free zones. This effect was also less pronounced by 1% pre-deformation and addition of 0.1 wt% Cu.

© 2014 Elsevier B.V. All rights reserved.

## 1. Introduction

The 6xxx series of Al alloys (i.e., Al–Mg–Si alloys) are predominant heat-treatable materials used in a wide range of industrial applications. A commercial interest in the 6xxx series has strongly been attracted on the basis of their characteristic properties: high strength-to-weight ratio, good formability and high corrosion resistance. Their main specific feature is a significant increase in hardness due to the formation of a large number of nano-sized, (semi-)coherent, metastable precipitates during isothermal heat treatment, which yield interfacial strain into the Al matrix. The interfacial strain eventually makes dislocations shearing and/or looping on precipitates to prevent their movements (the latter is known as the Orowan mechanism [1]), depending on size and distribution of precipitates. Hence, mechanical properties of the alloys depend highly on the microstructure. The precipitates form in alloys with relatively low amounts of solute elements (typically up to a total of 2 wt% of Mg and Si) which become supersaturated in the Al lattice after solution heat treatment. Quenching (rapid cooling) from the solution heat treatment creates quenched-in vacancies which promote diffusion of solute elements into clusters and their growth into metastable precipitates during the following isothermal heat treatment.

The precipitation sequence in the Al–Mg–Si alloys is as follows [2–10]:

$$SSSS \rightarrow atomic\ clusters \rightarrow GP\ zones(pre-\beta'') \rightarrow \beta'' \rightarrow \beta',$$

$$U1(Type-A),\ U2(Type-B),\ B'(Type-C) \rightarrow \beta, Si$$

where SSSS stands for super saturated solid solution. The main hardening precipitates are the highly coherent, needle-shaped GP zones and $\beta''$ which form the finest microstructure at peak hardness. The post-$\beta''$ phases are semi-coherent rods/laths and produce coarser precipitate microstructures with a lower strength contribution. All needles/rods/laths have their main growth direction along $\langle 001 \rangle$Al. The precipitate microstructure and types are determined by alloy composition and thermo-mechanical treatment.

It was previously demonstrated [11] that a low Cu addition ($\sim$0.1 wt%) does not alter the precipitation sequence in the Al–Mg–Si alloy system, although this level of Cu leads to higher strength by means of forming a higher number density of shorter precipitates having a partially disordered structure [11,12]. Aluminum recycling is increasing. Since Cu is one of the trace elements that can be accumulated in the scrap base during recycling, it is relevant to investigate the effects of low Cu additions.

* Corresponding author: Tel.: +47 73 59 07 30.
  *E-mail address:* takeshi.saito@ntnu.no (T. Saito).

The SSSS is reached when the alloy is solution heat treated and subsequently cooled or quenched to room temperature at a rate fast enough to avoid significant precipitation. It has previously been reported that slow quench rates influence the formation of grain boundary precipitates [13] and cause an increase in the width of precipitate free zone (PFZ), leading to intergranular fracture [14] in some Al–Mg–Si alloys. Slower quench rates also lead to lower strength [15] because of loss of quenched-in vacancies [16] which are essential for the atomic diffusion during precipitation and their concentration decides the precipitation hardening behavior [17–20]. It was recently demonstrated [21] that quenching into temperatures ~160 °C (interrupted quenching) enhances precipitation kinetics and increases overall hardness due to an increase in mobile vacancies which promotes clusters transforming to β″. Another report [22] showed that slow cooling leads to less precipitate number densities because of loss of quenched-in vacancies. Although natural aging (room temperature storage before the isothermal heat treatment) time generally influences the type of atomic clusters and consequently mechanical properties after precipitation [23,24], the slow cooling leads to lower influences on the effects of natural aging [22]. Investigations of effects of quench rates are important since a fast quenching is not always possible in industrial processes because of, e.g., limitations of the production equipment, or restrictions on shape changes that may be introduced by residual stress if the materials are quenched.

It is known that deformation between solution heat treatment and artificial aging affects precipitation. Since the deformation is conducted before further isothermal heat treatment, it is called 'pre-deformation'. Nucleation rates and precipitation kinetics are enhanced since the pre-deformation decreases activation energy

of the growth of precipitates [25,26]. It has been reported [27–31] that 10%–15% pre-deformation leads to formation of heterogeneous nucleation along dislocation lines. After artificial aging, different types of precipitates (except for β″) form: a continuous decoration of the dislocation lines ('string-like' precipitates) together with discrete precipitation consisting mainly of B′ [27–30], and together with (often disordered) Q′ [11,12,31,32] if Cu is present in the Al–Mg–Si alloys. In the case of 0.5%–5% pre-deformation, β″ is dominant at peak hardness condition, and this level of pre-deformation accelerates the formation of β″ due to decreased activation energy [33–36]. This can be attributed to the fact that the formation of atomic clusters transforming to β″ is enhanced during natural aging due to the pre-deformation [37]. Investigation of ~1% pre-deformation is relevant in industrial practice where the pre-deformation is applied to straighten the workpiece, e.g., after extrusion.

The effects of low Cu additions, quench rates and pre-deformation on precipitation hardening in Al–Mg–Si alloys must be due to modified atomic diffusion rates and quenched-in vacancy concentrations during thermo-mechanical treatment. The objective of the present work is hence how these factors influence precipitation hardening. In this study, the effects of low Cu additions (up to 0.1 wt%), quench rates and 1% pre-deformation on precipitation hardening in Al–Mg–Si alloys have been systematically investigated by hardness measurements and transmission electron microscopy (TEM).

## 2. Experimental procedure

Three alloys with different amounts of Cu (0.001, 0.01 and 0.1 wt%), but with fixed levels of Mg and Si, were used. The alloy compositions were measured by inductively coupled plasma optical emission spectroscopy and are shown in Table 1. Hereafter the alloys with different increasing amounts of Cu will be referred to as LC1, LC2 and LC3, respectively, as shown in Table 1. Although the three alloys contain Fe, the level (~0.07 wt%) was considered to be representative for the lowest practical Fe-level to be expected in industrial alloys. The alloys were cast as ⌀95 mm cylindrical ingots, from which extrusion billets were cut. The billets were homogenized at 575 °C for 2.5 h and cooled. The billets were subsequently extruded

**Table 1**
Alloy composition (wt%) for the three alloys studied, measured by inductively coupled plasma optical emission spectroscopy.

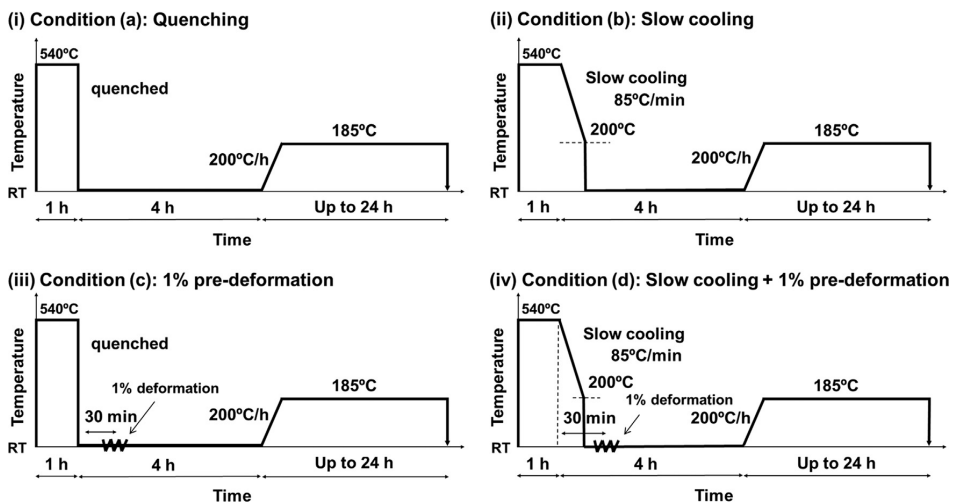| Alloy | Al | Mg | Si | Fe | Cu | Other |
|-------|------|------|------|-------|-------|-------|
| LC1 | Bal. | 0.50 | 0.42 | 0.071 | 0.001 | 0.000 |
| LC2 | Bal. | 0.47 | 0.41 | 0.078 | 0.010 | 0.000 |
| LC3 | Bal. | 0.48 | 0.41 | 0.072 | 0.093 | 0.000 |



**Fig. 1.** Thermo-mechanical histories for (i) condition (a): quenching, (ii) condition (b): slow cooling, (iii) condition (c): 1% pre-deformation and (iv) condition (d): combination with the slow cooling and the 1% pre-deformation after solution heat treatment. The alphabetic designations correspond to Figs. 2, 4, 5, 7 and 8.

to ⌀20 mm round profiles. The extrusion was conducted using a direct press and a single-hole die. The billet preheating temperature was 500–510 °C which was well above the solvus temperature for the alloys, and the extruded profiles were water-quenched approximately 5 s after the die exit. The extruded profiles were cut into lengths of 50 cm. Hence, all the samples were round bars with ⌀20 mm in length of 50 cm. The samples were solution heat treated at 540 °C for 1 h an air circulation oven. There were four different thermo-mechanical treatments conducted after the solution heat treatment: (a) water quenching (b) slow cooling (the cooling rate was 85 °C/min until 200 °C was reached, and then the sample was quenched), (c) water quenching and then 1% pre-deformation after 30 min and (d) slow cooling and 1% pre-deformation after 30 min. Hereafter these conditions will be referred to as conditions (a), (b), (c) and (d), respectively, as shown in Fig. 1. The cooling rate in conditions (b) and (d) were measured by a K-type thermo couple in the middle of the samples. The alloys were then exposed to room temperature (i.e., natural aging) for a total of 4 h after the solution heat treatment. Subsequently the alloys were heat treated isothermally (i.e., artificial aging) at 185 °C in an air circulation oven. The thermo-mechanical treatments for all the conditions are shown in Fig. 1. Only the middle part of the samples (where the 1% pre-deformation was expected to be homogeneous) was used for further characterization for conditions (c) and (d).

Vickers hardness measurements were carried out on the cross-sectional surface of slices cut transversal to the extrusion direction. A Struers Durascan-70 machine was used for the hardness measurement. The hardness indenter was used with 5 kg load and a loading time of 15 s. Each data point corresponds to the average of ten hardness indentations, with the corresponding standard error.

TEM specimens were prepared by electro polishing with a Tenupol 5 machine (Struers, Denmark), on the transversal slices used for the hardness measurements. The electrolyte consisted of 1/3 HNO₃ in methanol and the solution was kept at temperatures between −20 °C and −35 °C.

Investigations of precipitate microstructure were performed by TEM in bright-field mode using a Philips CM30 operating at 150 kV. A Gatan parallel electron energy loss spectroscopy (PEELS) was used to measure the thickness of the specimens, i.e., in the center of the area used in each image. All the TEM and PEELS analyses were performed with the incident electron beam along the ⟨001⟩ Al directions where approximately 1/3 of the needles can be viewed in cross-section and 2/3 can be imaged perpendicular to the precipitate needle lengths. A combination of the bright-field TEM images with corresponding thicknesses enabled average precipitate needle-lengths, cross-sections, number densities and volume fractions to be quantified. A full description of the methodology has been given elsewhere [5,38]. The total number of precipitate lengths and cross-sections measured were roughly 2000 and 700, respectively, for the statistical analysis in each thermo-mechanical condition. Widths of precipitate free zone (PFZ) adjacent to grain boundaries were measured from the TEM bright-field images.

# 3. Results

## 3.1. Hardness curves

Fig. 2 shows hardness curves as a result of isothermal heat treatment at 185 °C for different times up to 24 h for the LC1, LC2 and LC3 alloys for the different thermo-mechanical treatments described in Fig. 1. The following are the observations from Fig. 2.

- The overall hardness of the LC3 alloys is consistently higher than that of the LC1 and LC2 alloys in all conditions. This suggests that a 0.1 wt% Cu addition significantly increases the

hardness, which is in good agreement with previous results [11]. This strength increase is more pronounced when peak hardness is reached as compared to the early stages of precipitation. The main reason for this difference must be the different hardness contributions: mainly solute hardening at early stages, while a gradual precipitation hardening increases towards the peak hardness.

- During the early stages of clustering/precipitation (before 2 h of isothermal heat treatment), the hardness increases faster in the LC3 alloy in all conditions as compared to the LC1 and LC2 alloys, which indicates an accelerated precipitation kinetics due to 0.1 wt% Cu.
- Hardness curves for the LC1 and LC2 alloys are similar for all conditions. This suggests that a level of Cu additions of 0.01 wt% and below does not affect the precipitation hardening.
- The maximum hardness reached for each alloy is almost similar regardless of the quench rate and the 1% pre-deformation, although it was slightly lower in conditions (c) and (d). Faster hardness evolution was observed in the early stage for conditions (c) and (d), which indicates accelerated precipitation kinetics in the 1% pre-deformed conditions.
- A tendency to double peak hardness evolution is observed in the LC1 and LC2 alloys in all conditions, being most pronounced in condition (b). This effect is weaker in the LC3 alloy.
- The onset of the first hardness peak seems to be delayed for the LC1 and LC2 alloys in conditions (c) and (d), and its value is higher than that of the second peak.
- In condition (b), hardness starts decreasing after about 9 h of aging for all alloys as compared to the other conditions, which indicates a faster over-aging.

## 3.2. Precipitate microstructure and precipitate free zone (PFZ)

The microstructure of the LC1 and LC3 alloys for 2 and 12 h of isothermal heat treatment was investigated by bright-field TEM (the respective isothermal heat treatment times are indicated by vertical dashed lines in the hardness curves in Fig. 2). Representative examples of bright-field TEM images are shown in Fig. 3. Precipitates are present in the form of needle shape with the main growth direction along ⟨001⟩Al. The precipitates were identified to be mostly β″ in the LC1 alloy and to be in coexistence with β″ with a partially disordered structure in the same precipitate needle in the LC3 alloy at peak hardness condition [11]. The corresponding precipitate statistics (needle lengths, number densities, cross sections and volume fractions) are summarized in Figs. 4 and 5. In all conditions, the LC3 alloy has finer precipitate microstructure characterized by higher number densities of shorter precipitates and consequently higher volume fractions as compared to the LC1 alloy. Apart from this observation, tendencies of the differences in the precipitate statistics depend on each thermo-mechanical condition – but are qualitatively the same, irrespective of the amount of Cu, see dashed lines for the corresponding conditions in Figs. 4 and 5. Increases in needle lengths and cross-sections between 2 and 12 h of isothermal heat treatment were most pronounced in condition (b) as compared to the other conditions. As a consequence, increases in volume fractions were also most pronounced in condition (b), since volume fraction is related to needle length, cross-section and number density. Here, a very slight increase in number densities for the LC1 alloy and a decrease for the LC3 alloy can be observed between 2 and 12 h of isothermal heat treatment. These observations indicate faster over-aging in condition (b). This is in good agreement with the observations from the hardness curves shown in Fig. 2. Needle lengths and cross-sections in conditions (c) and (d) were longer and larger, respectively, than those in conditions (a) and (b) for both alloys.
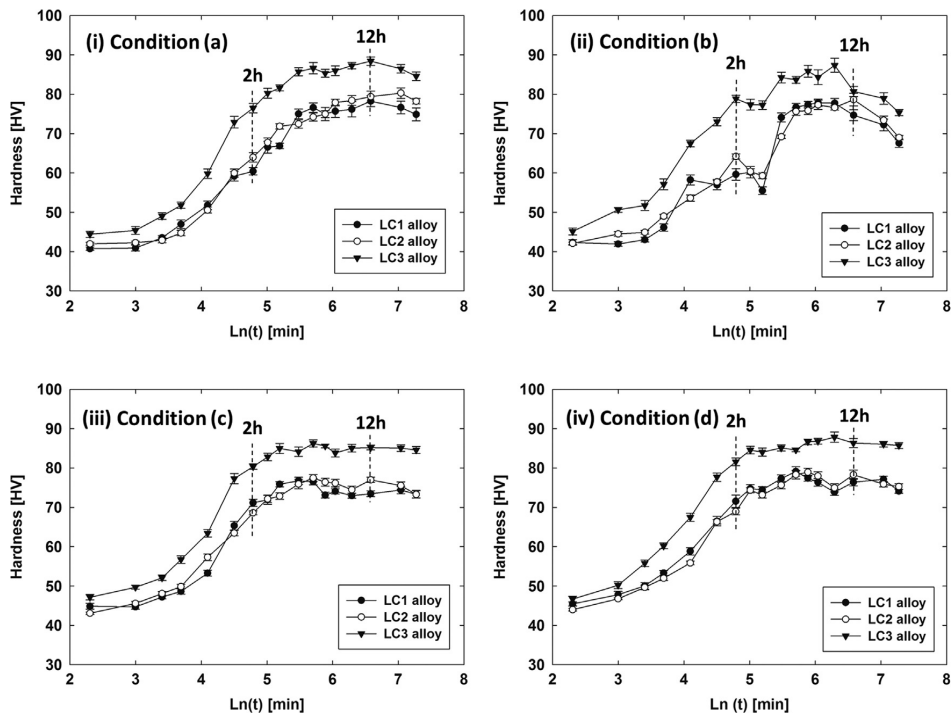
**Fig. 2.** Hardness curves as a function of isothermal heat treatment times for the LC1, LC2 and LC3 alloys for (i) condition (a), (ii) condition (b), (iii) condition (c) and (iv) condition (d). The alphabetic designations for the thermo-mechanical treatments correspond to Fig. 1. The alloy designations correspond to Table 1.
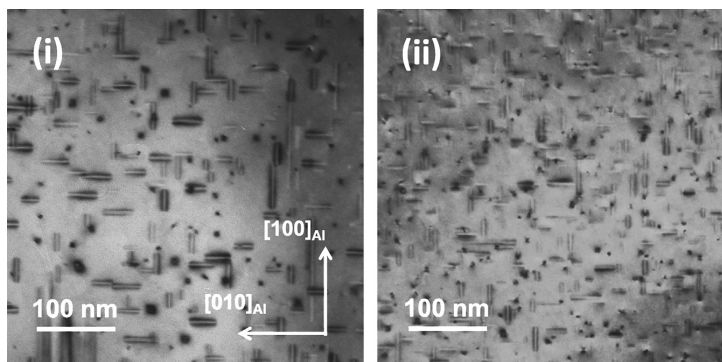


**Fig. 3.** Examples of bright-field TEM images, which were used for taking precipitate statistics shown in Figs. 4 and 5. The images shown were taken along ⟨001⟩Al for (i) the LC1 and (ii) the LC3 alloys after isothermal heat treatment for 2 h in condition (a). The images are recorded in areas with similar thicknesses (50–70 nm) and with the same scale. Dark spots represent cross sections of the needle-shaped precipitates in the viewing direction.

This shows that the 1% pre-deformation leads to faster growth of the precipitates.

Widths of PFZs adjacent to grain boundaries were measured from bright-field TEM images for each alloy and each condition. Examples of the PFZs on the TEM images are shown in Fig. 6 and measurements of the widths of the PFZs are summarized in Fig. 7. The PFZ widths in the LC3 alloys were narrower than those in the LC1 alloys for all conditions. This indicates that the Cu addition (~0.1 wt%) leads to a reduction of the PFZs. In conditions (b) and (d), wider PFZs were observed as compared to conditions (a) and (c). This is a typical effect of the slow cooling on the PFZs [14]. However, the widths in

condition (d) were slightly narrower than those in condition (b), which may be attributed to the 1% pre-deformation applied in condition (d).

## 4. Discussion

It is demonstrated that the influence of a Cu content of 0.01 wt% and below on hardness is negligible; the hardness curves for the LC1 and LC2 alloys were similar even including a distinct double peak hardness evolution in condition (b). However a Cu content
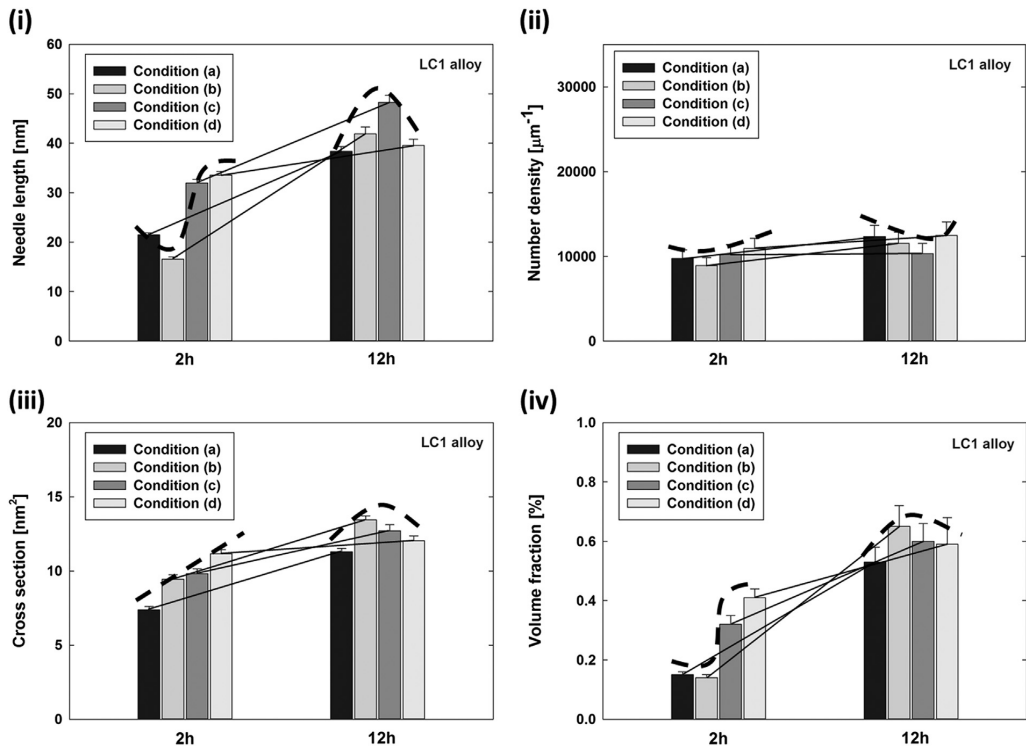
**Fig. 4.** Precipitate statistics for the LC1 alloy after isothermal heat treatment for 2 and 12 h in all conditions, calculated from a combination of bright-field TEM images and thicknesses measured by EELS. (i) Needle lengths, (ii) number densities, (iii) cross sections and (iv) volume fractions. The alphabetic designations for the thermo-mechanical treatments correspond to Fig. 1. The alloy designations correspond to Table 1. Solid lines connect each condition for 2 and 12 h of isothermal heat treatment. Dashed lines represent tendencies of differences in each condition.

of ∼0.1 wt% significantly affects the hardness in all the thermomechanical treatments. The addition of ∼0.1 wt% Cu leads to higher hardness corresponding to higher number densities of shorter precipitates, which is in good agreement with our previous study [11]. Interestingly, these observations were made not only for the quenched condition (condition (a)) but also for the slow cooling, the 1% predeformation and combination of these conditions (conditions (b), (c) and (d)).

The exact cause of the double peak hardness evolution could not be determined with the experimental data acquired in this work. However, a similar double peak has previously been reported [5,39,40], although it was in a denser alloying element, a Si-rich alloy in a quenched condition, which was related to the formation of an earlier phase, called pre-β″. Namely, the double peak corresponds to a transition of pre-β″ to β″ precipitates. The observed double peak hardness evolution in the present study could also be due to the same transition. It is noteworthy that it was observed in leaner, more Mg-rich alloys in slow cooling condition in the present study. The slow cooling, which generally leads to a lower quenched-in vacancy concentration, made this peak pronounced (condition (b)). It may be speculated that the formation of β″ precipitates could be delayed because of lower vacancy concentrations creating a low nucleation rate for β″ precipitates. As a consequence, a distinct double peak and corresponding increase in needle lengths and cross-sections could be observed in condition (b). The slow cooling rate also makes overaging faster, which could be explained by lower vacancy concentrations (less atomic diffusion) to grow β″ precipitates for long aging time because of a lack of available solute elements. These

explanations can be supported by the fact that quench-in vacancies are required in the formation of β″, i.e., they form clusters transforming to β″ [21]. Interestingly, a combination of slow cooling rate and 1% pre-deformation (condition (d)) makes the double peak hardness evolution less pronounced. This may indicate that the formation of β″ precipitates in condition (d) is faster than that in condition (b). It has been reported [33–36] that predeformation leads to acceleration of the formation of β″ precipitates, which is due to reduced activation energy. It is plausible to suggest that the 1% pre-deformation leads to faster atomic diffusion and growth of β″ precipitates, which can also be supported from the observation of the faster hardness evolutions in conditions (c) and (d), see Fig. 2. These observations indicate that the double peak is less pronounced when more energy is added to the system: either in the form of more quenched-in vacancies, predeformation or a combination of both, which promote atomic diffusion leading to the formation of β″. These explanations are illustrated in Fig. 8.

Cu makes the effect of the double peak hardness less pronounced. This might be related to the observation that Cu is not entering the β″ phase, but rather forms its own disordered structures [11,12] which are less coherent with lower bulk energies. In addition, Cu makes higher number density of precipitates. These might make them less susceptible to the available vacancy amounts. It is suggested that Cu could make a compensation of low vacancy concentrations to make the double peak hardness less pronounced.

1% pre-deformation did not lead to a significant increase in hardness, as compared to, e.g., 10%–15% pre-deformation [11,27,28].
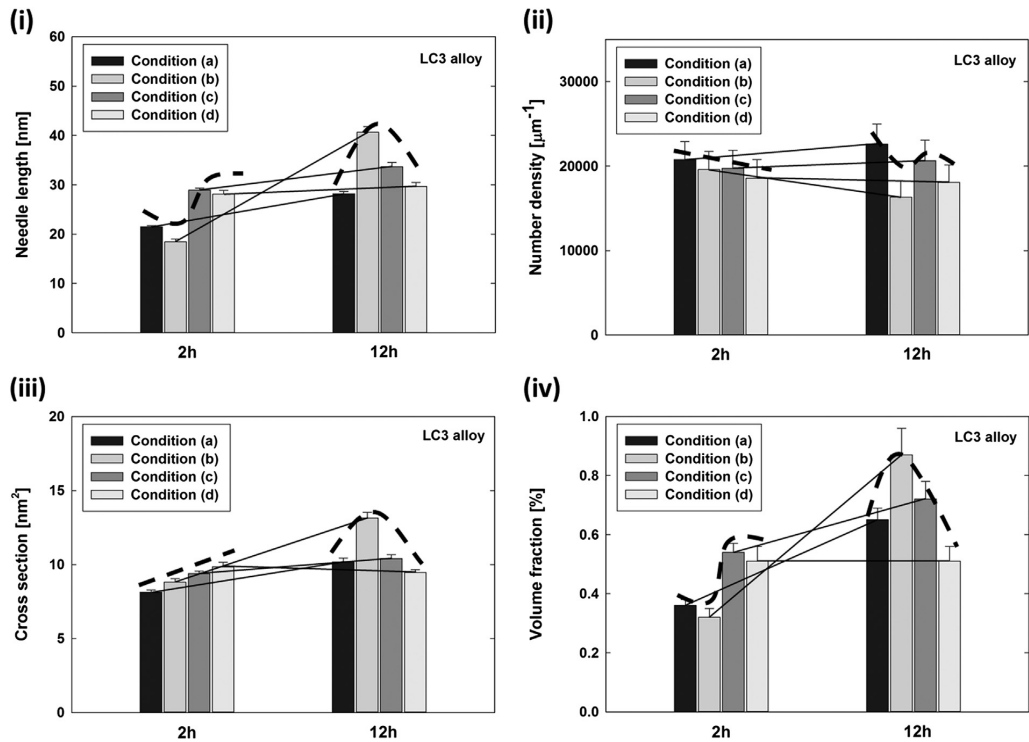
**Fig. 5.** Precipitate statistics for the LC3 alloy after isothermal heat treatment for 2 and 12 h in all conditions, calculated from a combination of bright-field TEM images and thicknesses measured by EELS. (i) Needle lengths, (ii) number densities, (iii) cross sections and (iv) volume fractions. The alphabetic designations for the thermo-mechanical treatments correspond to Fig. 1. The alloy designations correspond to Table 1. Solid lines connect each condition for 2 and 12 h of isothermal heat treatment. Dashed lines represent tendencies of differences in each condition.
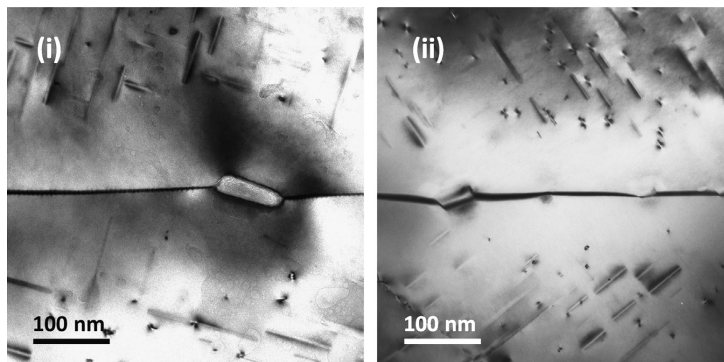


**Fig. 6.** Examples of PFZs adjacent to a grain boundary taken by bright-field TEM images. The images shown were taken for (i) the LC1 alloy and (ii) the LC3 alloy after isothermal heat treatment for 12 h in condition (a). Precipitate needles and a grain boundary precipitate can be seen on grains and on the grain boundary, respectively. The images were recorded at the same scale.

It is suggested that the level of pre-deformation (∼1%) does not give any notable work-hardening effect because of the relatively low dislocation densities, consistent also with the fact that the hardness in the as-quenched stage is almost the same in all conditions. However, these dislocations *affect* atomic nucleation and precipitation, which is probably because they promote faster atomic diffusion in the 1% pre-deformed conditions. The 1% pre-deformation could potentially compensate the negative effects of slow cooling rate on

the alloy properties. For example, it *reduced* the effect of over-aging and of wider PFZs due to the slow cooling rate, as shown in the present study.

As mentioned, it is worth noting that Cu addition (∼0.1 wt%) made PFZs narrower. A similar observation was reported in an alloy having ∼0.5 wt% Cu [41], and also Ag in Al–Zn–Mg alloys [42]. This was because Ag has a strong interaction with other alloying elements, which prevents solute depletion adjacent to

**Fig. 7.** Widths of PFZ for (i) the LC1 and (ii) the LC3 alloys after isothermal heat treatment for 2 and 12 h in all conditions. The alphabetic designations for the thermo-mechanical treatments correspond to Fig. 1. The alloy designations correspond to Table 1.
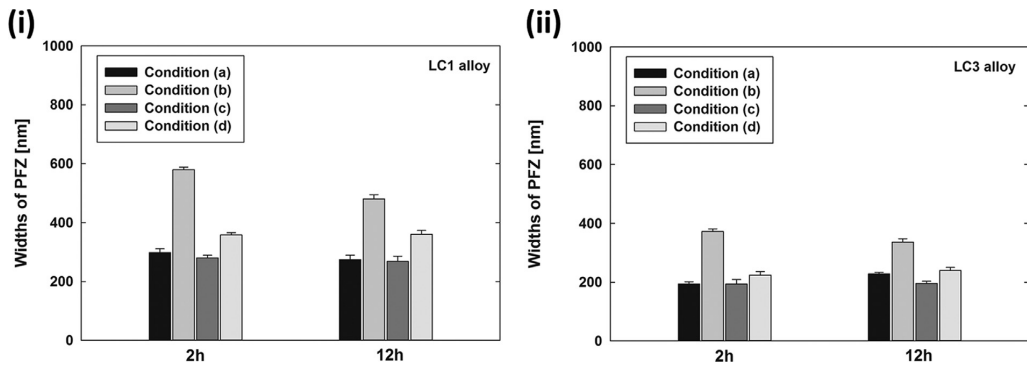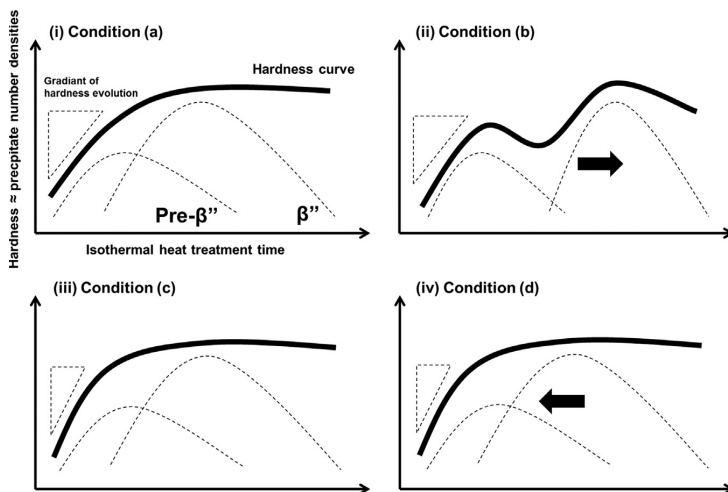


**Fig. 8.** Schematic images of hardness curves corresponding to the formation of pre-β″ and β″ precipitates for different thermo-mechanical treatments: (i) condition (a), (ii) condition (b), (iii) condition (c) and (iv) condition (d). The alphabetic designations correspond to Fig. 1. Dashed triangles and lines represent gradient of hardness evolutions at early stages of precipitation and number of pre-β″ and β″ precipitates, respectively. An increase in hardness is related to number densities of the precipitates.

grain boundaries, i.e., the critical vacancy concentrations for nucleation decreases [42]. It can be suggested that the ~0.1 wt% Cu addition also leads to decreasing the critical vacancy concentrations for nucleation in the region adjacent to grain boundaries since Cu can make high number densities of precipitates [11] due to own preferential atomic configuration [12]. These observations suggest that Cu additions could also compensate the effects of slow cooling rate on the alloy properties.

## 5. Conclusion

The influences of Cu additions (up to 0.1 wt%), quench rate and 1% pre-deformation on precipitation hardening in Al–Mg–Si alloys have been investigated. The highest Cu addition increases hardness of alloys with higher number densities of shorter precipitates, and reduces the width of PFZs. The effects of Cu were independent of the quench rate and the 1% pre-deformation. A double hardness peak observed during isothermal heat treatment is most probably due to the transition of pre-β″ to β″ precipitates, which was most pronounced in the slow cooling condition and less pronounced in

the alloy with 0.1 wt% Cu. 1% pre-deformation also made this effect less pronounced. These observations may be due to lower vacancy concentration in the slow cooling condition leading to a delayed formation of β″ precipitates. Moreover, the Cu addition and 1% pre-deformation compensate for the delay due to faster atomic diffusion. Maximum hardness is affected by 0.1 wt% Cu addition, but it is independent of thermo-mechanical treatments: slow cooling, 1% pre-deformation and a combination of these. Although the slow cooling led to wider PFZs, this effect was less pronounced by the 1% pre-deformation and 0.1 wt% Cu addition. These observations can also be explained by faster atomic diffusion due to the 1% pre-deformation and 0.1 wt% Cu addition.

## References

[1] E. Orowan, The Institute of Metals, London, Symposium on Internal Stresses in Metals and Alloys, 1948, pp. 451–453.
[2] G.A. Edwards, K. Stiller, G.L. Dunlop, M.J. Couper, Acta Mater. 46 (1998) 3893–3904.
[3] S.J. Andersen, H.W. Zandbergen, J. Jansen, C. Træholt, U. Tundal, O. Reiso, Acta Mater. 46 (1998) 3283–3298.
[4] H.S. Hasting, A.G. Frøseth, S.J. Andersen, R. Vissers, J.C. Walmsley, C.D. Marioara, F. Danoix, W. Lefebvre, R. Holmestad, J. Appl. Phys. 166 (2009) (123527-1–123527-9).
[5] C.D. Marioara, S.J. Andersen, H.W. Zandbergen, R. Holmestad, Metall. Mater. Trans. A 36 (2005) 691–702.
[6] C.D. Marioara, H. Nordmark, S.J. Andersen, H.W. Zandbergen, R. Holmestad, J. Mater. Sci. 41 (2006) 471–478.
[7] R. Vissers, M.A. van Huis, J. Jansen, H.W. Zandbergen, C.D. Marioara, S.J. Andersen, Acta Mater. 55 (2007) 3815–3823.
[8] S.J. Andersen, C.D. Marioara, R. Vissers, A. Frøseth, H.W. Zandbergen, Mater. Sci. Eng. A 444 (2007) 157–169.
[9] S.J. Andersen, C.D. Marioara, A. Frøseth, R. Vissers, H.W. Zandbergen, Mater. Sci. Eng. A 390 (2005) 127–138.
[10] K. Matsuda, Y. Sakaguchi, Y. Miyata, Y. Uetani, T. Sato, A. Kamio, S. Ikeno, J. Mater. Sci. 35 (2000) 179–189.
[11] T. Saito, S. Muraishi, C.D. Marioara, S.J. Andersen, J. Røyset, R. Holmestad, Metall. Mater. Trans. A 44 (2013) 4124–4135.
[12] T. Saito, C.D. Marioara, S.J. Andersen, W. Lefebvre, R. Holmestad, Philos. Mag. 94 (2014) 520–531.
[13] D. Steele, D. Evans, P. Nolan, D.J. Lloyd, Mater. Charact. 58 (2007) 40–45.
[14] M. De Haas, T. Th., M. De Hosson, J. Mater. Sci. 37 (2002) 5065–5073.
[15] J.L. Cavazos, R. Colás, Mater. Sci. Eng. A 363 (2003) 171–178.
[16] J.W. Evancho, J.T. Staley, Metall. Trans. 5 (1974) 43–47.
[17] L.A. Girifalco, H. Herman, Acta Metall. 13 (1965) 583–590.
[18] S. Hirosawa, T. Sato, J. Yokota, A. Kamio, Mater. Trans. JIM 39 (1998) 139–164.
[19] H.S. Zurob, H. Seyedrezai, Scr. Mater. 61 (2009) 141–144.
[20] S. Pogatscher, H. Antrekwitch, H. Leitner, T. Ebner, P.J. Uggowitzer, Acta Mater. 59 (2011) 3352–3363.
[21] S. Pogatscher, H. Antrekwitch, H. Leitner, D. Poschmann, Z.L. Zhang, P.J. Uggowitzer, Acta Mater. 60 (2012) 4496–4505.
[22] K. Strobel, M.A. Easton, L. Sweet, N.C. Parson, Proceedings of 13th International Conference on Aluminum Alloys (ICAA13), 3–7 June 2012, Pittsburgh, USA, isbn:978-1-118-45804-4, pp. 1187–1192.
[23] M. Torsæter, H.S. Hasting, W. Lefebvre, C.D. Marioara, J.C. Walmsley, S.J. Andersen, R. Holmestad, J. Appl. Phys. 108 (2010) (073527-1–073527-9).
[24] J. Røyset, T. Stene, J.A. Saeter, O. Reiso, Mater. Sci. Forum 519–521 (2006) 239–244.
[25] H.J. Rack, Mater. Sci. Eng. 29 (1977) 179–188.
[26] H.-L. Lee, W.-H. Lu, S.L. Chan, Scr. Metall. Mater. 25 (1991) 2165–2170.
[27] K. Matsuda, H. Gamada, Y. Uetani, S. Rengakuji, F. Shinagawa, S. Ikeno, J. Jpn. Inst. Light Met. 48 (1998) 471–475.
[28] K. Matsuda, S. Shimizu, H. Gamada, Y. Uetani, F. Shinagawa, S. Ikeno, J. Soc. Mater. Sci. Jpn. 49 (1999) 10–15.
[29] K. Teichmann, C.D. Marioara, S.J. Andersen, K.O. Pedersen, S. Gulbrandsen-Dahl, M. Kolar, R. Holmestad, K. Marthinsen, Philos. Mag. 91 (2011) 3744–3754.
[30] K. Teichmann, C.D. Marioara, S.J. Andersen, K. Marthinsen, Metall. Mater. Trans. A 43 (2012) 4006–4014.
[31] R.S. Yassar, D.P. Field, H. Weiland, Scr. Mater. 53 (2005) 299–303.
[32] R.S. Yassar, D.P. Field, H. Weiland, Metall. Mater. Trans. A 36 (2005) 2059–2065.
[33] G.K. Quainoo, S. Yannacopoulos, J. Mater. Sci. 39 (2004) 6495–6502.
[34] Y. Birol, Scr. Mater. 52 (2005) 169–173.
[35] Y. Birol, M. Karlik, Scr. Mater. 55 (2006) 625–628.
[36] T. Matsuda, Y. Takaki, T. Sakurai, S. Hirosawa, Mater. Trans. 51 (2010) 325–332.
[37] A. Serizawa, T. Sato, M.K. Miller, Mater. Sci. Eng. A 561 (2013) 492–497.
[38] S.J. Andersen, Metall. Mater. Trans. A 26 (1995) 1931–1938.
[39] C.D. Marioara, S.J. Andersen, J. Jansen, H.W. Zandbergen, Acta Mater. 49 (2001) 321–328.
[40] C.D. Marioara, S.J. Andersen, J. Jansen, H.W. Zandbergen, Acta Mater. 51 (2003) 789–796.
[41] K. Matsuda, K. Kido, T. Kawabata, Y. Uetani, S. Ikeno, J. Jpn. Inst. Light Met. 53 (2003) 528–533.
[42] T. Ogura, S. Hirosawa, T. Sato, Sci. Technol. Adv. Mater. 5 (2004) 491–496.

# Paper II

## The Effects of Low Cu Additions and Predeformation on the Precipitation in a 6060 Al-Mg-Si Alloys

Takeshi Saito, Shinji Muraishi, Calin D. Marioara, Sigmund J. Andersen, Jostein Røyset and Randi Holmestad

# The Effects of Low Cu Additions and Predeformation on the Precipitation in a 6060 Al-Mg-Si Alloy

TAKESHI SAITO, SHINJI MURAISHI, CALIN D. MARIOARA,
SIGMUND J. ANDERSEN, JOSTEIN RØYSET, and RANDI HOLMESTAD

Effects of low Cu additions (≤0.10 wt pct) and 10 pct predeformation before aging on precipitates' microstructures and types in a 6060 Al-Mg-Si alloy have been investigated using transmission electron microscopy (TEM). It was found that predeformation enhances precipitation kinetics and leads to formation of heterogeneous precipitate distributions along dislocation lines. These precipitates were often disordered. Cu additions caused finer microstructures, which resulted in the highest hardness of materials, in both the undeformed and the predeformed conditions. The introduced predeformation led to microstructure coarsening. This effect was less pronounced in the presence of Cu. The precipitate structure was studied in detail by high-resolution TEM and high angle annular dark-field scanning TEM (HAADF-STEM). The Cu additions did not alter the respective precipitation sequence in either the undeformed or the predeformed conditions, but caused a large fraction of $\beta''$ precipitates to be partially disordered in the undeformed conditions. Cu atomic columns were found in all the investigated precipitates, except for perfect $\beta''$. Although no unit cell was observed in the disordered precipitates, the presence of a periodicity having hexagonal symmetry along the precipitate length was inferred from the fast Fourier transforms (FFT) of HRTEM images, and sometimes directly observed in filtered HAADF-STEM images.

## I. INTRODUCTION

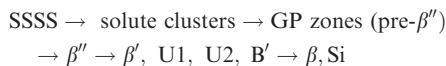THE 6xxx series (*i.e.*, Al-Mg-Si alloys) of wrought Al alloys are heat-treatable materials used in many industrial applications on the basis of their characteristic properties: high strength-to-weight ratio, good formability, and corrosion resistance. Their main property is a significant increase in hardness during a final isothermal heat treatment (artificial aging) at an adequate temperature and time. This is due to the formation of large numbers of nanosized semicoherent metastable precipitates which yield interfacial strain into the Al matrix, hindering dislocation movement. The interfacial strain originates from the different atomic matchings at the interface, which ultimately depends on the precipitate structure (type). Therefore, alloy properties depend highly on the precipitate types and the microstructures they produce (sizes, numbers, orientations, *etc.*). The precipitates are formed from solid solution and are controlled by the alloy composition and thermome-chanical history. The 6xxx alloys contain relatively low amounts of solute elements (up to 2 wt pct of Mg and Si), which become supersaturated in the fcc Al lattice after quenching from a solution heat treatment (SHT) to room temperature (RT). The solutes diffuse already at RT and nucleate atomic clusters. At elevated temperatures, during the artificial aging, the atomic clusters grow rapidly into metastable precipitates. Initially, fully coherent Guinier–Preston (GP) zones are formed with atoms on the Al matrix. The subsequent precipitates are seen to keep the alignment of some planes (fully coherent) only in one direction, corresponding to ⟨001⟩Al, except for the final, completely incoherent equilibrium phase $\beta$ (Mg$_2$Si), which forms at higher temperature. As a consequence, the metastable precipitates in this alloy system have needle/lath/rod morphologies extending along ⟨001⟩Al directions.

The precipitation sequence of Al-Mg-Si alloys is as follows[1–7]:

$$\text{SSSS} \rightarrow \text{ solute clusters} \rightarrow \text{GP zones (pre-}\beta'')$$
$$\rightarrow \beta'' \rightarrow \beta', \text{ U1, U2, B}' \rightarrow \beta, \text{Si}$$

where SSSS stands for supersaturated solid solution. The main hardening precipitates are the highly coherent, needle-shaped GP zones and $\beta''$ which form the finest microstructure. The U1, U2, and B' are larger, thicker needles/rods/laths and are also known as Type-A, Type-B, and Type-C, respectively.[8] They are mostly formed together with $\beta'$ (rod) upon over-aging. They are semicoherent and produce coarse microstructures with

TAKESHI SAITO, Ph.D. Candidate, and RANDI HOLMESTAD, Professor, are with the Department of Physics, Norwegian University of Science and Technology (NTNU), 7491 Trondheim, Norway. Contact e-mail: takeshi.saito@ntnu.no SHINJI MURAISHI, Assistant Professor, is with the Department of Metallurgy and Ceramics Science, Tokyo Institute of Technology, 2-12-1 Ookayama, Meguro-ku, Tokyo 152-8552, Japan. CALIN D. MARIOARA, Research Scientist, and SIGMUND J. ANDERSEN, Senior Scientist, are with the SINTEF Materials and Chemistry, 7465 Trondheim, Norway. JOSTEIN RØYSET, Principal Research Scientist, is with the Hydro Aluminum Research and Technology Development, 6601 Sunndalsøra, Norway.
Manuscript submitted October 11, 2012.
Article published online April 30, 2013

low strength. The equilibrium $\beta$ (Mg$_2$Si) phase can be plate- or cube shaped. It often coexists with pure Si particles with diamond structure, depending on the Si content of the alloy.

Additions of Cu (~0.40 wt pct) to the Al-Mg-Si alloys can drastically alter the precipitation sequence as follows[9–13]:
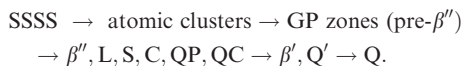
$$\text{SSSS} \rightarrow \text{atomic clusters} \rightarrow \text{GP zones (pre-}\beta'')$$
$$\rightarrow \beta'', \text{L, S, C, QP, QC} \rightarrow \beta', \text{Q}' \rightarrow \text{Q}.$$

This shows that the formation of $\beta''$ is suppressed, and other metastable precipitates such as L, S, C, QP, and QC are formed at peak hardness conditions.[9,11] Q$'$ is formed in over-aged conditions.[9,12] The Q$'$ is isostructural to the equilibrium Q phase.[13]

It was recently discovered that all metastable precipitates in the Al-Mg-Si(-Cu) system are structurally connected through a common network of Si atomic columns (the Si-network) with a projected near hexagonal symmetry of $a = b \approx 0.4$ nm, $c = n \times 0.405$ nm ($n$ is integer), with $c$ being parallel to the needle/rod/lath directions.[7,9] The network is also present in the equilibrium Q phase of the quaternary system. Basically, any of these precipitates can therefore be understood as stacks of elemental columns in a $\langle 001 \rangle$Al direction. They have just different arrangements of Al, Mg (and Cu) atomic columns situated in-between the triangularly arranged (0.4 nm spaced) columns forming the Si-network. When this *column* arrangement is periodic, the precipitates are characterized by a well-defined unit cell. However, although the Si-columns appear triangularly arranged and periodic in projection, it has been demonstrated that the overall arrangement *on the network* can be nonperiodic in many metastable precipitates of the Al-Mg-Si(-Cu) system, with partially disordered, or completely disordered precipitates, without a unit cell.[9] In this system, complex precipitate structures are encountered, consisting of ordered local parts that may be identified as Q$'$ and/or C together with more disordered parts, but all parts are connected by the same Si-network.[9,14] An exception from the above is the $\beta''$ phase, which has a distorted Si-network. The distortion is probably attributed to the full coherency with matrix. As a result, the column arrangement of the Si-network forms locally square symmetry approaching the Al unit cell although a triangular Si-network exists over part of the phase.

Most industrial products made of the 6xxx series are initially subjected to hot forming such as extrusion or rolling, and in many cases, also to cold forming into a final product. The forming process involves inherently a certain degree of plastic deformation of the materials. The artificial aging (*e.g.*, bake-hardening for automobile panel production) takes place at an adequate temperature generally after the forming process. In the presence of dislocations, the precipitation kinetics and sequence may change considerably since the dislocations provide heterogeneous nucleation sites for the precipitates. Previous reports show that predeformation before artificial aging enhanced nucleation rate and precipitation kinetics in a commercial AA6061 alloy.[15] Moreover, the precip-

itation sequence is altered due to predeformation in an AA6060 alloy.[16] Matsuda *et al.*[17,18] have reported that two different precipitate types nucleate along dislocation lines: a string-like phase, together with an elongated type which was mainly considered to be B$'$. Teichmann *et al.*[16,19] have demonstrated that all the precipitates nucleated on dislocation lines are based on the same Si-network as the bulk nucleated precipitates.

Recycling of Al alloys is a noteworthy activity in the Al industry. The need for recycling is supported by the fact that approximately 75 pct of Al ever produced since 1888 is still in use all over the world[20] and that the energy used for recycling Al is only about 5 pct of what is needed for its primary production.[20] While the main intention of the recycling activity remains important, the recycled Al inevitably contains certain levels of trace elements. The trace elements might induce undesirable changes in the precipitation behavior with consequences for the mechanical properties, since relatively low amounts of solute elements are needed to form precipitates.

Based on the above mentioned considerations, the influences of trace elements and predeformation on the precipitation are highly relevant topics of research in the context of the recycling activity. Considering several possible trace elements contained during the recycling processes, we focus in this study on the influence of low amounts of Cu (up to 0.10 wt pct), because of its considerable effect on the precipitation sequence when it is present in higher concentrations (~0.4 wt pct). The TEM observations and the hardness measurement were conducted in relation to predeformation (before artificial aging) on two Al-Mg-Si alloys, with emphasis on precipitate types and microstructures. The distribution of Cu atomic columns inside precipitates was also investigated in detail.

## II. EXPERIMENTAL PROCEDURES

Two alloys prepared by ultrapure Al with different amounts of Cu (0.01 and 0.10 wt pct), but with fixed levels of Mg and Si, were used. The alloys were cast as cylindrical ingots with 95 mm in diameter, from which extrusion billets were cut. The alloy compositions were measured by inductively coupled plasma optical emission spectroscopy and are shown in Table I. Although the two alloys contain Fe, the level (~0.07 wt pct) was chosen so as to be representative for the lowest practical Fe-level to be expected in industrial alloys.

The billets were homogenized at 848 K (575 °C) for 2.5 hours and subsequently extruded to a round profile with 20 mm in diameter. The extrusion was conducted using a direct press and a single hole die. The extrusion temperature was 773 K to 783 K (500 °C to 510 °C) which was well above the solvus temperature for the alloys, and the extruded profiles were water-quenched approximately 5 seconds after the die exit. Thus, only a rapid solid SHT was needed for the subsequent heat-treatment procedures. From these extruded profiles, some samples were machined with geometry shown in Figure 1 for the 10 pct predeformed condition, while

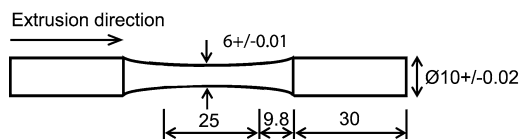| Alloy | Al | Mg | Si | Fe | Cu | Other |
|-------|-----|------|------|------|------|-------|
| 1 | bal. | 0.47 | 0.41 | 0.07 | 0.01 | 0.00 |
| 2 | bal. | 0.48 | 0.41 | 0.07 | 0.09 | 0.00 |
| Al-1 pct Mg | bal. | 0.97 | 0.05 | 0.07 | 0.00 | 0.00 |



Fig. 1—Sample geometry (unit: mm) of the predeformed samples. The predeformation was done by a 10 pct stretching along the extrusion direction.



Fig. 2—Thermomechanical histories for (a) the undeformed and (b) 10 pct predeformed conditions.

other samples were cut to 50-mm lengths for undeformed condition. They were solution heat treated in a salt bath at 818 K (545 °C) for 5 minutes, and subsequently water quenched. The samples were then exposed to RT (*i.e.*, natural aging) for a total of 30 minutes. The machined samples were plastically deformed to 10 pct by tensile stress within 5 minutes after the SHT (during the natural aging), while the other samples were left undeformed at RT. The 10 pct predeformation was conducted by a hydraulic MTS 810 test machine with a constant crosshead speed of 2 mm/min, corresponding to an initial strain rate of $1.3 \times 10^{-3}$ s$^{-1}$. The predeformed and the undeformed samples were further heat treated isothermally (*i.e.*, artificial aging) at 463 K (190 °C) for 10 minutes and 300 minutes in an oil bath. The thermomechanical histories for the undeformed and predeformed conditions are shown in Figure 2, which is identical to the one applied to a Cu-free commercial AA6060 alloy by Teichmann *et al.*[16,19] having similar amounts of Mg and Si as the alloys in this study.

Vickers hardness measurements were carried out along the deformation direction on transversal slices cut from the middle of the predeformed samples in which the deformation was expected to be homogenous. A Durascan-70 (Struers, Denmark) machine was used for the hardness measurement. The hardness indenter was used with a 5-kg load and the loading time being 15 seconds. Each data point corresponds to the average of ten hardness indentations, with the corresponding standard error.

In order to separate the hardness contributions of the solid solution, precipitates and the introduced dislocations in the case of predeformed conditions, a nonheat-treatable 5xxx series alloy, namely Al-1 wt pct Mg alloy, was used as a reference. This alloy has comparable solute amount to the investigated 6xxx alloys (see Table I), thus yielding a similar solid solution strength. The Al-1 pct Mg alloy was extruded with the same profile, was machined in the same manner (see Figure 1) and was subjected to the same thermomechanical treatment described above. Its hardness was measured in the same manner and for the same conditions as in the case of the two 6xxx alloys.
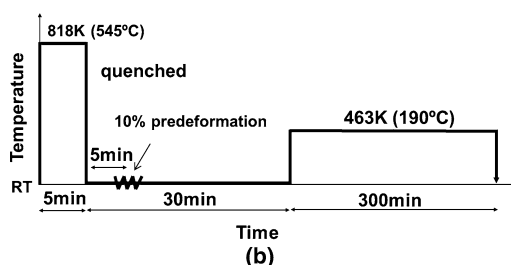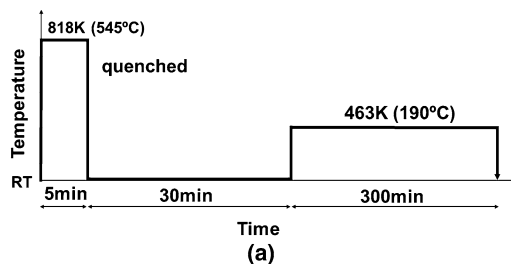
TEM specimens were prepared by electropolishing with a Tenupol 5 machine (Struers, Denmark), on the transversal slices used in the hardness measurements. The electrolyte consisted of 1/3 HNO$_3$ in methanol, and the solution was kept at a temperature between 253 K and 238 K ($-20$ °C and $-35$ °C).

Investigations of precipitate microstructure were performed by TEM in bright-field mode using a Philips CM30 operated at 150 kV with a double-tilt holder. A Gatan parallel electron energy loss spectroscopy (PEELS) (Gatan, UK) was used to measure the thickness of the specimens, *i.e.*, in the center of the area used in each image. All the TEM and PEELS analyses were performed along $\langle 001 \rangle$Al directions where approximately 1/3 of the needles can be viewed in cross section and 2/3 can be imaged perpendicular to the needle lengths. The combination of bright-field TEM images with corresponding thickness enabled average precipitate needle-lengths, cross sections, number densities and volume fractions to be quantified. The precipitate number density $\rho$ was defined as the total number of precipitates over the volume in the TEM images, calculated as follows: $\rho = 3N/At$ where "$N$" stands for the number of particles counted, "$A$" for the respective area on the TEM image, and "$t$" for the thickness (in the middle of the measured area) of the sample as measured by PEELS. The factor 3 in the formula arises because only needles viewed in the cross

section along one of the ⟨001⟩Al directions are counted. The volume in which the counted precipitates reside must be corrected (increased). This is because some fraction of needles having geometric centers outside (close to the specimen surface) has remaining parts inside the specimen that will be counted as particles, since they cannot removed during sample preparation. Hence, the number density can be expressed as $\rho = 3N/[A(t + \lambda)]$ instead of using the effective thickness $(t + \lambda)$ within which all precipitates with average needle length $(\lambda)$ originate. The precipitate volume fraction was calculated by multiplying the number density with the average needle length and the average cross section. Full description of the methodology has been given elsewhere.[4,21] The total number of precipitate lengths and cross sections measured were roughly 2000 and 700, respectively, for the statistical analysis in each thermo-mechanical condition.

A JEOL 2010F TEM/STEM operated at 200 kV and having 0.2 nm point resolution was used to determine precipitate types by HRTEM and HAADF-STEM imaging. The HAADF-STEM technique enables the determination of atomic column positions directly, being less affected by objective lens defocus and specimen thickness compared with HRTEM images. In addition, the technique provides atomic number $(Z)$ contrast with the intensity proportional to $Z^{1.7-1.9}$.[22,23] This enables to distinguish the heavier Cu ($Z_{Cu} = 29$) atomic columns from those of Mg ($Z_{Mg} = 12$), Al ($Z_{Al} = 13$) and Si ($Z_{Si} = 14$) in the precipitate structures. A probe size of 0.2 nm and an inner detector angle of ~28 mrad were used. The inner detector angle is smaller than what is normally used in the HAADF technique (>50 mrad). This was chosen for the purpose of achieving a sufficient signal-to-noise ratio, and based on previous study with similar materials.[9] All specimens were plasma cleaned before HAADF-STEM imaging to reduce the effect of contamination, using a Model 1020 Plasma Cleaner (Fischione Instruments, USA).

## III. RESULTS AND DISCUSSION

### A. *Hardness Results*

Figure 3 shows hardness values for the three alloys in undeformed and 10 pct predeformed conditions after the isothermal heat treatment at 463 K (190 °C) for 10 minutes and 300 minutes. The hardness measured right after SHT is also indicated (right after the predeformation in the case of predeformed conditions). In order to understand how Cu additions influence the hardness in connection with the predeformation, we attempt to quantify the hardness contributions of different factors. Four independent origins are assumed: Contribution from pure Al matrix ($HV_{pure}$), from solid solution ($HV_{ss}$), from dislocations ($HV_{dis}$) and from precipitates ($HV_{pre}$). Thus, the overall hardness may be described as a simple summation:

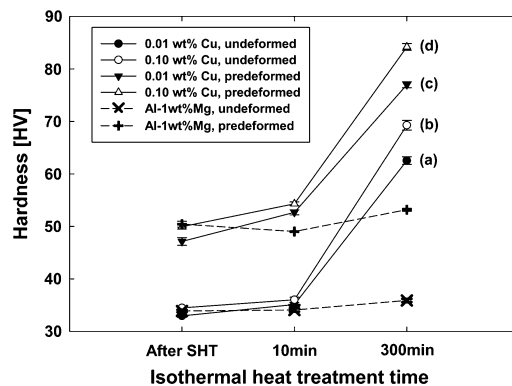$$HV = HV_{pure} + HV_{ss} + HV_{dis} + HV_{pre}$$



Fig. 3—Hardness evolutions for the two Cu-containing 6060 aluminum alloys and for an Al-1 wt pct Mg reference alloy in the undeformed and 10 pct predeformed conditions right after SHT and during an isothermal heat treatment for 10 min and 300 min at 463 K (190 °C). The hardness after SHT was measured right after the predeformation in the case of predeformed conditions. The alphabetic designations, corresponding to Figs. 3 and 5 and Table II, represent the alloys containing (a) 0.01 wt pct Cu in undeformed, (b) 0.10 wt pct Cu in undeformed, (c) 0.01 wt pct Cu in predeformed and (d) 0.10 wt pct Cu in predeformed conditions after the isothermal heat treatment for 300 min.

The hardness for pure undeformed Al (99.99 pct) is constant and has been measured at about ~15HV. The hardness curves for the Al-1 wt pct Mg alloy in the undeformed and predeformed conditions show only slight changes during the respective isothermal heat treatments. The hardness of this alloy is therefore assumed to be constant during the isothermal heat treatment both in the undeformed and predeformed conditions. For Al-1 wt pct Mg, the difference in hardness between undeformed and predeformed conditions gives $HV_{dis}$ ~20HV. The $HV_{ss}$ and $HV_{pre}$ are considered to be variable quantities during the isothermal heat treatment. Since precipitates originate from solid solution, $HV_{ss}$ decreases while $HV_{pre}$ increases during the isothermal heat treatment. A quantitative determination of $HV_{ss}$ and $HV_{pre}$ is not straight forward since the overall and relative fractions of the solute entering the precipitates depend on the precipitate type. Figure 4 shows an estimation of the relative hardness contribution from precipitates for the two investigated alloys in their undeformed and predeformed conditions, achieved by subtracting the respective hardness values of the Al-1 pct-Mg alloy.

The following are observations from Figures 3 and 4:

(a) The overall hardness of the predeformed alloys is always higher (with ~20HV) compared with the undeformed alloys. This is clearly due to the contribution of dislocations which were introduced by the 10 pct predeformation, *i.e.*, strain hardening.

(b) The hardness after SHT for the alloy containing 0.10 wt pct Cu is slightly higher (1–2HV) than that for the alloy containing 0.01 wt pct Cu in both the undeformed and predeformed conditions. This is
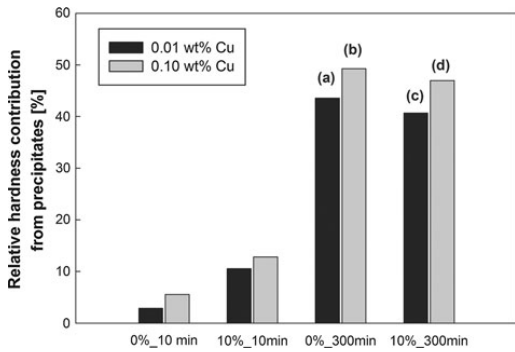
Fig. 4—Relative hardness contributions from precipitates for the two investigated alloys. Labels xx pct_XXmin in horizontal axis indicate that xx is the amount of predeformation, and XX is for isothermal heat-treatment time. For instance, alloy in predeformed condition after isothermal heat treatment for 300 min is represented as 10 pct_300min. The values were calculated by subtracting the respective hardness for Al-1 wt pct Mg alloy in each undeformed and predeformed condition. The alphabetic nomenclatures correspond to Figs. 3 and 6 and Table II.

interpreted as the effect of solute hardening from the extra Cu. The difference is somewhat larger in the case of predeformed conditions and might suggest slightly higher contribution from strain hardening in the alloy richer in solute.

(c) During the early stage of clustering/precipitation (up to 10 minutes of isothermal heat treatment), the hardness increases faster in the predeformed conditions than in the undeformed conditions, since the corresponding slope of the hardness curve in this region is slightly steeper. Furthermore, the relative hardness contribution from precipitates for the alloys in the predeformed conditions is higher than that in undeformed condition (see Figure 4). This indicates that the introduced dislocations enhance the precipitation, confirming previous study.[15]

(d) The overall hardness, as well as the relative hardness contribution from precipitates, of the alloy containing 0.10 wt pct Cu is higher than that of the alloy containing 0.01 wt pct Cu, in both undeformed and predeformed conditions. This is in good agreement with previous results showing that Cu additions enhance material hardness,[10,24] and demonstrates that 0.10 wt pct Cu addition is a quantity large enough to produce a measurable effect.

(e) During the precipitation up to 300 minutes of the isothermal heat treatment, the hardness increases at a slower rate in predeformed conditions than in the undeformed conditions. This suggests that the dislocations decrease $HV_{pre}$ in the later stage of isothermal heat treatment, which is opposite to the phenomena observed in the early stage (up to 10 minutes of isothermal heat treatment). One might expect that the peak hardness in predeformed conditions was different from that in the undeformed conditions, due to different precipitation kinetics.

(f) The respective differences in hardness after 10 minutes and 300 minutes of the isothermal heat treatment for the alloys containing 0.01 wt pct Cu and 0.10 wt pct Cu were similar in both the undeformed and predeformed conditions. This suggests that the predeformation did not enhance the effect of Cu, which means that the relative hardness contribution from precipitates is proportional to the Cu composition in the two alloys.

(g) The slight dip in the hardness curves at 10 minutes for the Al-1 wt pct Mg alloy in the predeformed condition might be due to dislocation annihilation. The subsequent recovery might be caused by subgrain formation. However, the effect is negligible compared with other changes, and its influence on hardness can be ignored for the two investigated alloys.

## B. Microstructure Investigations

### 1. Isothermal heat treatment for 10 minutes

Figure 3 shows that after 10 minutes of the isothermal heat treatment at 463 K (190 °C) the alloy containing 0.10 wt pct Cu has a slightly higher hardness than the alloy containing 0.01 wt pct Cu, in both the undeformed and the predeformed conditions. TEM investigations of the respective microstructures proved to be difficult due to the small precipitate size after this short isothermal heat-treatment time. However, it could be demonstrated that the alloys in undeformed and predeformed conditions produced different microstructures. Figure 5 shows typical bright-field TEM images for the alloy containing 0.10 wt pct Cu in the undeformed and predeformed conditions after the isothermal heat treatment for 10 minutes. A small fraction of precipitates was observed in the undeformed condition, as well as a small fraction of dislocations which probably had formed naturally during quenching after SHT. By contrast, the alloy in the predeformed condition shows a large amount of dislocations, on which needle- (and/or plate-) shaped precipitates, as well as string-like precipitates, have been nucleated. This proves that nucleation and growth of the precipitates have been considerable after 10 minutes of the isothermal heat treatment. This is in good agreement with the above given interpretation of the hardness, generally saying that predeformation enhances precipitation kinetics. Since the needles/plates were short and precipitate number density low, further quantifications of the conditions were not performed.

### 2. Isothermal heat treatment for 300 minutes

Figure 6 shows bright-field TEM images for the two alloys in undeformed and predeformed conditions after the isothermal heat treatment at 463 K (190 °C) for 300 minutes. The corresponding quantified microstructure parameters are summarized in Table II. Regardless of predeformation, the alloy containing 0.10 wt pct Cu was producing finer microstructures characterized by higher number densities of shorter needles and total higher volume fractions as compared with the alloy
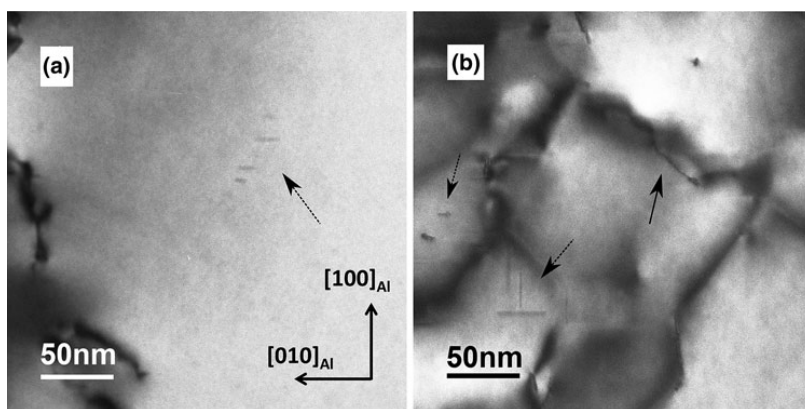
Fig. 5—Bright-field TEM images taken along ⟨001⟩Al directions for the alloy containing 0.10 wt pct Cu in (*a*) undeformed and (*b*) predeformed conditions, after an isothermal heat treatment at 463 K (190 °C) for 10 min. For a direct comparison, the images are recorded in areas with similar thicknesses (~110 nm). Crystallographic orientation for (b) is the same as that for (a). Some precipitate-types are indicated by arrows. Arrows with solid and dotted lines represent string-type and needle/lath-shaped precipitates, respectively. A large number of precipitates nucleated along dislocation lines can be observed in the predeformed condition.

containing 0.01 wt pct Cu. This supports the results of higher material hardness for the alloy with the higher Cu content (see Figure 3). Homogeneous distributions of precipitates were observed for both alloys in the undeformed condition, see Figures 6(a) and (b). In contrast, heterogeneous distributions associated with dislocation lines were found in the predeformed condition, see Figures 6(c) and (d). Predeformation was producing coarser microstructures characterized by lower number densities of longer, thicker needles in comparison with the undeformed conditions. This coarsening effect was reduced for the alloy containing the higher amount of Cu, as can be seen by comparing the quantified values for conditions (a), (c) with (b), (d) in Table II. The average precipitate's cross section in the undeformed condition was higher for the alloy with the high amount of Cu (0.10 wt pct), while the ones in the predeformed condition were similar for both alloys, see conditions (a), (b) as compared with (c), (d) in Table II. It implies that the precipitate types change as a function of Cu amount in the undeformed condition, while the precipitate types may be similar in the predeformed condition. A detailed discussion of the precipitate types is given in the next paragraph. It is also interesting to note that a combination of 0.10 wt pct Cu and 10 pct predeformation (condition (d)) produced the highest precipitate volume fraction observed among the investigated alloys.

### C. Precipitate Types

Based on HRTEM images, most precipitate types observed in the undeformed condition were perfect $\beta''$ for the alloy containing 0.01 wt pct Cu. By contrast, a large fraction of precipitates consisted of $\beta''$ and disordered atomic structures in the same needle, labeled $\beta''$/disordered from here on, were observed for the alloy

containing 0.10 wt pct Cu. These precipitates coexisted with a certain fraction of perfect $\beta''$. Figure 7 shows HRTEM images of a perfect $\beta''$ and a $\beta''$/disordered precipitates, viewed in cross section. Corresponding fast Fourier transforms (FFT) of the perfect $\beta''$ and of the disordered part of the $\beta''$/disordered precipitate are also shown. While the periodicity of the perfect $\beta''$ particle was clearly identified in the HRTEM image and corresponding FFT (see Figures 7(a) and (c)), the disordered part of the $\beta''$/disordered precipitate showed no clear periodicity in the HRTEM image (Figure 7(b)). However, a hexagonal periodicity of ~0.4 nm in real space could be identified in the FFT of the disordered part (Figure 7(d)), associated with the common Si-network.[7,9] Low amounts of fully disordered structures were also observed for both alloys in the undeformed condition. Teichmann[16] revealed that most precipitates forming in a commercial Cu-free AA6060 alloy after an isothermal heat treatment at 463 K (190 °C) for 300 minutes contain disorders of various degrees. However, we observed that most precipitates in the undeformed condition were perfect $\beta''$ for the alloy containing 0.01 wt pct Cu. This difference can be because the alloy used in Reference 16 contained 0.20 wt pct Fe, while in this study, the alloys contained only 0.07 wt pct Fe. A higher Fe content determines the formation of large primary phases and dispersoids which absorb a certain amount of Si, modifying both the amount of solutes available for the precipitation of hardening phases, and the Mg/Si ratio available for precipitates in the alloy. This might have rendered the composition in Reference 16 less ideal for the formation of the $\beta''$ phase.

As mentioned earlier, an addition of ~0.4 wt pct Cu alters the precipitation sequence in undeformed conditions of Al-Mg-Si alloys.[9–13] However, no precipitate types other than $\beta''$ and $\beta''$/disordered were observed in
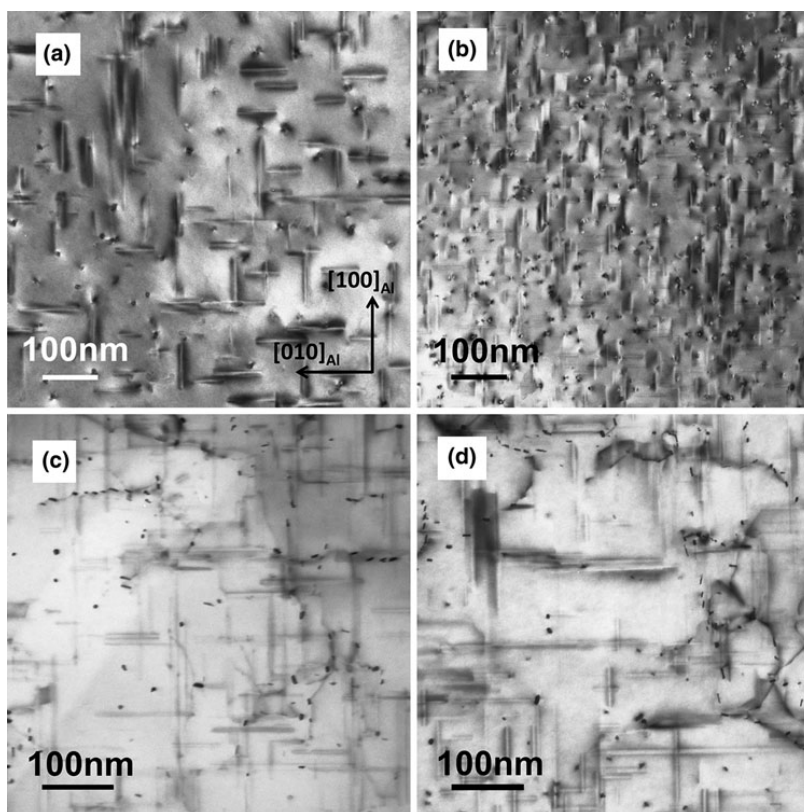
Fig. 6—Bright-field TEM images taken along ⟨001⟩Al directions for the alloys containing (*a*) 0.01 wt pct and (*b*) 0.10 wt pct Cu in undeformed conditions, and (*c*) 0.01 wt pct and (*d*) 0.10 wt pct Cu in 10 pct predeformed conditions, after an isothermal heat treatment at 463 K (190 °C) for 300 min, corresponding to Figs. 3 and 4 and Table II. For a direct comparison, the images are recorded in areas with similar thicknesses between 70 nm and 110 nm. Crystallographic orientation for (b) to (d) are the same as that for (a). The dark spots represent the cross sections of the needle-shaped precipitates in the viewing direction. The introduced dislocations in the predeformed conditions lead to coarser, inhomogeneous microstructures, while Cu addition produces a finer microstructure in the undeformed condition. See Table II for the microstructure quantification.

**Table II.  Precipitate Statistics for the Alloys Calculated from a Combination of Bright-Field TEM Images and Thicknesses Measured by PEELS According to the Methodology[4,21]**

|     | Needle Length (nm) | Number Density ($\mu m^{-3}$) | Cross Section (nm$^2$) | Volume Fraction (pct) |
| --- | --- | --- | --- | --- |
| (a) | 73.82 ± 2.09 | 5652 ± 628 | 6.29 ± 0.31 | 0.26 ± 0.01 |
| (b) | 50.00 ± 0.73 | 8254 ± 875 | 9.35 ± 0.46 | 0.39 ± 0.02 |
| (c) | 119.10 ± 3.08 | 2306 ± 252 | 10.61 ± 0.61 | 0.29 ± 0.02 |
| (d) | 77.29 ± 1.80 | 7271 ± 793 | 9.05 ± 0.37 | 0.51 ± 0.02 |

Alphabetic nomenclatures correspond to Figs. 3, 4 and 6.

the undeformed condition of the alloy containing 0.10 wt pct Cu. Furthermore, bright-field TEM images (see Figures 6(a) and (b)) indicate only contrast of needle type precipitates, and not that of C-plate-type precipitates. Therefore, it is suggested that the low amounts of Cu used in the present study (≤0.10 wt pct) do not affect the precipitation sequence, although it makes the $\beta''$ partially disordered and the microstructure finer.

The distribution of Cu atoms in these precipitates was investigated by HAADF-STEM. Figure 8 shows HAADF-STEM images from one perfect $\beta''$ and one $\beta''$/disordered precipitates in the alloy containing 0.10 wt pct Cu in the undeformed condition. The images show no distinctive bright Cu columns within the particle of the perfect $\beta''$ (see Figures 8(a) and (c)). In contrast, bright Cu columns appear in the $\beta''$/disordered precipitate (see Figures 8(b) and (d)). Furthermore, the
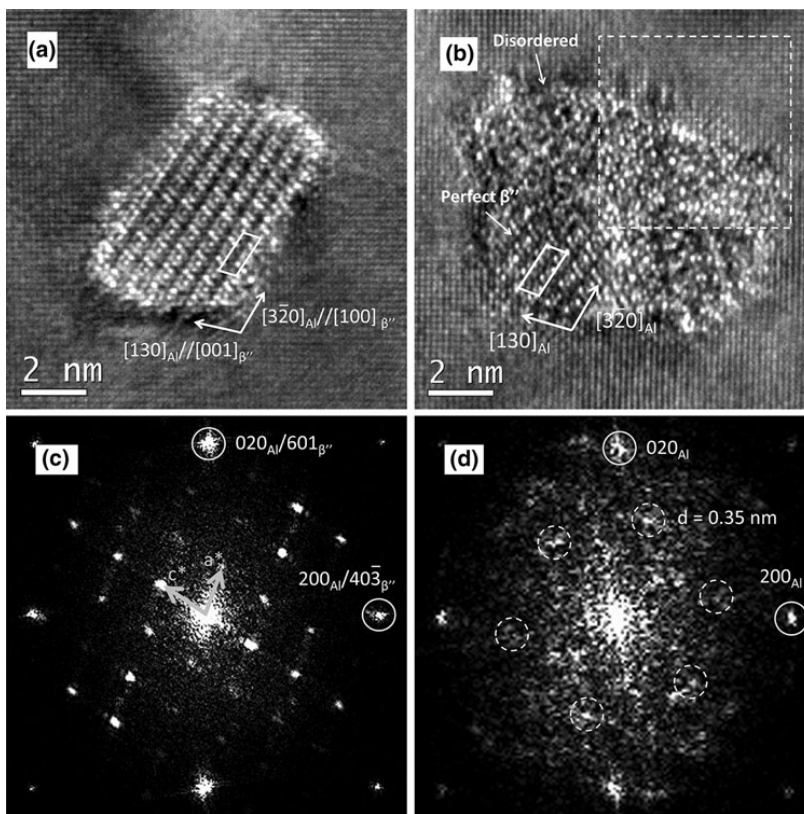
Fig. 7—HRTEM images of precipitate cross sections taken along $\langle 001 \rangle$Al for the alloy containing 0.10 wt pct Cu in the undeformed condition (b). (*a*) perfect $\beta''$, (*b*) a combined $\beta''$/disordered precipitate, (*c*) FFT of (a) and (*d*) FFT of disordered part of (b). A unit cell of the perfect $\beta''$ is shown by solid line in (a) and (b). The FFT of the disordered part was extracted from the area delimited by the dashed line square in (b). The d-spacing of 0.35 nm is the spatial period related to spots inside dashed circles in (d), and corresponds to a projected hexagonal periodicity of ~0.4 nm in real space, typical for the Si-network. It therefore indicates the presence of the network in the disordered part, where no unit cell could be identified in the HRTEM image (b).

Cu atomic columns are localized only within the disordered parts and at the interface of the $\beta''$/disordered precipitate, but not inside the perfect $\beta''$ part. These observations indicate that the perfect $\beta''$ structure does not accommodate Cu atoms. The periodicity of the hexagonal Si-network and the aperiodic presence of Cu columns on the Si-network can be observed in the disordered part (see Figure 8(d)). This result is supported by previous study,[14] where both aberration-corrected and uncorrected HAADF-STEM images of Cu-containing Al-Mg-Si precipitates demonstrated that, in addition to the Cu columns, Si atomic columns are also resolvable in the uncorrected images. The existence of the Si-network in the disordered parts confirms the observation from the HRTEM images (see Figures 7(b) and (d)).

In the predeformed conditions of the alloys, all the analyzed precipitates had partially disordered structure. In addition, most of the precipitates were nucleated along dislocation lines. No precipitate having the $\beta''$ structure was observed regardless of the amount of Cu. This is probably because the heterogeneous nucleation sites dominate, facilitating formation of post-$\beta''$ precipitates instead, with hexagonally arranged Si-columns.[16,19] String-type and disordered B′/Q′ needle/lath-shaped precipitates were observed along dislocation lines (see Figures 9(a) and (b), respectively). Many disordered precipitates showed the hexagonal B′/Q′ cell periodicity (1.04 nm) along a main side of the cross section, parallel with a $\langle 510 \rangle$Al direction (see Figure 9(b)). These precipitate types are similar to what has been reported by Matsuda[17,18] and Teichmann,[16,19] even though only Cu-free alloys were analyzed in those studies. Therefore, we conclude that 0.10 wt pct Cu additions in alloys in predeformed condition does not have a considerable effect on precipitate types, which is also supported by the results of the statistically similar size of cross section shown in Table II (see conditions (c) and (d)). HAADF-STEM images of typical precipitates from the alloy
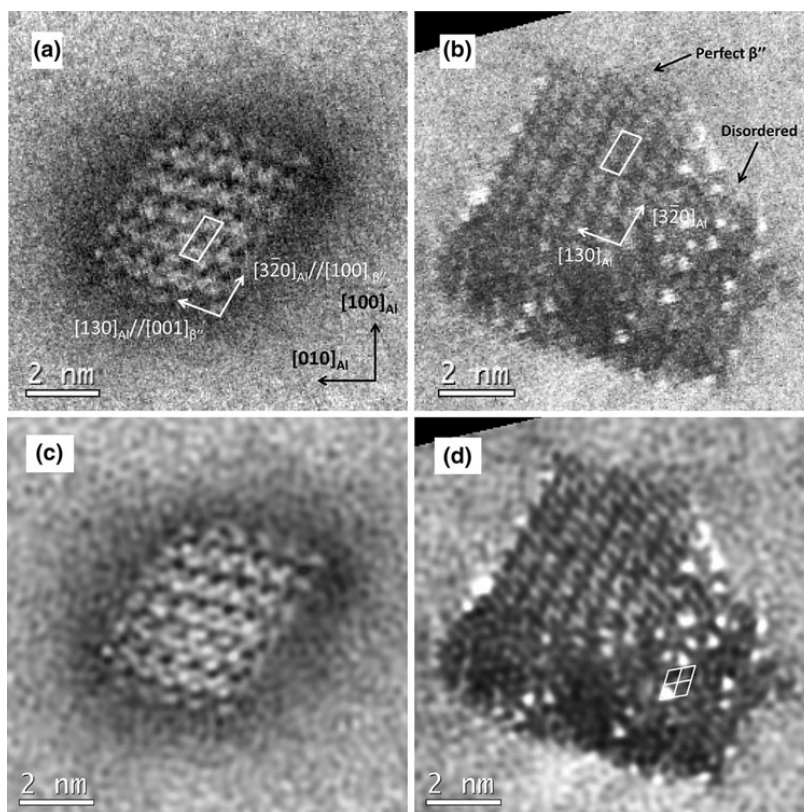
Fig. 8—HAADF-STEM images of precipitate cross sections taken along ⟨001⟩Al for the alloy containing 0.10 wt pct Cu in the undeformed condition. (a) Unprocessed image of a perfect β″, (b) unprocessed image of β″/disordered precipitate, (c) inverse FFT (IFFT)-filtered image of (a) and (d) IFFT-filtered image of (b). The IFFT filtering was applied to reduce noise using a circular band pass mask removing all periods shorter than 0.3 nm. A unit cell of the perfect β″ is shown by solid line in (a) and (b). Crystallographic orientation shown in (a) is common for all images. No specific atomic columns with high intensities are observed in the perfect β″ precipitate, or in the β″ part of the β″/disordered precipitate. However, strong contrasts corresponding to Cu-containing atomic columns are present in the disordered part of the β″/disordered precipitate, as well as at the precipitate–matrix interface. The periodicity of the hexagonal Si-network can be discerned in the disordered part, see the grid overlay in (d).

containing 0.10 wt pct Cu in the predeformed condition are shown in Figures 9(c) to (f). It can be observed that they are disordered (with no apparent unit cell) and that all of them contain Cu. This may indicate that Cu aids in producing a potent nucleation site, which would explain the strong increase in precipitate number density and volume fraction in condition (d) as compared with (c), see Figure 3 and Table II. However, as mentioned above, no change in precipitate types was observed in condition (d) as compared with studies using Cu-free alloys. The reason might be the low Cu amount (~0.10 wt pct) and the fact that B′ and Q′ precipitates are isostructural,[25,26] the latter associated with Cu-containing alloys.

Torsæter et al.[27] proposed a local atomic arrangement of Si and Mg columns surrounding each Cu atomic column common for the Cu-containing, C, Q, and Q′ (isostructural to Q) precipitates. Figure 10 shows the C and Q structures in detail, where the similarity of

the local arrangement of Si and Mg columns around Cu columns is clarified. It was shown that this local arrangement is also present around each Cu column in the disordered L phase[14] and is also found in precipitates of Al-Mg-Si-Ge-Cu alloy.[28] It is interesting to note that the local atomic arrangement of Si and Mg columns does not exist in the β″ structure (see Figure 10). Hence, it might be suggested that these Cu atoms preferentially accommodate this local arrangement of Mg and Si columns, with β″ precipitates having to become partially disordered to be able to host Cu atoms in undeformed condition. Careful analysis of the HAADF-STEM images (Figures 8 and 9) showed that the Cu is often accommodated between Si columns, as expected. However, in some instances, the Cu may systematically take positions on the Si column. This is clear from the higher magnification in Figure 11, where Si columns are joined by dashed, white lines revealing
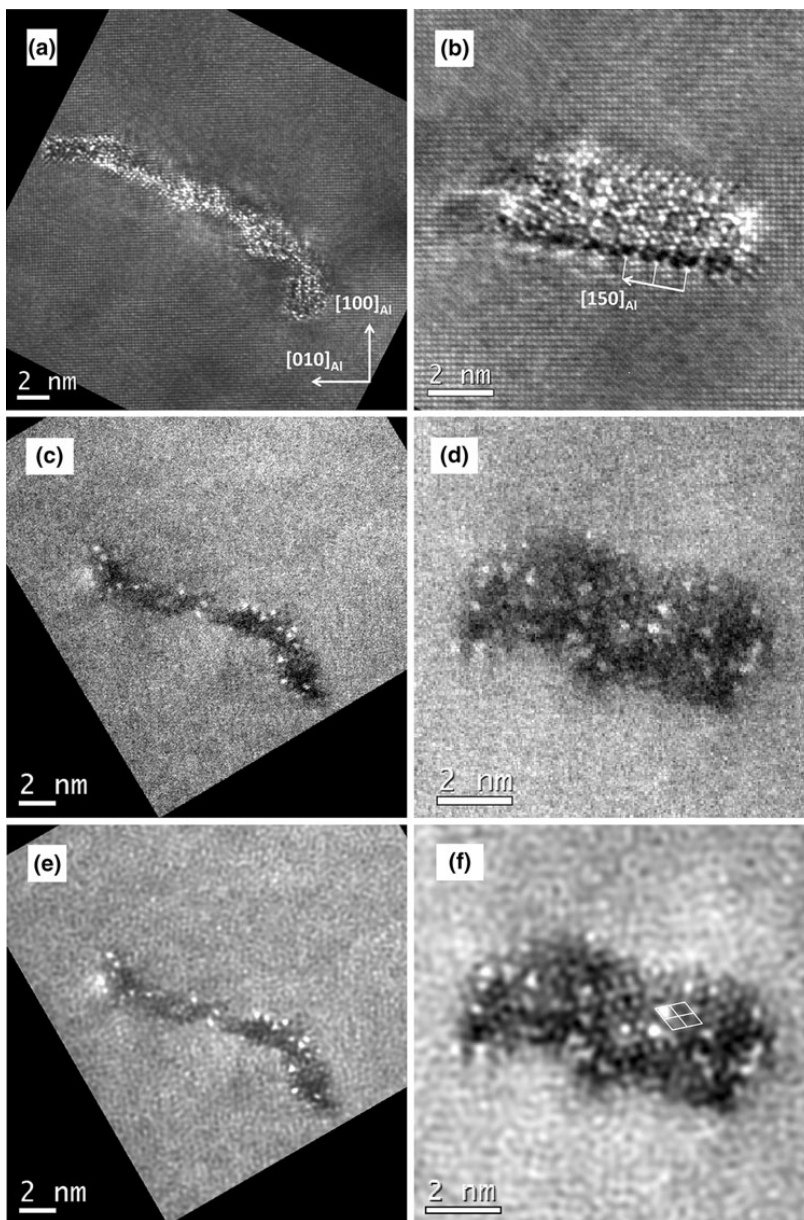
Fig. 9—HRTEM images of (*a*) string-type and (*b*) disordered B′/Q′ precipitates' cross sections taken along ⟨001⟩Al directions in the alloy containing 0.10 wt pct Cu in the predeformed condition. HAADF-STEM images of (*c*) string-type precipitates and (*d*) needle-type precipitate cross sections, (*e*) inverse FFT (IFFT)-filtered image of (c) and (*f*) inverse FFT (IFFT)-filtered image of (d). The IFFT filtering was processed to reduce noise using a circular band pass mask filtering out all periods shorter than 0.3 nm. Crystallographic orientation for (b) to (d) are the same as that for (a). Cu (brightest atomic columns) is present in both precipitate types, which are disordered (with no unit cell observed). However, the periodicity associated with the hexagonal Si-network can be identified, see the grid overlay in (d).

the Si-network, and some Cu columns are indicated by the circles. The Cu-free B′ structure shows also this local arrangement of Si and Mg columns,[25] supporting the argument that the low Cu amount (~0.10 wt pct) does not change in precipitate types in the predeformed condition.
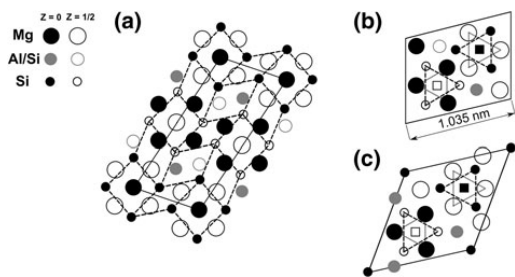
Fig. 10—Schematic images for unit cells for (a) β″,[2,3] (b) C phase,[27] and (c) Q phase precipitates,[13] drawn with the same scale. The common local arrangement around Cu atomic columns is indicated by dotted triangles on (b) and (c), which is identified for C, Q, Q′, and L phases.[14,27] This arrangement does not exist in the β″ structure, see (a). In (a), the Si atomic columns are connected by dashed lines.



Fig. 11—Higher magnification of the central (disordered) region of Fig. 9(f). The hexagonal overlay indicates the Si-network 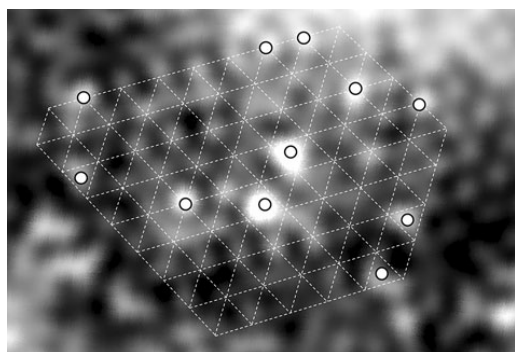columns at vertices. The distance between two vertices is about 0.4 nm. The strongest contrasts are Cu columns, indicated by the circles. They fall both between Si columns with an overall triangular appearance, but also on the Si vertices, where they obtain a more roundish appearance).

## IV. CONCLUSIONS

The effects of low Cu addition (0.01 and 0.10 wt pct) and predeformation (10 pct) on a 6060 Al-Mg-Si alloy were investigated as a function of an isothermal heat treatment at 463 K (190 °C) for 10 and 300 minutes. Changes in hardness, and the influence on precipitate numbers, size, cross section, and types were studied. The results obtained are summarized as follows:

1. Enhancement of precipitation kinetics in the presence of dislocations was observed during the early stage of clustering/precipitation, up to 10 minutes of isothermal heat treatment regardless of Cu content in the alloy.
2. Homogeneous precipitate distributions were observed in the undeformed condition, while heterogeneous distributions associated with the presence of dislocation lines dominated in the predeformed conditions. This shows that dislocations are the preferred nucleation sites for precipitation.

3. Finer microstructures giving materials of higher hardness were produced in the alloy with the highest Cu amount for both the undeformed and the predeformed conditions. In both alloys, the dislocations introduced by predeformation led to microstructure coarsening during the isothermal heat treatment. This effect was weaker in the alloy containing the higher amount of Cu.
4. A large fraction of precipitate consisting of β″ and disordered parts within the same needle was observed in the alloy containing 0.10 wt pct Cu in the undeformed condition. Mainly perfect β″ were observed in the alloy with 0.01 wt pct Cu. Thus, the low Cu additions did not change the precipitate type, but induced disorder in the β″ precipitates. However, no Cu atomic columns were observed within the structure of perfect β″ precipitates, or in the prefect β″ region of the β″/disordered precipitates. Instead, the Cu was localized in the disordered parts, which also contained the hexagonal Si-network.
5. String-type and needle/lath-shaped precipitates, many of them identified as B′/Q′ periodicities, nucleated along dislocation line in the predeformed condition. The same precipitate types were found in the Cu-free alloys. Therefore, it can be concluded that Cu additions up to ~0.10 wt pct do not cause other precipitate types to appear in the predeformed condition, although HAADF-STEM images showed that Cu was present in each of the investigated precipitates.
6. The combination of predeformation and the highest amount of Cu (0.10 wt pct) produced the highest precipitate volume fraction among the investigated alloys, while retaining a fine microstructure. This suggests that predeformation and Cu act independently in forming nucleation sites, which enhances microstructural evolution of precipitates and improves material strength.

## REFERENCES

1. G.A. Edwards, K. Stiller, G.L. Dunlop, and M.J. Couper: *Acta Mater*., 1998, vol. 46, pp. 3893–3904.
2. S.J. Andersen, H.W. Zandbergen, J. Jansen, C. Træholt, U. Tundal, and O. Reiso: *Acta Mater*., 1998, vol. 46, pp. 3283–98.

3. H.S. Hasting, A.G. Frøseth, S.J. Andersen, R. Vissers, J.C. Walmsley, C.D. Marioara, F. Danoix, W. Lefebvre, and R. Holmestad: *J. Appl. Phys.*, 2009, vol. 106, pp. 123527-1–123527-9.
4. C.D. Marioara, S.J. Andersen, H.W. Zandbergen, and R. Holmestad: *Metall. Mater. Trans. A*, 2005, vol. 36A, pp. 691–702.
5. C.D. Marioara, H. Nordmark, S.J. Andersen, H.W. Zandbergen, and R. Holmestad: *J. Mater. Sci.*, 2006, vol. 41, pp. 471–78.
6. R. Vissers, M.A. van Huis, J. Jansen, H.W. Zandbergen, C.D. Marioara, and S.J. Andersen: *Acta Mater.*, 2007, vol. 55, pp. 3815–23.
7. S.J. Andersen, C.D. Marioara, R. Vissers, A. Frøseth, and H.W. Zandbergen: *Mater. Sci. Eng. A*, 2007, vol. 444, pp. 157–69.
8. K. Matsuda, Y. Sakaguchi, Y. Miyata, Y. Uetani, T. Sato, A. Kamio, and S. Ikeno: *J. Mater. Sci.*, 2000, vol. 35, pp. 179–89.
9. C.D. Marioara, S.J. Andersen, T.N. Stene, H. Hasting, J. Walmsley, A.T.J. Van Helvoort, and R. Holmestad: *Philos. Mag.*, 2007, vol. 87, pp. 3385–413.
10. D.J. Chakrabarti and D.E. Laughlin: *Prog. Mater. Sci.*, 2004, vol. 49, pp. 389–410.
11. C. Cayron, L. Sagalowicz, O. Beffort, and P.A. Buffat: *Philos. Mag. A*, 1999, vol. 79, pp. 2833–51.
12. K. Matsuda, Y. Uetani, T. Sato, and S. Ikeno: *Metall. Mater. Trans. A*, 2001, vol. 32A, pp. 1293–99.
13. L. Arnberg and B. Aurivillius: *Acta Chem. Scand. A*, 1980, vol. 34, pp. 1–5.
14. C.D. Marioara, S.J. Andersen, C.B. Boothroyd, and R. Holmestad: *Proceedings of ICAA12*, 5–9 September 2010, Yokohama, Japan, ISBN 978-4-905829-11-9, pp. 424–29.
15. H.J. Rack: *Mater. Sci. Eng.*, 1977, vol. 29, pp. 179–88.
16. K. Teichmann, C.D. Marioara, S.J. Andersen, and K. Marthinsen: *Metall. Mater. Trans. A*, 2012, vol. 43A, pp. 4006–14.
17. K. Matsuda, H. Gamada, Y. Uetani, S. Rengakuji, F. Shinagawa, and S. Ikeno: *J. Jpn. Inst. Light Met.*, 1998, vol. 48, pp. 471–75.
18. K. Matsuda, S. Shimizu, H. Gamada, Y. Uetani, F. Shinagawa, and S. Ikeno: *J. Soc. Mater. Sci. Jpn.*, 1999, vol. 49, pp. 10–15.
19. K. Teichmann, C.D. Marioara, S.J. Andersen, K.O. Pedersen, S. Gulbrandsen-Dahl, M. Kolar, R. Holmestad, and K. Marthinsen: *Phil. Mag.*, 2011, vol. 91, pp. 3744–54.
20. J.A.S. Green: *Aluminum Recycling and Processing for Energy Conservation and Sustainability*, ASM International, Materials Park, OH, 2007, pp. 109–134.
21. S.J. Andersen: *Metall. Mater. Trans. A*, 1995, vol. 26A, pp. 1931–38.
22. P.D. Nellist and S.J. Pennycook: *Ultramicroscopy*, 1999, vol. 78, pp. 111–24.
23. T. Yamazaki, M. Kawasaki, K. Watanabe, I. Hashimoto, and M. Shiojiri: *Ultramicroscopy*, 2002, vol. 92, pp. 181–89.
24. W.F. Miao and D.E. Laughlin: *Metall. Mater. Trans. A*, 2000, vol. 31A, pp. 361–71.
25. R. Vissers, C.D. Marioara, S.J. Andersen, and R. Holmestad: *Proceedings of ICAA11*, 22–26 September 2008, Aachen, Germany, ISBN 978-3-527-32367-8, vol. 2, pp. 1263–69.
26. M. Torsæter, R. Vissers, C.D. Marioara, S.J. Andersen, and R. Holmestad: *Proceedings of ICAA11*, 22–26 September 2008, Aachenm, Germany, ISBN 978-3-527-32367-8, vol. 2, pp. 1338–44.
27. M. Torsæter, F.J.H. Ehlers, C.D. Marioara, S.J. Andersen, and R. Holmestad: *Philos. Mag.*, 2012, vol. 92, pp. 3833–56.
28. R. Bjørge, S.J. Andersen, C.D. Marioara, J. Etheridge, and R. Holmestad: *Philos. Mag.*, 2012, vol. 92, pp. 3983–93.

# Paper III

**Aberration-corrected HAADF-STEM investigations of precipitate structures in Al-Mg-Si alloys with low Cu additions**

Takeshi Saito, Calin D. Marioara, Sigmund J. Andersen, Williams Lefebvre and Randi Holmestad

Taylor & Francis
Taylor & Francis Group

# Aberration-corrected HAADF-STEM investigations of precipitate structures in Al–Mg–Si alloys with low Cu additions

Takeshi Saito[a]*, Calin D. Marioara[b], Sigmund J. Andersen[b], Williams Lefebvre[c] and Randi Holmestad[a]

[a]*Department of Physics, Norwegian University of Science and Technology (NTNU), N-7491, Trondheim, Norway;* [b]*SINTEF Materials and Chemistry, N-7465, Trondheim, Norway;* [c]*Université de Rouen, GPM, UMR CNRS 6634 BP 12, Avenue de I'Université, 76801, Saint Etienne du Rouvray, France*
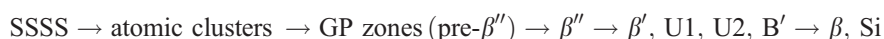
Precipitates in a lean Al–Mg–Si alloy with low Cu addition (~0.10 wt.%) were investigated by aberration-corrected high angle annular dark field scanning transmission electron microscopy (HAADF-STEM). Most precipitates were found to be disordered on the generally ordered network of Si atomic columns which is common for the metastable precipitate structures. Fragments of known metastable precipitates in the Al–Mg–Si–(Cu) alloy system are found in the disordered precipitates. It was revealed that the disordered precipitates arise as a consequence of coexistence of the Si-network. Cu atomic columns are observed to either *in-between the Si-network* or *replacing a Si-network column*. In both cases, Cu is the center in a three-fold rotational symmetry on the Si-network. Parts of unit cells of Q′ phase were observed in the ends of a string-type precipitates known to extend along dislocation lines. It is suggested that the string-types form by a growth as extension of the B′/Q′ precipitates initially nucleated along dislocation lines. Alternating Mg and Si columns form a well-ordered interface structure in the disordered Q′ precipitate. It is identical to the interface of the Q′ parts in the string-type precipitate.

**Keywords:** aberration correction; HAADF-STEM; age-hardening; aluminium alloy; precipitation

## 1. Introduction

Al–Mg–Si alloys are structural materials characterized by a high number density of precipitates yielding interfacial strain into the Al matrix and hindering dislocation movement. The efficiency of such obstruction depends highly on precipitate structure (type) because of different atomic bonding on the interface. The precipitates form with relatively low amounts of solute elements (up to 2 wt.% of Mg and Si), which become supersaturated in the fcc Al lattice after solution heat treatment and rapid cooling. During a subsequent artificial ageing, atomic clusters form and grow into metastable precipitates. The precipitation sequence of the Al–Mg–Si alloys is as follows [1–7]:

$$\text{SSSS} \rightarrow \text{atomic clusters} \rightarrow \text{GP zones}\,(\text{pre-}\beta'') \rightarrow \beta'' \rightarrow \beta',\,\text{U1, U2, B}' \rightarrow \beta,\,\text{Si}$$

---

*Corresponding author. Email: takeshi.saito@ntnu.no

where SSSS stands for super-saturated solid solution. In recent years, the structures of the various metastable precipitates have been investigated in great detail by transmission electron microscopy (TEM) based studies; the main hardening precipitates are the highly-coherent, needle-shaped GP zones and β″ which form the finest microstructure at peak hardness conditions [2]. The U1, U2 and B′ structures come in the shapes of larger, thicker needles/rods/laths and are also known as Type-A, Type-B and Type-C, respectively [8]. They mostly form together with β′ (rod) upon over-ageing [5]. They are semi-coherent and produce coarse microstructures with low strength. The equilibrium β (Mg$_2$Si) phase can be plate or cube-shaped. It often coexists with pure Si particles with diamond structure, for alloys with sufficiently high Si content.

The addition of Cu (~0.40 wt.%) alters the precipitation sequence as follows [9–13]:

$$\text{SSSS} \rightarrow \text{atomic clusters} \rightarrow \text{GP zones}\,(\text{pre-}\beta'') \rightarrow \beta'', \text{L, S, C, QP, QC} \rightarrow \beta', \text{Q}' \rightarrow \text{Q}.$$
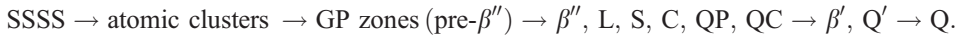
This shows that Cu suppresses the formation of β″, and causes other metastable precipitates such as L, S, C, QP and QC form at peak hardness conditions [9,11]. Q′ forms in over-aged conditions [9, 12]. This phase is most likely isostructural to the equilibrium Q phase [14] and to the B′ phase in the Cu-free system [15].

In the Al–Mg–Si–(Cu) alloy system, all metastable precipitates, as well as the equilibrium Q phase, are structurally connected through a common network of Si atomic columns (the Si-network) with a projected near hexagonal symmetry of a = b ≈ 0.4 nm, c = n × 0.405 nm (*n* is an integer), with *c* parallel to the needle/rod/lath directions [7,9]. These precipitates are basically a stack of elemental columns in a ⟨1 0 0⟩ Al direction adapting the Al periodicity and can be defined as different arrangements of Al, Mg (and Cu) atomic columns situated in-between the triangularly arranged (≈0.4 nm spaced) columns forming the Si-network. The Si-network is distorted in the case of the β″ phase as a consequence of the high coherency in this phase with the Al matrix.

In a previous work [16], we demonstrated that the addition of low amounts of Cu (~0.10 wt.%) to the Al–Mg–Si alloy system do not alter the precipitation sequence, although precipitation kinetics and number density of the precipitates change. In addition to perfect β″ precipitates, which are typically encountered at the peak hardness conditions of Al–Mg–Si alloys, large fraction of precipitates consisting of perfect β″ and disordered regions in the same precipitate needle (β″/disordered precipitates) was observed in the Cu-containing alloy. Using probe uncorrected high angle annular dark field scanning transmission electron microscopy (HAADF-STEM), no Cu could be detected in the perfect β″ parts while Cu atomic columns were observed within the disordered parts. Furthermore, it was found that the disordered parts are based on the above described Si-network. It was suggested that Cu atomic columns are associated with two specific local symmetries on the network (atomic configurations) by Mg, Si and Al atomic columns connected to the Si-network: Cu column either *in-between the Si-network columns* (being surrounded by Mg and Si atomic columns of the Si-network), or *replaces Si-network column*. While the exact atomic arrangement in the latter case could not be determined, it was suggested that the former local symmetry is similar to the one proposed earlier by Torsæter et al. [17]. This symmetry is not present in the bulk β″ precipitate, which might be related to its Cu-free composition [16].

Previous studies have reported that 10% pre-formation causes a heterogeneous precipitate distribution, with formation of different precipitate types in Al–Mg–Si alloy

system: string-like (the 'string-type') and roundish (B′/Q′ precipitates) cross-sections along dislocation lines [16,18–21]. A low Cu addition (~0.10 wt.%) preserved these types, although Cu atomic columns were observed in all investigated precipitates, as confirmed by probe uncorrected HAADF-STEM [16]. It was suggested that these precipitates contain the same specific local symmetries surrounding Cu atomic columns. However, the atomic structures in detail could not be determined due to the limited resolution of the HAADF-STEM instrument [16]. Hence, discussion of the atomic column symmetries and its connection to the Si-network were yet hypothetical.

In this work, we study the local atomic structure of these precipitates in details. Aberration-corrected HAADF-STEM, used for the results presented in this work, enables to determine Cu local symmetries, structure of the disordered parts of the precipitates and their interface structure with the Al matrix. The new knowledge can contribute to improve understanding of precipitation and growth mechanism and potentially to aid microstructure modelling in its efforts to connect micro-/nano-structure to macroscopic properties of the alloys. In recent years, recycling of Al alloys has become an important activity. Hence, these studies of low Cu addition (~0.10 wt.%) include also an aim to investigate effects of Cu *as a trace element* on precipitate structure [16].

## 2. Experimental procedure

An alloy with chemical composition of 0.47 Mg, 0.42 Si, 0.07 Fe and 0.10 Cu (wt.%) was used for all experiments. The composition was measured by inductively coupled plasma optical emission spectroscopy. Other impurities had a total less than 0.01 wt.%. The alloy was cast as a cylindrical ingot, from which the extrusion billet was cut. The billet was homogenized at 575 °C for 2.5 h and subsequently extruded to a round profile with 20 mm in diameter. The extrusion was conducted well above the solvus temperature for the alloy. From the extruded profiles, the alloys were machined with tensile test geometry for making a pre-deformed condition while others were cut transversally for an undeformed condition. All alloys were solution heat treated (SHT) in a salt bath at 545 °C for 5 min, and subsequently water quenched. They were then stored at room temperature (i.e. natural ageing) for a total of 30 min. The pre-deformed conditions were made by plastically deformed to 10% by tensile stress within 5 min after the SHT (during the natural ageing). All alloys were further heat treated isothermally (i.e. artificial ageing) at 190 °C for 300 min. The preparation and thermomechanical history are identical to the previous work, which are fully described in [16].

HAADF-STEM specimens were prepared by electropolishing using a Tenupol 5 machine (Struers), on transversal slices along the extrusion and deformation directions in the case of undeformed and pre-deformed conditions, respectively. The electrolyte consisted of 1/3 vol.% $HNO_3$ in methanol and the solution was kept at a temperature between −20 and −35 °C.

The HAADF-STEM images were taken by a spherical aberration probe corrected JEOL JEM-ARM200F TEM with a Schottky field emitter operated at 200 kV. The probe diameter was 0.1 nm and the collection angle of the HAADF detector was in the range of 45–150 mrad. The HAADF-STEM technique enables to determine atomic column positions directly, being less affected by objective lens defocus and specimen thickness compared to high resolution TEM images. In addition, the technique provides atomic number ($Z$) contrast with the intensity proportional to $Z^{1.7-1.9}$ [22,23].

This enables to distinguish the heavier Cu ($Z_{Cu}$ = 29) atomic columns from those of Mg ($Z_{Mg}$ = 12), Al ($Z_{Al}$ = 13) and Si ($Z_{Si}$ = 14) in the precipitate structures. In order to reduce contamination on the specimen during the HAADF-STEM observation, all specimens were ion-milled by precision ion polishing system (PIPS Gatan) and plasma cleaned by plasma cleaner (SOLARUS Gatan) before the observation.

## 3. Results and discussion

All HAADF-STEM images shown in this paper were taken from material isothermally heat treated at 190 °C for 300 min, which is known to produce a peak aged condition in this alloy [16]. Since the precipitate needles are growing in ⟨0 0 1⟩ Al directions, all images were taken from the ⟨0 0 1⟩ Al zone axis, corresponding to the cross sections of the precipitate needle. Owing to the high resolution of aberration-corrected HAADF-STEM, all atomic columns could be resolved in the structures. Based on their high Z contrast, Cu atomic columns could be identified even in the unprocessed HA-ADF-STEM images. Fast Fourier transform (FFT) filtering has been applied to reduce noise using a circular band pass mask that removed all period shorter than 0.15 nm. After filtering the images, weaker-contrast Si, Al and Mg atomic columns could also be resolved. The atomic overlays for all figures in this paper were based on the Z contrast, inter-atomic distances and local similarities with well-known structures in the Al–Mg–Si alloy system. The following sub-sections discuss each type of precipitates observed.

### 3.1. *β″/disordered precipitate*

Figure 1 shows a typical example of the β″/disordered precipitate. It is here straight forward to distinguish between the perfect β″ and the disordered parts in the precipitate. In this type of precipitate, the Cu atomic columns are found only within the disordered parts or at the precipitates/matrix interface but never inside the β″ structure. This observation supports results of the precious work [16]. It is interesting to note that the disordered part of the precipitate consists of several identical local atomic column arrangements, and it appears to have no overall unit cell periodicity. These arrangements can be identified to be sub-cell fragments in different types of the other metastable precipitates in the Al–Mg–Si(–Cu) alloy system, such as C, Q′, β′$_{Ag}$ and U2, see Figures 1 and 2. Figure 2 shows schematic drawing of unit cells of the encountered metastable precipitates. The legend in Figure 2 represents all figures in the present study. In the investigated precipitates, the disordered part is always based on the same ordered Si-network, see Figure 1. In addition, Cu atomic columns could be classified by their two different positions connected to Si-network: *in-between the Si-network columns* and *replacing Si-network columns*. The first case is identical to C, Q′, Q and L precipitates [17]. This is dominant with respect to the fraction of Cu columns found in such positions. The second case is interestingly analogue to Ag columns in β′$_{Ag}$ precipitates [24], but with Ag being replaced by Cu, see Figures 1 and 2. This local atomic configuration will be referred to as modified β′ in the present study, and represents a structure which is isostructural with the β′$_{Ag}$. It is worth noting that both cases have three-fold rotational symmetry around the Cu atomic columns in this projection, namely along needle growth direction. It seems plausible that Cu occupies only the sites that
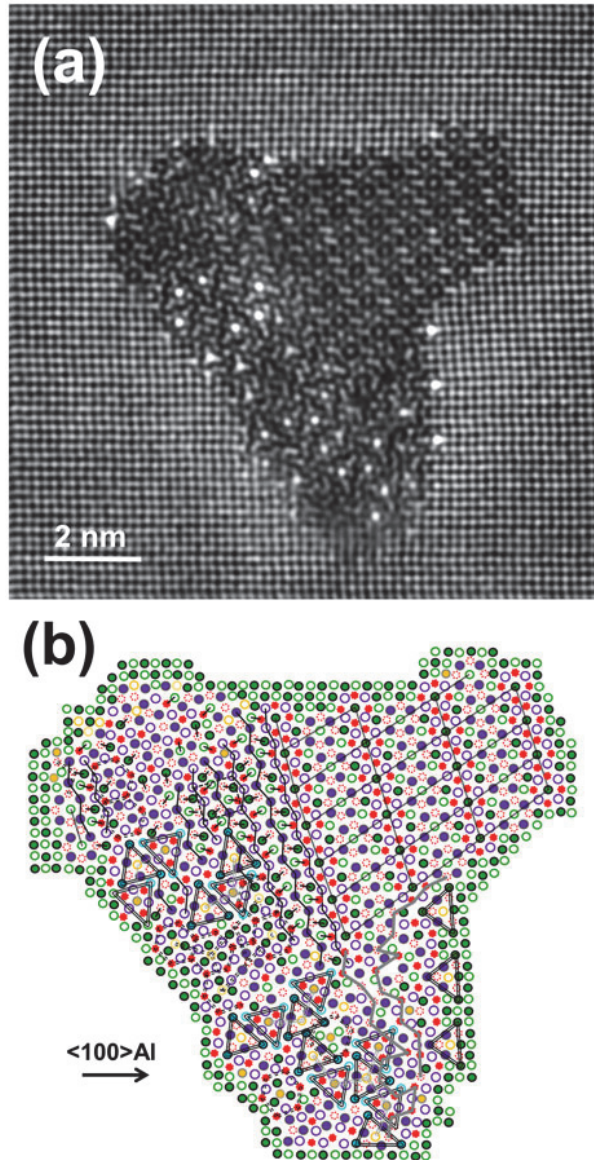
Figure 1. HAADF-STEM images of a β″/disordered precipitate cross-section taken along ⟨0 0 1⟩ Al for the undeformed condition. (a) Inverse FFT (IFFT) filtered image. (b) Suggested atomic overlay on the image (a). See legend in Figure 2.

can produce three-fold symmetry, or it modifies the surrounding columns to produce this type of symmetry. The β″ structure lacks this type of sites (atomic columns) because it is more closely adapted to the matrix, with a maximum two-fold symmetry, as given by its space group C2/m (12) [2,3]. Cu is therefore only able to exist at the disordered part and interface. It is worth mentioning that Al and Mg atomic columns

91
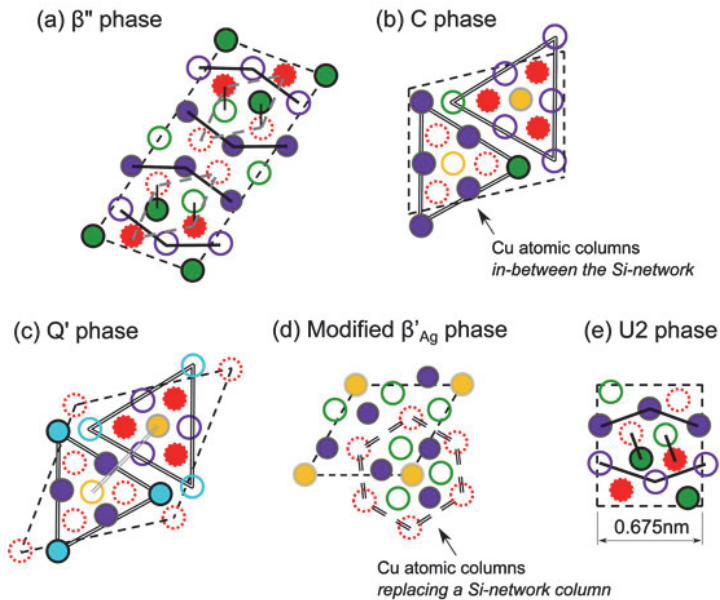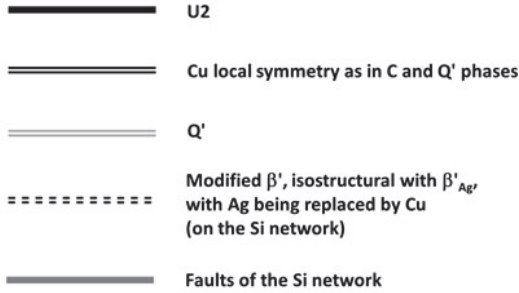
Figure 2. Legend representing all overlays in the present study and schematic drawings of unit cells of the encountered metastable precipitates: (a) β″ phase [2, 3], (b) C phase [17], (c) Q′ phase [14], (d) modified β′$_{Ag}$ phase [24] and (e) U2 phase [7], drawn to the same scale. The atomic column arrangement around Cu is shown for both *in-between the Si-network* and *replacing a Si-network column*. Cu atomic columns for the former case is identical to C, Q, Q′ and L phases [17] and the latter case is found in β′$_{Ag}$ phase [24] (Cu atomic columns instead of Ag in this case). Both Cu arrangements have three-fold rotational symmetry. Neither exists in the β″ phase probably because the space group of C2/m (12) at most allows two-fold rotation although parts of the near-hexagonal Si-network is found [2,3], see grey dashed line in (a). The β″ phase has fragments of U2 phase, which can create interface between perfect β″ and disordered parts along ⟨3 1 0⟩ Al direction in β″/disordered precipitate, see Figure 1.

also take positions in-between the Si-network columns; however, there is never a three-fold rotational symmetry around them.

In a previous work [16], it was measured that Cu-added alloy (~0.10 wt.% Cu) produces twice the precipitate number density than the base alloy (~0.01 wt.% Cu). It seems therefore that Cu atoms exert a strong effect on nucleation; either they create additional nuclei, or they merge with the ones already present, improving potently nucleation. Based on above mentioned observations, Cu atoms might produce clusters with atomic surrounding having three-fold symmetry connected to the Si-network during nucleation. This hypothesis will be discussed in later subsection.

As observed in Figures 1 and 2, some parts recognized to be associated with the U2 phase could frequently be observed in Cu-free areas of the disordered part of the β″/disordered precipitate. For instance, a long band consisting of the U2 structure acts as an interphase between bulk β″ and the disordered part. It is interesting to mention that β″ phase has fragment of U2 phase, see Figure 2(a). This could be a reason why the band consisting of the U2 structure acts as an interphase between bulk β″ and disordered parts in β″/disordered precipitate. Similar U2 bands connect domains of $β′_{Ag}$ in the precipitates of the respective system [24]. From Figure 1, it can be seen that the connection between the U2 band and the bulk β″ is much accurate compositionally if the Mg1 site in β″ phase is occupied by an Al atom. Therefore, a composition of $Mg_4Al_3Si_4$ is chosen for the β″ phase, which is one of the two lowest formation enthalpy structures according to previous study [3].

Cu atomic columns are also present to a certain extent at the precipitate/matrix interface, especially in the disordered part of the precipitate, see Figure 1. At the interface, Cu atomic columns are spread unevenly. Since the interface is rather incoherent, there will be sites that are more and less well suited for the Cu atoms. Another plausible explanation is that these columns formed in defect sites created due to the interface growth during nucleation/precipitation. Further experiments are needed to understand the possible role of Cu taking in shaping the interface. There was only one Cu-enriched column observed at the interface of the bulk β″ with the Al matrix, located on a Si3 site [3], see Figure 1. For the small area of the disordered part where the Si network is oriented along $\langle 0\,1\,0 \rangle$ Al (see the lower-right side of the precipitate in Figure 1), these three Cu atomic columns at the interface resemble local parts of C or L phase precipitates [17].

As mentioned, fragments of the C, Q′, $β′_{Ag}$ and U2 phases were identified in the disordered parts. The Si-network is near-hexagonal in all these phases, but has two orientations (rotations in the (0 0 1) Al plane), which sets the orientation of the precipitate cross-section and interface directions. For the C and L phases, one vector of the hexagonal base of the Si-network is oriented along $\langle 1\,0\,0 \rangle$ Al. For the other phases, it is along $\langle 5\,1\,0 \rangle$ Al. This creates a discontinuity (faults) in the Si-network at the interconnected region of these components, as seen in Figure 1.

## 3.2. String-type and disordered Q′ precipitates along dislocation lines

Examples of the string-type and disordered Q′ precipitates are shown in Figures 3 and 4. It is revealed that both precipitate types are also composed of fragments from a number of different metastable precipitates in the Al–Mg–Si(–Cu) alloy system. Both types of Cu local configurations, with Cu column *in-between the Si-network* and replacing *on the Si-network column*, were observed in the string-type precipitate, as it

was the case in the disordered part of the β″/disordered precipitates. Fragments of U2 phase are also easily identified. From these observations, we can conclude that all disordered precipitates are composed of parts of various metastable precipitates structure on a common near-hexagonal Si-network in some manner. It is interesting to note that half unit cells of Q′ precipitates were observed at the narrow ends of the cross-sections in the string-type precipitates see Figure 3. It is well known that Q′ and the string-type precipitates preferably form along dislocation lines [16,18–21]. This could indicate that Q′ precipitates (or fragments thereof) initially form along the dislocation line, and only later become connected by the string-type. For instance, for the precipitates in Figure 3, the half unit cell may represent the Q′ phase parts first nucleated. In other words, the string-type precipitates could start at different positions from small regions of Q′ building out the Si-network which should encounter somewhere in-between. This also means that they start not only at arbitrary heights, but also they meet in wrong directions. This will interrupt the ordering of the Si-network columns height, but could also lead to faults in the projected Si-network, both which will be sources of disorder. Note that the Si-network contains discontinuities in the non Q′ precipitates regions, see Figure 3. It is interesting to note that another fragment was observed as shown by thick solid red line in Figure 4(iii). The fragment is also connected with the ordering Si-network and is repeated like unit cell along $\langle 5\,1\,0 \rangle$ Al direction. However, this fragment has not reported yet as a pure precipitate phase. This could give interesting view to explain that Si-network might be much important than ordered precipitate structure during formation of precipitates, which will be discussed in next subsection.

Higher number density of precipitates was observed in the condition with the low Cu addition (~0.10 wt.%) compared to the base alloy (~0.01 wt.% Cu) in the pre-deformed condition [16]. This again supports the hypothesis for Cu atoms promoting nucleation in these materials.

It is worth noting that the precipitate interface structure of the Q′ part of the disordered precipitate in Figure 4 is well defined, which is shown by thick solid blue line on the upper side of the atomic overlay in Figure 4. Cu atoms are not incorporated in the interface structure, which instead consists of alternating Mg and Si atomic columns. This interface structure is found to be identical in the Q′ parts at the ends of the string-type precipitate, see Figure 3. The alternating Mg and Si atomic columns are also present at the interface of the lower side of the precipitates, although they are much in a disordered manner.

### 3.3. *Hypothesis of Cu local configurations in connection with Si-network during nucleation*

The disordered precipitates observed may provide new insight into the nucleation stage. The fragments which not continue to grow into bulk structures point out that the Si-network at some stage is more energetically favourable than the ordered precipitate structures. Note that the fragments of the other precipitates observed in the disordered precipitates were based on atomic columns along the whole needle-like precipitates. This means that the fragments grow side-by-side throughout the length of the precipitates. It is not possible to know the details during nucleation and in the early growth stage without dedicated experiment. However, it is plausible to say that the fragments based on Si-network would form during nucleation, in the early growth stage, before
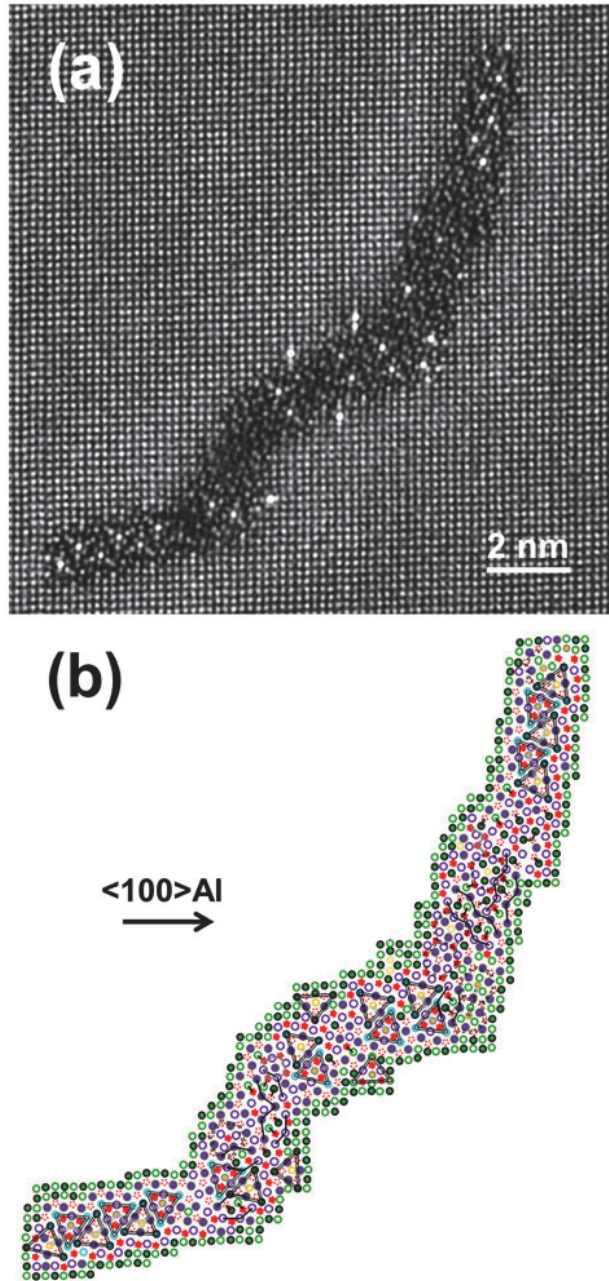
Figure 3. HAADF-STEM images of string-type precipitate cross-section taken along ⟨0 0 1⟩ Al for the 10% pre-deformed condition. (a) IFFT filtered image. (b) Suggested atomic overlay on the image (a). See legend in Figure 2. Half units cell of the Q′ phase are present at both ends of the precipitate.
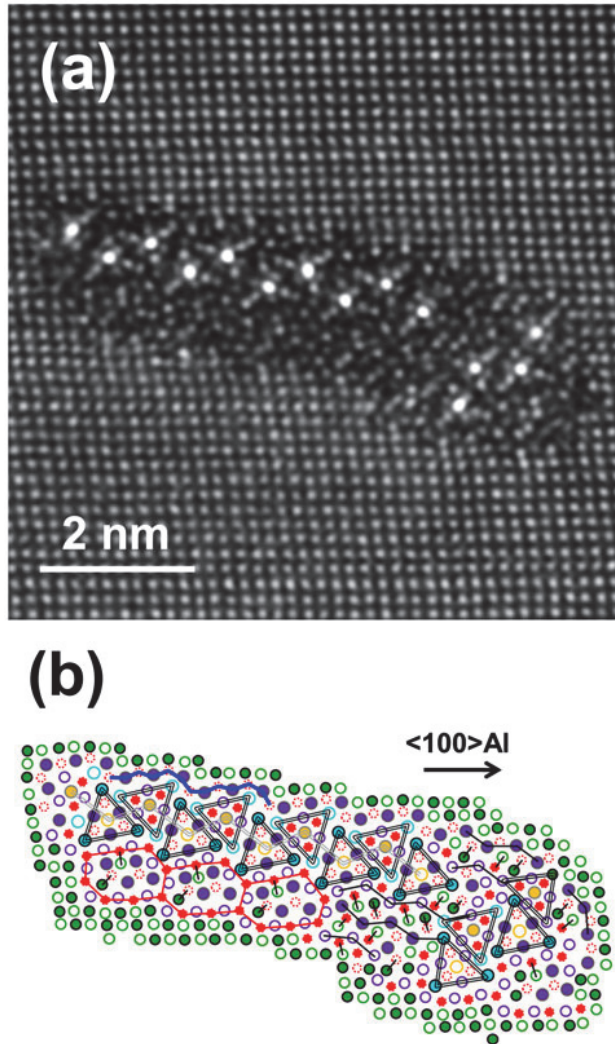
Figure 4. HAADF-STEM images of disordered Q′ precipitate cross-section taken along ⟨0 0 1⟩ Al for the 10% pre-deformed condition. (a) IFFT filtered image. (b) Suggested atomic overlay on the image (a). See legend in Figure 2. In addition, the alternating Mg and Si columns in the interface of the Q′ part with Al matrix along ⟨5 1 0⟩ Al is shown by thick solid blue line. Another fragment, which have not been reported yet as a pure precipitate phase in the Al–Mg–Si system are shown in thick solid red line.

growing as longer needles. During the early growth, several precipitate phases could be started off from the same 'local Si network'. Then, it allows more than one structure or fragment to be possible across the initial cross-section. It is understandable that the Cu aggregate could play an important role considering nucleation. Since Cu seeks to be surrounded by Si atoms, it would be influencing the local order on the Si-network at early stage and could make clusters more potent for the Cu-containing phases.

Here, one can wonder if the Cu atomic columns have full or partial occupancies of Cu atoms. Intensity and standard deviation measurements of Cu and Al matrix atomic columns in Figures 1, 3 and 4 may indicate a varying occupancy of Cu in the Cu columns. It is not straight forward to estimate the Cu distribution from these images, since the HAADF-STEM intensities vary with crystal structure and bonding, thickness of the specimen, where in the columns the Cu atoms eventually are, back ground intensity and the quality of the specimen. Future studies will hopefully clarify those aspects for further atomic modelling.

## 4. Conclusions

The precipitate structures formed in an alloy with composition 0.47 Mg, 0.42 Si, 0.07 Fe and a low addition of Cu (~0.10 wt.%) were investigated by aberration-corrected HAADF-STEM. It was found that a high fraction of the precipitates was disordered. The disordered precipitates were composed of local atomic column arrangements consistent with fragments of different types of metastable precipitates in the Al–Mg–Si–(Cu) alloy system, which exist side-by-side on a common near-hexagonal Si-network. Cu atomic columns were observed to be the centre in two types of columns arrangements depending on the Si-network. The Cu atomic columns take the place between three Si-network columns in the most frequent arrangement while Cu replaces a Si-network column in the less dominating arrangement. In both arrangements, the Cu has a three-fold rotational symmetry axis, as viewed along the needle growth direction. Half unit cells of Q′ phase were observed at the ends of a string-type precipitate. It is suggested that the string-type originates from initially nucleated Q′ precipitates/fragments which extend and meet each other along a dislocation line. A well-ordered interface structure consisting of alternating Mg and Si atomic columns was observed for the Q′ phase. This was identical to the interface of the Q′ precipices/fragments which extend and encounter each other along the dislocation line. The results of disordered precipitates indicate that the fragments are established early in the growth, possibly on small domains where the Si-network is established on just a few $(0\,0\,1)$ Al planes. Cu plays an important role for precipitate nucleation. It is suggested that Cu atoms influence the cluster during nucleation, priming them for Cu-containing phases, which explains the increased precipitate number densities in the Cu-containing alloys. It is likely that such clusters could contain the specific Cu arrangements as discussed.

## References

[1]  G.A. Edwards, K. Stiller, G.L. Dunlop and M.J. Couper, Acta Mater. 46 (1998) p.3893.
[2]  S.J. Andersen, H.W. Zandbergen, J. Jansen, C. Træholt, U. Tundal and O. Reiso, Acta Mater. 46 (1998) p.3283.

[3]  H.S. Hasting, A.G. Frøseth, S.J. Andersen, R. Vissers, J.C. Walmsley, C.D. Marioara, F. Danoix, W. Lefebvre and R. Holmestad, J. Appl. Phys. 106 (2009) p.123527.

[4]  C.D. Marioara, S.J. Andersen, H.W. Zandbergen and R. Holmestad, Metall. Mater. Trans. A 36 (2005) p.691.

[5]  C.D. Marioara, H. Nordmark, S.J. Andersen, H.W. Zandbergen and R. Holmestad, J. Mater. Sci. 41 (2006) p.471.

[6]  R. Vissers, M.A. van Huis, J. Jansen, H.W. Zandbergen, C.D. Marioara and S.J. Andersen, Acta Mater. 55 (2007) p.3815.

[7]  S.J. Andersen, C.D. Marioara, R. Vissers, A. Frøseth and H.W. Zandbergen, Mater. Sci. Eng. A 444 (2007) p.157.

[8]  K. Matsuda, Y. Sakaguchi, Y. Miyata, Y. Uetani, T. Sato, A. Kamio and S. Ikeno, J. Mater. Sci. 35 (2000) p.179.

[9]  C.D. Marioara, S.J. Andersen, T.N. Stene, H. Hasting, J. Walmsley, A.T.J. Van Helvoort and R. Holmestad, Philos. Mag. 87 (2007) p.3385.

[10] D.J. Chakrabarti and D.E. Laughlin, Prog. Mater. Sci. 49 (2004) p.389.

[11] C. Cayron, L. Sagalowicz, O. Beffort and P.A. Buffat, Philos. Mag. A 79 (1999) p.2833.

[12] K. Matsuda, Y. Uetani, T. Sato and S. Ikeno, Metall. Mater. Trans. A 32 (2001) p.1293.

[13] L. Arnberg and B. Aurivillius, Acta Chem. Scand. A 34 (1980) p.1.

[14] M. Torsæter, R. Vissers, C.D. Marioara, S.J. Andersen and R. Holmestad, *Proceedings of ICAA11*, 22–26 September 2008, Vol. 2, Aachenm Germany, ISBN 978-3-527-32367-8, 2008, p.1338.

[15] R. Vissers, C.D. Marioara, S.J. Andersen and R. Holmestad, *Proceedings of ICAA11*, 22-26 September 2008, Vol. 2, Aachenm Germany, ISBN 9978-3-527-32367-8, p.1263.

[16] T. Saito, S. Muraishi, C.D. Marioara, S.J. Andersen, J. Røyset and R. Holmestad, Metall. Mater. Trans. A. 44 (2013) p.4124.

[17] M. Torsæter, F.J.H. Ehlers, C.D. Marioara, S.J. Andersen and R. Holmestad, Philos. Mag. 92 (2012) p.3833.

[18] K. Matsuda, H. Gamada, Y. Uetani, S. Rengakuji, F. Shinagawa, and S. Ikeno, J.J.I.L.M 48 (1998) p.471.

[19] K. Matsuda, S. Shimizu, H. Gamada, Y. Uetani, F. Shinagawa and S. Ikeno, J. Soc. Mater. Sci. Jpn. 49 (1999) p.10.

[20] K. Teichmann, C.D. Marioara, S.J. Andersen, K.O. Pedersen, S. Gulbrandsen-Dahl, M. Kolar, R. Holmestad and K. Marthinsen, Philos. Mag. 91 (2011) p.3744.

[21] K. Teichmann, C.D. Marioara, S.J. Andersen and K. Marthinsen, Metall. Mater. Trans. A 43 (2012) p.4006.

[22] P.D. Nellist and S.J. Pennycook, Ultramicroscopy 78 (1999) p.111.

[23] T. Yamazaki, M. Kawasaki, K. Watanabe, I. Hashimoto and M. Shiojiri, Ultramicroscopy 92 (2002) p.181.

[24] C.D. Marioara, J. Nakamura, K. Matsuda, S.J. Andersen, R. Holmestad, T. Sato, T. Kawabata and S. Ikeno, Philos. Mag. 92 (2012) p.1149.

# Paper IV

## The effect of Zn on precipitation in Al-Mg-Si alloys

Takeshi Saito, Sigurd Wenner, Elisa Osmundsen, Calin D. Marioara, Sigmund J. Andersen, Jostein Røyset, Williams Lefebvre and Randi Holmestad

# The effect of Zn on precipitation in Al–Mg–Si alloys

Takeshi Saito[a]*, Sigurd Wenner[a], Elisa Osmundsen[a], Calin D. Marioara[b],
Sigmund J. Andersen[b], Jostein Røyset[c], Williams Lefebvre[d] and Randi Holmestad[a]

[a]*Department of Physics, Norwegian University of Science and Technology (NTNU), N-7491
Trondheim, Norway;* [b]*SINTEF Materials and Chemistry, N-7465 Trondheim, Norway;* [c]*Hydro
Aluminum Research and Technology Development, N-6601 Sunndalsøra, Norway;* [d]*Université de
Rouen, GPM, UMR CNRS 6634, BP 12, Avenue de I'Université, 76801 Saint Etienne du
Rouvray, France*

Effects of addition of Zn (up to 1 wt%) on microstructure, precipitate structure
and intergranular corrosion (IGC) in an Al–Mg–Si alloys were investigated.
During ageing at 185 °C, the alloys showed modest increases in hardness as
function of Zn content, corresponding to increased number densities of nee-
dle-shaped precipitates in the Al–Mg–Si alloy system. No precipitates of the
Al–Zn–Mg alloy system were found. Using high-angle annular dark-field
scanning transmission electron microscopy (HAADF-STEM), the Zn atoms
were incorporated in the precipitate structures at different atomic sites with
various atomic column occupancies. Zn atoms segregated along grain bound-
aries, forming continuous film. It correlates to high IGC susceptibility when
Zn concentration is ~1wt% and the materials in peak-aged condition.

**Keywords:** Al–Mg–Si alloy; precipitation; intergranular corrosion (IGC);
transmission electron microscopy (TEM); high-angle annular dark-field scan-
ning transmission electron microscopy (HAADF-STEM)

## 1. Introduction

### 1.1. *Al–Mg–Si alloys*

The 6xxx series aluminium alloys (i.e. Al–Mg–Si alloy system) constitute an important
heat-treatable alloy system. They are used in a wide range of industrial applications
since they have advantageous properties: high strength-weight ratio, good formability
and corrosion resistance. Their main feature is an increase in hardness during a final
isothermal heat treatment (i.e. artificial ageing) at an adequate temperature and time.
During the artificial ageing, a large number of various nano-sized semi-coherent meta-
stable precipitates will form. These precipitates set up surrounding strain fields which
prevent dislocation movement due to the interfacial strain into the aluminium matrix
(i.e. precipitation hardening). The interfacial strain depends on atomic matching at the
precipitate–matrix interface, which eventually makes the dislocations shearing and/or
looping on precipitates. The latter is known as Orowan mechanism occurring in certain
size and distribution of precipitates. Hence, the alloy properties depend ultimately on

---

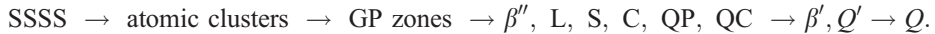*Corresponding author. Email: takeshi.saito@ntnu.no

the precipitate types and the microstructure they produce (sizes, numbers and orientations). The precipitation sequence comprises several metastable precipitates. The metastable precipitates form as a consequence of precipitation which is controlled by the alloy composition and thermo-mechanical history. The precipitation sequence of the Al–Mg–Si alloys is as follows: [1–8]:

$$\text{SSSS} \rightarrow \text{atomic clusters} \rightarrow \text{GP zones } (\text{pre} - \beta'') \rightarrow \beta'' \rightarrow \beta', \text{ U1, U2, B}' \rightarrow \beta, \text{ Si}$$

where SSSS stands for super-saturated solid solution. Solute elements become supersaturated in the fcc Al lattice after rapid cooling from a solution heat treatment to room temperature. The diffusion of the solute elements starts even at room temperature leading to nucleation of the atomic clusters. The atomic clusters grow rapidly into metastable precipitates during the artificial ageing. Fully coherent Guinier–Preston (GP) zones form initially with the solute elements occupying fcc positions in the Al matrix. The subsequent metastable precipitates are seen to keep the alignment of some planes (fully coherent) only in one direction, corresponding to $\langle 0\,0\,1 \rangle$ Al which is the main growth direction of the precipitates. As a consequence, they have needle/lath/rod morphologies extending along $\langle 0\,0\,1 \rangle$ Al directions. The main hardening precipitates are the highly coherent, needle-shaped GP zones and $\beta''$ phase which form the finest microstructures, characterized by large number densities of small (short and thin) needles. The U1, U2 and B′ (also known as Type-A, Type-B and Type-C, respectively, [9]) are larger, thicker needles/rods/laths. They mostly form together with $\beta'$ (rod) upon over-ageing. They are semi-coherent and produce coarse microstructures with low strength. The equilibrium $\beta$ ($Mg_2Si$) phase is incoherent and can be both plate- and cube-shaped. It forms and grows rapidly at higher temperatures. It often coexists with pure Si particles with diamond structure, depending on the Si content of alloy.

### 1.2. *Effects of additional alloying elements*

Effects of additional alloying elements in the Al–Mg–Si alloys are of key interest since they affect directly the microstructure and precipitate structure. For instance, Cu (~0.4 wt%) drastically alters the precipitation sequence as follows [10–14]:

$$\text{SSSS} \rightarrow \text{atomic clusters} \rightarrow \text{GP zones} \rightarrow \beta'', \text{ L, S, C, QP, QC} \rightarrow \beta', Q' \rightarrow Q.$$

The proportion of the $\beta''$ phase diminishes strongly for increased Cu content. The other metastable precipitates such as L, S, C, QP and QC form at peak-aged conditions [10, 11]. The $Q'$ phase forms in over-aged conditions [10,12]. $Q'$ is most likely isostructural to the equilibrium $Q$ phase [14].

An interesting feature of the Al–Mg–Si–(Cu) alloy system is that all metastable precipitates, as well as the equilibrium $Q$ phase, are structurally connected through a common network of Si atomic columns (Si-network) with a projected near hexagonal symmetry of $a = b \approx 0.4$ nm, $c = n \times 0.405$ nm ($n$ is integer), with $c$ parallel to the needle/rod/lath main growth directions [7,10]. Consequently, the precipitates consist of different arrangements of Al, Mg and Cu atomic columns located in-between the Si-network columns. Typically Cu promotes the formation of disordered precipitates, which lack a unit cell, although they are based on the Si-network. In the $\beta''$ phase, the Si-network is distorted, probably because of its high coherency with the Al matrix.

Ge is another additional alloying element influencing precipitation in the Al–Mg–Si (–Cu) alloys. It leads to the formation of Ge containing hardening phases which are iso-structural with the $\beta'$ and U1 phases in the Al–Mg–Si alloy system [15–17]. It was found that Ge forms a network similar to the Si-network. It is mixed (Si/Ge) when both elements are present in the alloy [17].

Addition of Ag (~0.5 wt%) in the Al–Mg–Si alloy system lead to an increase in hardness and elongation [18] by means of a new Ag-containing phase called $\beta'_{Ag}$ phase where Ag replaces one-third of the Si-network columns [19].

The amount of these additional alloying elements is an important factor influencing alloy properties and precipitation. It was previously demonstrated [20] that a low addition of Cu (~0.1 wt%) leads to a higher number density of precipitates, and conse-quently to higher strength, although the precipitation sequence is not altered. Furthermore, this level of Cu makes the $\beta''$ precipitates partially disordered in the same precipitate needle, which is also structurally connected to the Si-network [20]. A low additions of Ca (~0.1 wt.%) lowers, on the other hand, the precipitate number density, because of formation of large Ca-containing particles which absorb Si [21].

### 1.3. *Zn as an additional alloying element*

Zn is the main alloying element in the heat-treatable 7xxx series (Al–Zn–Mg) aluminium alloys. For instance, the commercial 7075 alloy typically contains 5.5 Zn, 2.5 Mg and 1.5 Cu (wt%). In this system, Zn atoms combine with Mg to form plate-like semi-coherent $\eta'$ metastable precipitates and equilibrium $\eta$-MgZn$_2$ precipitates on {1 1 1}Al planes [22–24]. These alloys have very low Si content. Our interest here is to investigate how modest additions of Zn influence Al–Mg–Si alloys. Concurrently, recycling of Al alloys is a noteworthy activity in the Al industry. Since Zn is one of the trace elements that can potentially end up in aluminium scrap metals during recycling, it is important to know to which extent different levels of Zn will influence the micro-structure, precipitate structure, mechanical and corrosion properties in Al–Mg–Si alloys. In the present paper, influence of Zn on the precipitation in Al–Mg–Si alloys has sys-tematically been investigated for different levels of Zn (up to 1 wt%).

### 2. Experimental procedure

Five alloys were prepared from ultrapure Al with different amounts of Zn (0.000, 0.001, 0.01, 0.1 and 1 wt %). The levels of Mg and Si were fixed. The alloys were cast as cylindrical ingots with 95 mm in diameter, from which extrusion billets were cut. The alloy compositions were measured by inductively coupled plasma optical emission spectroscopy and are shown in Table 1. Hereafter, the alloys with different amounts of Zn will be referred to as LZ0, LZ1, LZ2, LZ3 and LZ4 as shown in Table 1. All alloys contain ~0.07 wt% Fe, which is low for most industrial alloys. The billets were homogenized at 575 °C for 2.5 h and subsequently extruded into round profiles with 20 mm in diameter. The extrusions were conducted using a direct press and a single-hole die. The extrusion temperature was in the range of 500–510 °C, which is well above the solvus temperature for the alloys. The entire extruded profiles were water-quenched approximately 5 s after the die exit. Thus, only a short solid solution heat treatment was needed prior to subsequent heat treatment procedures. The extruded profiles were cut

Table 1. Measured alloy compositions (wt%) for the five alloys studied.

| Alloys/Elements | Al | Mg | Si | Fe | Zn | Other |
|---|---|---|---|---|---|---|
| LZ0 | Bal. | 0.47 | 0.40 | 0.07 | 0.000 | 0.000 |
| LZ1 | Bal. | 0.48 | 0.39 | 0.07 | 0.002 | 0.000 |
| LZ2 | Bal. | 0.47 | 0.40 | 0.07 | 0.012 | 0.000 |
| LZ3 | Bal. | 0.48 | 0.41 | 0.07 | 0.110 | 0.000 |
| LZ4 | Bal. | 0.47 | 0.39 | 0.07 | 1.019 | 0.000 |

into 500 mm lengths; solution heat-treated in an air-circulation oven at 540 °C for 1 h, and subsequently water-quenched. The alloys were then exposed to room temperature (i.e. natural ageing) for a total of 4 h. Furthermore, the alloys were aged at 185 °C in the air-circulation oven.

Vickers hardness measurements were carried out along the extrusion direction on transversally cut slices. A Durascan-70 (Struers) machine was used for the hardness measurements. The hardness indenter carried a 5 kg load. The loading time was 15 s. Each data point corresponds to the average of 10 hardness indentations, with the corresponding standard error. Electrical conductivity measurements were carried out at room temperature on the same surface as the hardness measurements. A SIGMATEST 2.069 operated at a frequency of 960 kHz was used. Each data point corresponds to the average of five conductivity measurements, with the corresponding standard error. Calibration of the equipment for the conductivity measurement was performed regularly in order to minimize error of the measurements. The hardness and conductivity were measured on the samples at 17 different ageing times up to 24 h.

TEM specimens were prepared by electropolishing with a Tenupol 5 machine (Struers), on the transversal slices used in the hardness measurements. The electrolyte consisted of 1/3 $HNO_3$ in methanol and the solution was kept at a temperature between −20 and −35 °C. Precipitate microstructure was investigated by TEM in bright-field mode using a Philips CM30 operated at 150 kV with a double-tilt holder. The thickness of the specimens was measured with a Gatan parallel electron energy loss spectrometer (PEELS). The thickness measurements were performed in the central area shown in the micrographs. The thickness in all images shown in this study was around 70–110 nm. All TEM and PEELS analyses were performed along $\langle 0\,0\,1 \rangle$ Al directions where approximately one-third of the needles can be viewed in cross-section and two-third perpendicular to the needle lengths. The combination of the TEM bright-field images and PEELS spectra enables average precipitate needle-lengths, cross-sections, number densities and volume fractions to be quantified. A full description of the methodology is given elsewhere [4,25]. Precipitate atomic structures were investigated by high-resolution high-angle annular dark-field scanning TEM (HAADF-STEM) using a spherical aberration (Cs) probe corrected JEOL ARM 200F STEM operated at 200 kV. The inner and outer collection angles of the HAADF detector were in the range of 45–150 mrad and the probe size was 0.1 nm. The HAADF-STEM technique enables to determine atomic column positions directly, being less affected by objective lens defocus and specimen thickness compared to high resolution TEM. In addition, the technique provides atomic number (Z) contrast with the intensity proportional to $Z^{1.7-1.9}$ [26,27]. This enables to distinguish the heavier Zn ($Z_{Zn} = 30$) atomic columns from those of Mg

$(Z_{Mg} = 12)$, Al $(Z_{Al} = 13)$ and Si $(Z_{Si} = 14)$ in the precipitate structures. In order to reduce contamination on the specimen during the HAADF-STEM observation, all specimens were ion-milled in a precision ion polishing system (PIPS Gatan) and further cleaned in plasma cleaner (SOLARUS, Gatan) before the observation. Fast Fourier transform (FFT) filtering has been applied to the HAADF-STEM images in order to reduce noise using a circular band pass mask which removes all periods shorter than 0.15 nm. A JEOL 2010F operated at 200 kV and equipped with an energy dispersive X-ray spectroscopy (EDS) from Oxford Instruments (with INCA software) was used for elemental mapping. For these acquisitions, drift compensation was activated, whereby the microscope regularly acquires annular dark-field scanning TEM (ADF-STEM) images and cross-correlates them to a reference image in order to adjust the STEM-EDS scanning position.

Accelerated corrosion tests were performed by following the British Standard (BS 11846 method B). The intergranular corrosion (IGC) susceptibility was evaluated after the corrosion test. The samples for the corrosion test were cut from the round extruded profiles parallel to the extrusion direction to a 'D-shape' (a shape of half cylinder) so that the metallography could be observed parallel with and perpendicular to the extrusion direction. Before the corrosion test, the samples were degreased using acetone and ethanol, followed by alkaline etching. The alkaline etching was conducted with immersion in a 7.5 wt% NaOH solution for 3 min at 55–60 °C, and then desmutting in concentrated $HNO_3$, which removed approximately 15 μm of sample surface. The corrosion test was conducted by immersion for 24 h in an acidified sodium chloride solution (30 g NaCl and 10 ml concentrated HCl per litre). After the immersion, the samples were washed in water and then in ethanol and subsequently dried. In order to investigate IGC susceptibility at different precipitation stages, samples with different heat treatment times were prepared corresponding to under-aged, peak-aged (T6) and over-aged (T7) conditions. Metallographic examinations after the corrosion test were conducted by optical microscopy.

## 3. Results and discussion

### 3.1. *Hardness and electrical conductivity*

Figure 1 shows hardness and conductivity curves for the five Zn-containing alloys as a function of ageing time, up to 24 h. The observations from the curves can be explained as follows:

- Both hardness and conductivity increase with increasing ageing time. This must be a result of precipitation; hardness increases as precipitates form, while conductivity increases since the Al matrix becomes depleted of solute atoms.
- The overall hardness of LZ4 is slightly higher than that of other alloys while the conductivity is lower. Lower conductivity may indicate the presence of Zn in solid solution throughout the ageing, while the slightly higher hardness could be due to the same effect (solution hardening), or in combination with a weak influence on precipitation. It is interesting to note that after 2 h of ageing time, corresponding to largest hardness difference between the alloys, hardness is nearly proportional with the Zn amount in the alloy. This indicates that Zn additions influence the formation of precipitates, although the effect seems to be weak.
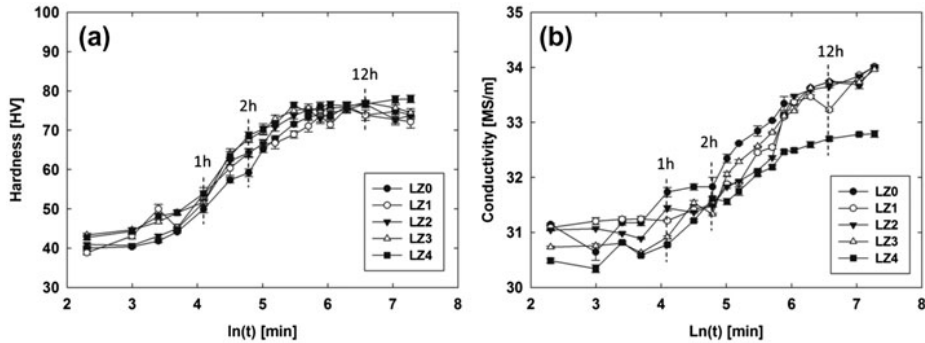
Figure 1. (a) Hardness and (b) electrical conductivity curves for the five Zn-containing alloys during an ageing at 185 °C. The designations and alloy compositions are shown in Table 1.

- Interestingly the conductivity curves for LZ0–LZ3 can be seen to converge with increasing ageing time. This could suggest that a certain amount of Zn diffuses from the Al matrix and enters into the precipitates. This phenomenon was not observed in LZ4, which may show that a saturation level of Zn in the precipitates has been reached.

### 3.2. *Microstructure*

Figure 2 shows bright-field TEM images for LZ1 and LZ4 after the ageing at 185 °C for 12 h, representing peak-aged condition. The corresponding quantified microstructure
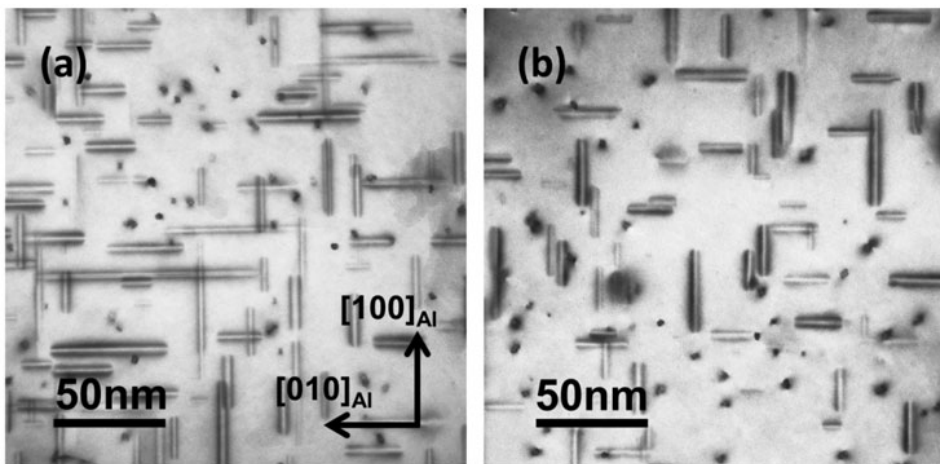


Figure 2. Bright-field TEM images taken along $\langle 0\,0\,1\rangle$ Al directions for (a) LZ1 and (b) LZ4 after an ageing at 185 °C for 12 h. For a direct comparison, the images are recorded in areas with similar thickness between 70 and 110 nm. Crystallographic orientation for (b) is the same as that for (a). Dark spots represent cross-sections of the needle-shaped precipitates along the viewing direction. See Table 2 for corresponding microstructure quantification.

Table 2. Precipitate statistics for the LZ1 and LZ4 alloys calculated from a combination of bright-field TEM images and thickness measured by PEELS according to the methodology [4,25].

| | Needle length [nm] | Number density [$\mu m^{-3}$] | Cross section [$nm^2$] | Volume fraction [%] |
|---|---|---|---|---|
| LZ1 | $55.43 \pm 0.74$ | $6397 \pm 663$ | $13.09 \pm 0.58$ | $0.46 \pm 0.02$ |
| LZ4 | $53.52 \pm 0.57$ | $7230 \pm 792$ | $12.54 \pm 0.57$ | $0.49 \pm 0.03$ |

parameters are summarized in Table 2. Only needle-like precipitates, typical for the Al–Mg–Si(–Cu) alloy system were observed along $\langle 0\,0\,1 \rangle$ Al directions. No plate-like precipitates were observed on {1 1 1}Al planes, as common for the Al–Zn–Mg alloy system. This indicates that $\eta'$ or $\eta$ phases were not formed in the investigated alloys. It should be noted that the normal ageing temperatures in Al–Zn–Mg alloy system are lower (~120 °C). It is therefore not impossible that these plate-like precipitates may form at the current ageing temperature for the Al–Mg–Si alloys. Mg prefers to combine with Si to form needle-like precipitates rather than with Zn for the composition and heat treatment given in this study. Homogeneous distributions of precipitates were observed for both alloys. The main difference between LZ1 and LZ4 is a slightly higher precipitate number density in LZ4, which correlates with a somewhat smaller precipitate average length and cross-section, resulting in the volume fraction. These results confirm, in the observations of hardness and conductivity, that Zn has a weak influence on precipitation, and consequently it should be expected that Zn is incorporated into the precipitate structure. This will be discussed in detail in a later sub-section.

Figure 3 shows an ADF-STEM image and corresponding to EDS elemental maps for relevant elements along a grain boundary and adjacent grains for the LZ4 after
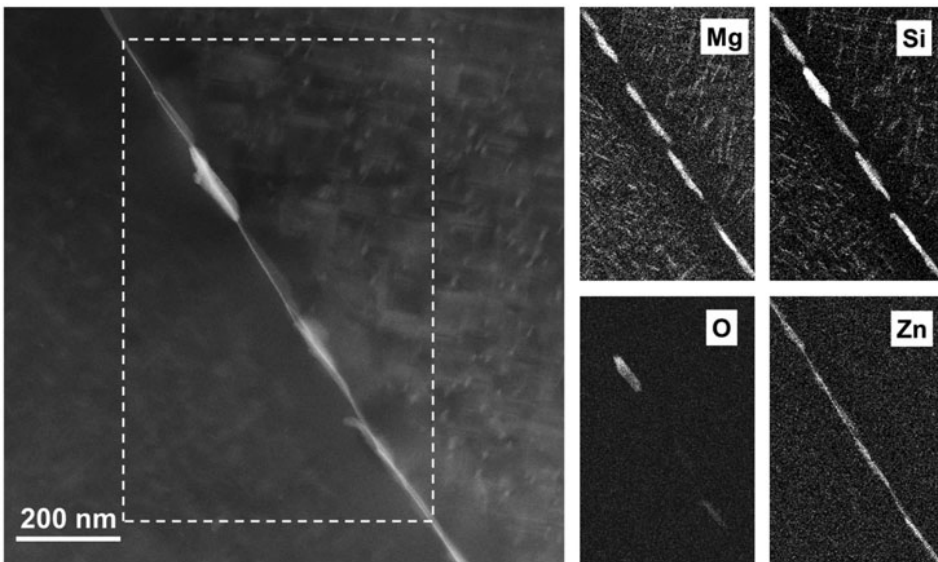


Figure 3. ADF-STEM image (left) for LZ4 after the ageing at 185 °C for 12 h and corresponding to EDS elemental maps for relevant elements (right) in the analysed area delimited by the dashed line rectangle. Alphabetic notations represent Mg: Magnesium, Si: Silicon, O: Oxygen and Zn: Zinc.

the ageing at 185 °C for 12 h. The ADF-STEM contrast of precipitate needles can be observed in the Al matrix, which clearly corresponds to the Mg and Si elemental maps. A precipitate free zone can also be seen in the Mg and Si elemental maps in the vicinity of the grain boundary. It is interesting to mention that EDS elemental map for Zn shows a shape of a line indicating the presence of a Zn thin film along the whole grain boundary. This continuous film can also be recognized in contrast to the ADF-STEM image. Figure 3 shows no trace of any precipitates in the Zn elemental map in Al matrix, while distinct EDS signals of needle precipitates in the Mg and Si elemental maps. Quantitative analysis of EDS data indicates that the Zn concentration in the two grains adjacent to the grain boundary is similar to the Zn nominal alloy composition. This leads to the conclusion that Zn is homogeneously distributed in the Al matrix, which seems to be supported by the observed low-electrical conductivity of LZ4, see Figure 1(b). This supports that Zn can only exist in low amounts in the precipitate needles. If Zn enters the composition of precipitate needles, it must be at a low level, below the detectability limit of the EDS detector. The ADF-STEM contrast and elemental maps along the grain boundary in Figure 3 also indicate the formation of grain boundary precipitates, consisting of Mg and Si. Based on EDS quantitative measurements, the Mg/Si ratios for these precipitates was found to be 1.5–1.7, which seem to correspond to the $\beta'$ ($Mg_{1.8}Si$) phase [6]. The data does not exclude the possibility of low Zn amounts being incorporated into such grain boundary precipitates. One grain boundary precipitate shows signals of Si and O, see Figure 3. In Al–Mg–Si alloys, it is not unusual to find amorphous and/or oxidized remains. This is presumably attributed to damage during electropolishing in specimen preparation.

### 3.3. *IGC susceptibility*

As shown in the EDS elemental map, Zn segregates along grain boundaries at peak-aged condition, forming an apparent continuous film. Among several types of corrosion considered, IGC is of high interest since it is related to grain boundary precipitates and atomic segregation on grain boundaries. In general, IGC is the result of microgalvanic reactions at grain boundaries; the grain boundary precipitates and/or segregated atoms are either active or noble with respect to the Al matrix. Figure 4 shows cross-section examinations after the IGC test for LZ3 and LZ4. Similar cross-section for the alloys with lower Zn contents – LZ0, LZ1 and LZ2 – had strong resemblance with LZ3, thus showing negligible IGC susceptibility. This implies that levels of Zn below 0.1 wt% have little influence concerning IGC. On the contrary, the cross-section of LZ4 shows strong evidence of corrosion attacks, indicating that the IGC susceptibility is pronounced only for the highest Zn concentration (1 wt%). This indicates that the critical level of Zn to influence the IGC is somewhere between 0.1 and 1 wt%. It is interesting to note that the IGC susceptibility depends highly on heat treatment, being pronounced at peak-aged and over-aged conditions, as compared to an under-aged condition, see Figure 4. The results of the IGC susceptibility and the TEM investigations suggest that the observed difference in the IGC must somehow be related to the characteristics of the Zn thin film presenting along the grain boundaries for the high Zn content. This should be compared with a recent finding in Cu-containing Al–Mg–Si alloys. Here,
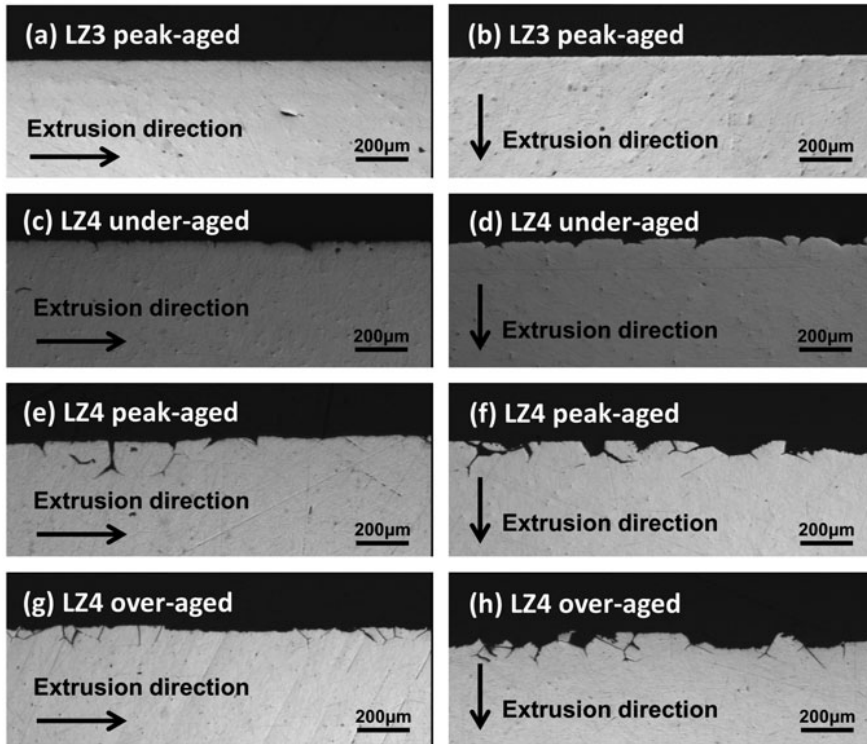
Figure 4. Cross-section optical micrographs after IGC test (a, b) for LZ3 for peak-aged (2 h), (c, d) for LZ4 for under-aged (2 h), (e, f) for LZ4 for peak-aged (12 h) and (g, h) for LZ4 for over-aged (30 h) conditions. The surface is either parallel (a, c, e, g) or perpendicular (b, d, f, h) to the extrusion direction. Cross-section for LZ0, LZ1 and LZ2 (not shown) is similar to that for LZ3.

IGC susceptibility was found to be reduced at peak-aged and over-aged conditions, when an analogous Cu-rich film along grain boundaries had become discontinuous during coarsening of grain boundary precipitates [28,29]. Note that the results in the present study may be interpreted oppositely, since the IGC susceptibility increases at peak-aged and over-aged conditions with the Zn film. Our investigation also shows that the IGC susceptibility is dependent on the extrusion direction; the corrosion attacks were pronounced along the extrusion direction, compared to perpendicular to it, see Figure 4. This might be attributed to different grain boundary orientation and/or a fibrous texture along the extrusion direction.

### 3.4. *Precipitate structures*

Based on the findings discussed in the previous sub-sections, it is still questionable whether or not Zn incorporates into the precipitate structure; the microstructure quantification (Table 2) shows that there is a correlation between an increased precipitate number density and a high Zn amount in the alloy composition, while the EDS maps (Figure 3) do not seem to show any Zn signal associated with the precipitates. In this

sub-section, precipitate structure will be discussed by observations from aberration corrected HAADF-STEM. All HAADF-STEM images shown in this sub-section were taken from LZ4 after ageing for 12 h (peak-aged). They were taken from the $\langle 0\,0\,1 \rangle$ Al zone axis, corresponding to the cross-sections of the precipitate needles. Owing to the high resolution of aberration-corrected HAADF-STEM, all atomic columns could be resolved in the structures. Based on the high Z contrast, a column having a sufficient fraction of Zn atom can easily be identified even in the unprocessed HAADF-STEM images. After filtering the images, weaker-contrast Si, Al and Mg atomic columns could also be resolved. The atomic overlays for all figures in this sub-section were based on the Z contrast, inter-atomic distances and local similarities with well-known structures in the Al–Mg–Si(–Cu) alloy system.

Most analysed precipitates had disordered structures lacking a unit cell, but it was found that they still were based on the Si-network. Figures 5–7 show examples of disordered precipitates while Figures 8 and 9 displays a $\beta''$ precipitate. A legend in Figure 10 explains the atomic overlays in Figures 5, 7, 8 and 9, as well as unit cells of phases in which fragments are frequently encountered in the structure of the disordered precipitates. In the HAADF-STEM images, bright spots represent atomic columns containing Zn. This is a strong indication of the Zn incorporation into precipitates. In the disordered precipitates, the intensity of the Zn-containing columns was found to vary, indicating fluctuating, partial Zn occupancy. It is worth noting that the disordered precipitates were still based on a regular Si-network. They are found to contain fragments of known precipitates in the Al–Mg–Si(–Cu) system. As a consequence of the disorder, the Zn distribution is non-periodic. Columns containing Zn were identified both in-between the columns of the Si-network, as well as replacing Si-network columns. In



Figure 5. HAADF-STEM images of disordered precipitate cross-section taken along $\langle 0\,0\,1 \rangle$ Al for LZ4 after ageing for 12 h. (a) FFT filtered image and (b) suggested atomic overlay. Local atomic configurations shown in the areas (i), (ii) and (iii) can be identified as the $\beta'_{Ag}$ phase [19], the C phase [30] and the U2 phase [8], respectively. See legend in Figure 10.

Figure 6. HAADF-STEM images of disordered precipitate cross-section taken along $\langle 0\,0\,1 \rangle$ Al for LZ4 after ageing for 12 h. (a) Unprocessed image, (b) FFT-filtered image of (a). White solid arrow shows Zn atoms segregated to the interface, but occupying Al fcc positions.

this respect, the Zn distribution resembles that of Cu [31] in similarly disordered precipitates. On the other hand, Zn seems to have less preference for particular local atomic sites. It can be observed that Zn has a weak preference for a number of sites: such as the Ag and Al sites in the $\beta'_{Ag}$ phase [19], the Cu sites in the C phase [30] and the Al
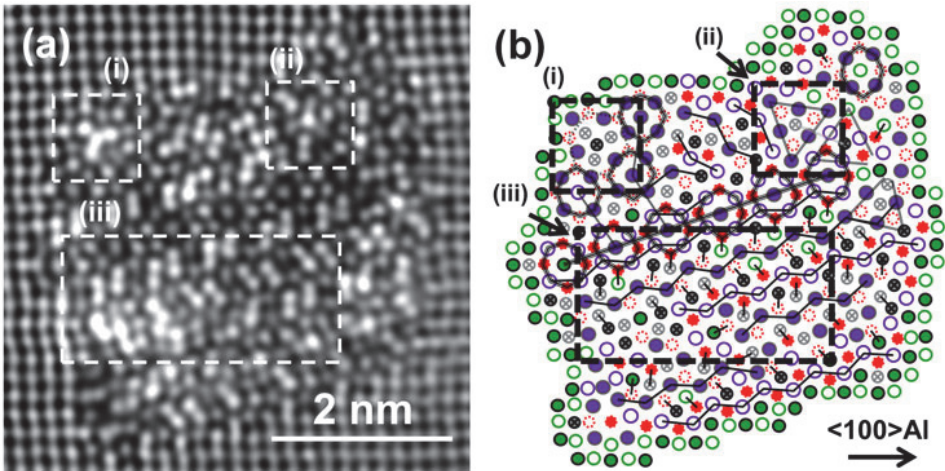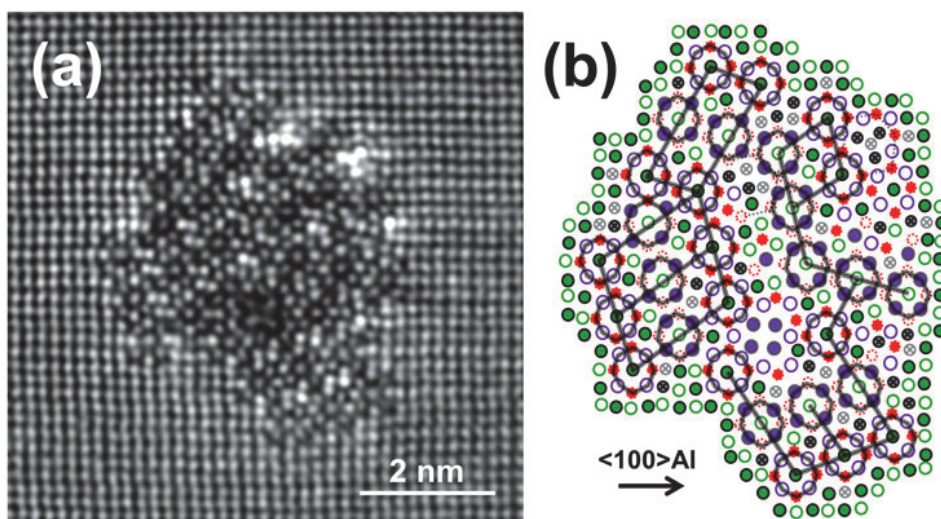


Figure 7. HAADF-STEM images of disordered precipitate cross-section taken along $\langle 0\,0\,1 \rangle$ Al for LZ4 after ageing for 12 h. (a) FFT filtered image and (b) suggested atomic overlay on the image (a). See legend in Figure 10.
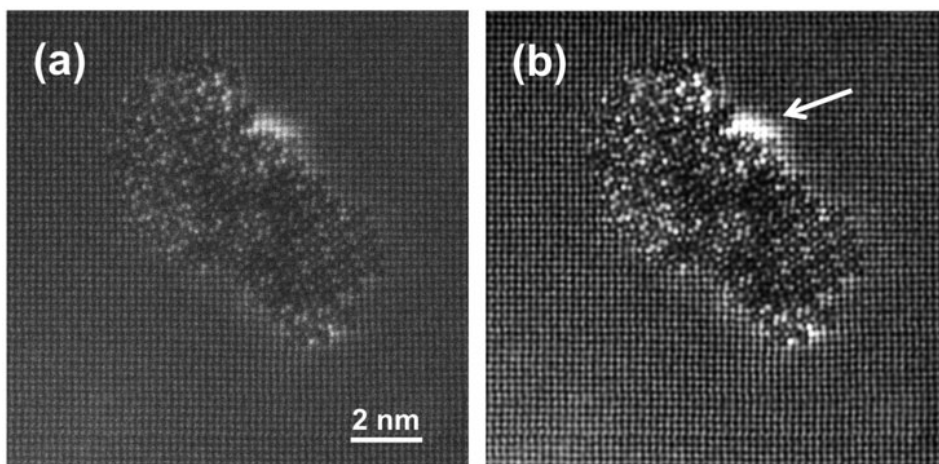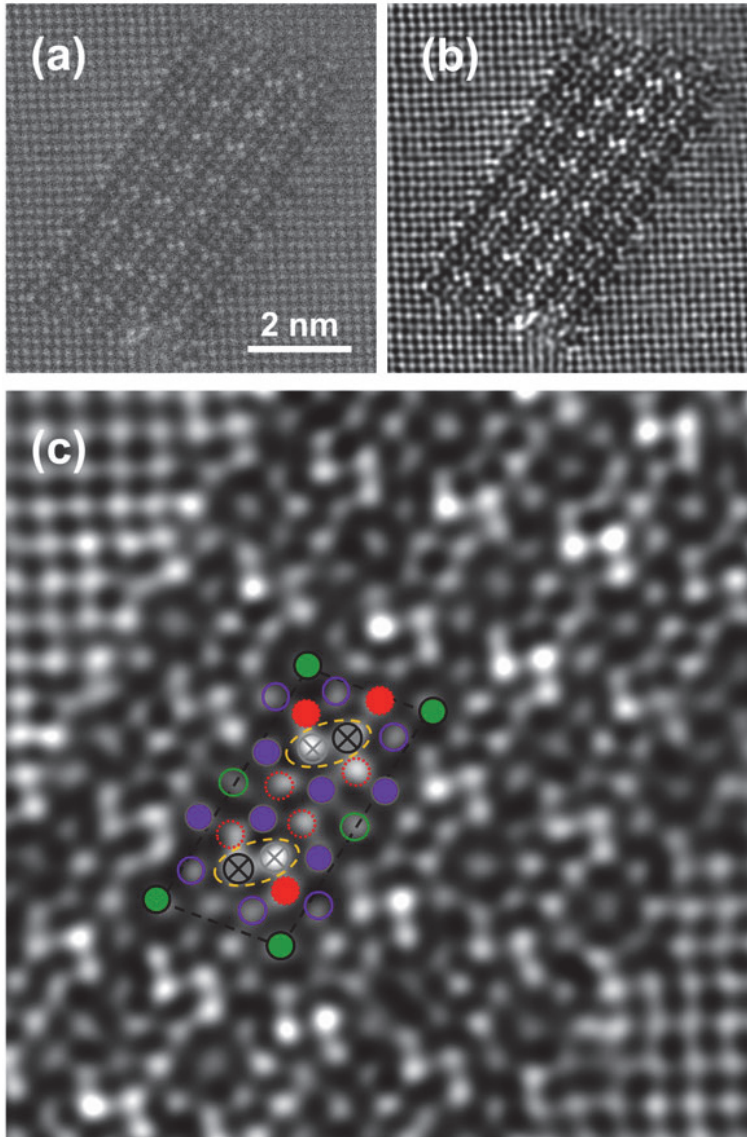
Figure 8. HAADF-STEM images of a $\beta''$ precipitate cross-section taken along $\langle 0\,0\,1 \rangle$ Al for LZ4 after ageing for 12 h. (a) Unprocessed image, (b) FFT filtered image of (a) and (c) enlarged image of (b) with overlay of a unit cell of the $\beta''$ phase. See legend in Figure 10.

and Si sites in the U2 phase [8], see Figures 5 and 10. Some Zn is observed in Al fcc sites, as can be seen as an enrichment (of 'bright spots') at precipitate/matrix interface in Figure 6. This is probably a consequence of localized high interfacial strain, which could favour the Zn atoms with respect to Al. The observation resembles the case of Ag enrichment of the Al matrix around precipitates [19]. It is also observed that the
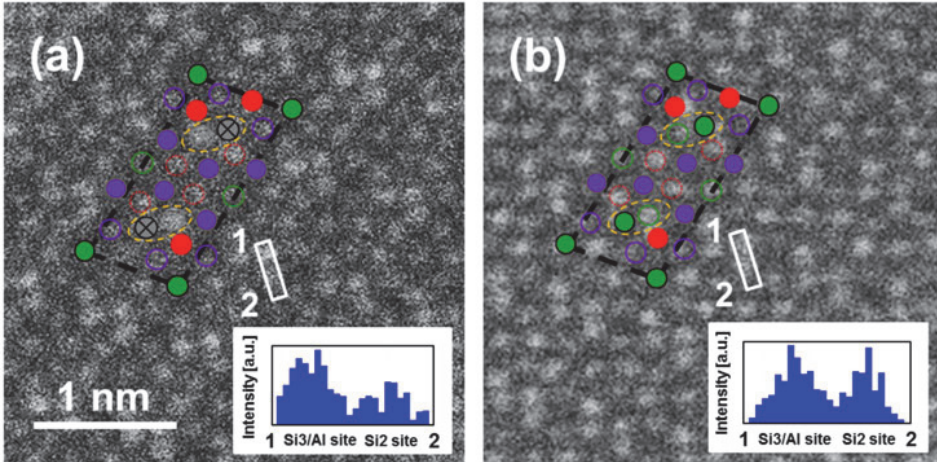
Figure 9. HAADF-STEM images of $\beta''$ precipitate cross-sections taken along $\langle 0\,0\,1 \rangle$ Al with corresponding intensity line profiles. (a) Enlarged unprocessed image of Figure 8 with corresponding intensity line profile (inserted). (b) Unprocessed image adopted from Ref. [32] taken from the similar alloy composition *without Zn* at peak hardness condition and the similar HAADF-STEM experimental condition, with corresponding intensity line profile (inserted). The intensity line profiles were taken from the white rectangle marked 1 to 2, shown in (a) and (b), respectively. Atomic overlays of a $\beta''$ phase unit cell are shown. See legend in Figure 10.

structure of the $\beta'_{Ag}$ disordered precipitates contains fragments and/or unit cell of the $\beta''$ phase, see Figures 5 and 7. Apart from the disordered precipitates, a perfect $\beta''$ precipitate was also observed, as shown in Figure 8. In the case of the $\beta''$ precipitate, Zn is only been observed at the Si3/Al sites [2,3], see Figures 8 and 10. Intensity line profile analyses show distinct higher intensity at the Si3/Al sites than another Si site. In addition, for a $\beta''$ precipitate in Zn-free Al–Mg–Si alloys, an intensity line profile for each Si site gives similar intensity, see comparison in Figure 9. These observations can support the incorporation of Zn at the Si3/Al sites in the $\beta''$ precipitate in the present work. The contrast of these Zn atomic columns is relatively weak although it is higher than intensities of the Si columns, which indicates a low Zn occupancy in the site. It is interesting to note that the Si3/Al site in $\beta''$ phase is locally identical to the Al site in the U2 phase, as these precipitates show close structural similarities, see Figure 10.

All these observations show that the general effect of Zn on precipitate structure is weak, as no new Zn-containing precipitate types have been observed. In other words, Zn does not alter precipitation sequence in the Al–Mg–Si system. Zn is rather incorporated into the structures of known precipitates by partly replacing other elements. The overall fraction of Zn in such precipitates is small. A simple calculation assuming 100% Zn occupancy in all Zn-containing columns in the precipitates shown in Figures 5, 7 and 8 (which is never the case based on the Zn-contrast) would set the highest limit of Zn to 18 at% in $\beta''$ precipitates, and to 18 at% and 11 at% in the disordered precipitates shown in Figures 5 and 7, respectively. Further investigation including quantitative HAADF-STEM image simulations and first principle calculations will have
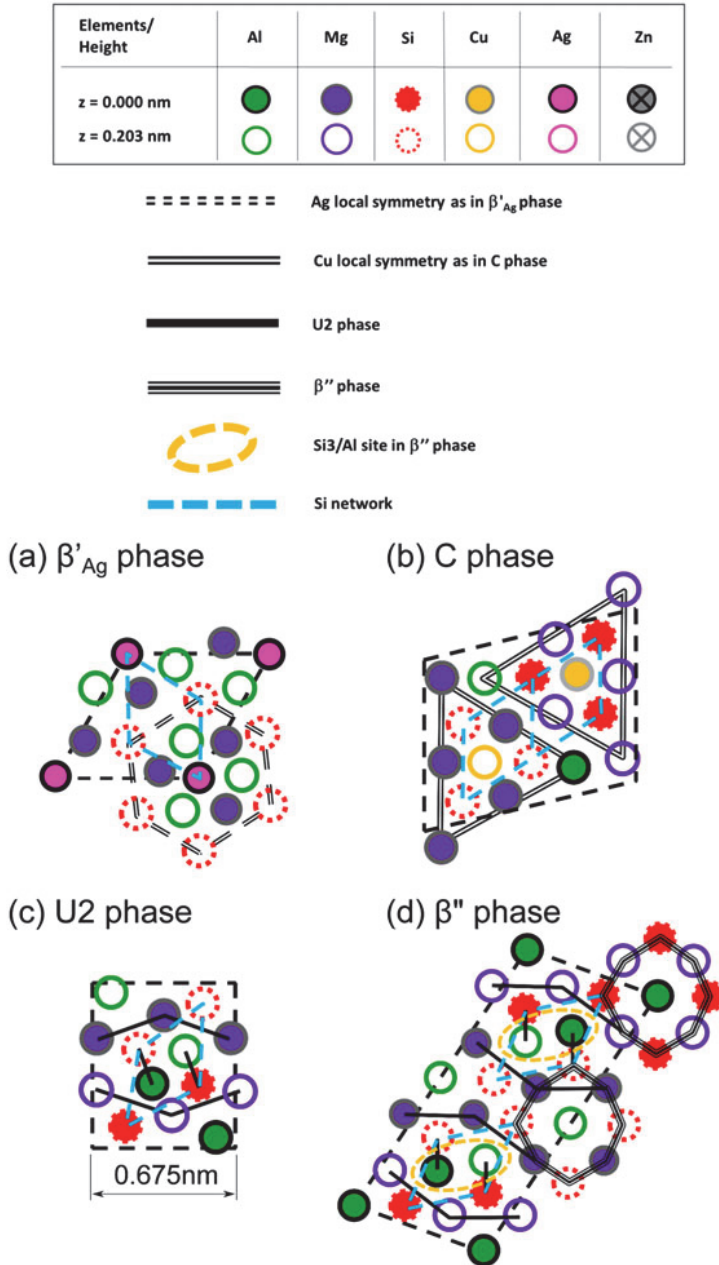
Figure 10. Legend representing atomic overlays in Figures 5, 7, 8 and 9 and schematic drawings of unit cells of the encountered metastable precipitates: (a) the $\beta'_{Ag}$ phase [19], (b) the C phase [30], (c) the U2 phase [8] and (d) the $\beta''$ phase with assumed Mg4Al3Si4 composition [2,3], all drawn to the same scale. Columns containing Zn appear as replacing the Ag and Al atomic columns in the $\beta'_{Ag}$ phase, the Cu atomic columns in the C phase, the Al and Si atomic columns in the U2 phase and the Al atomic columns in the $\beta''$ phase, see Figures 5, 7, 8 and 9.

to be performed for a better estimation of the Zn occupancies in the Zn-containing atomic columns.

## 4. Conclusions

The effects of Zn additions (up to 1 wt%) on precipitate microstructures, mechanical properties, corrosion properties and precipitate structures in Al–Mg–Si alloys have been investigated as a function of ageing at 185 °C. It could be concluded that Zn additions up to 0.1 wt% do not have a measurable influence on these properties and parameters. However, a slight increase in material's hardness and a decrease in electrical conductivity have been detected at 1 wt% Zn. The higher hardness correlates with a quantified increase in precipitate number density and presence of Zn in solid solution. The lower electrical conductivity suggests more Zn exists in solid solution. No precipitates of the Al–Zn–Mg system have been detected, instead all investigated areas showed needles parallel to $\langle 0\,0\,1 \rangle$ Al, characteristic for the Al–Mg–Si system. Zn segregation along grain boundaries was observed in the peak-aged condition of LZ4. This was found to be linked to high IGC susceptibility. The IGC susceptibility was lower in an under-aged condition. Most precipitates had disordered cross-sections, while some $\beta''$ were also observed. All disordered precipitates were based on the Si-network and incorporated fragments of known metastable phases in the Al–Mg–Si(–Cu) system. Low amounts of Zn have been observed to enter the structures of all investigated precipitates. However, Zn does not alter precipitation sequence of the Al–Mg–Si system, but makes precipitate disordered. Most Zn-containing atomic columns had low and fluctuating Zn occupancies. These columns occupy positions both in-between the columns of the Si-network, or replacing the Si-network columns. Weak Zn preference for certain atomic sites was found.

## References

[1] G.A. Edwards, K. Stiller, G.L. Dunlop and M.J. Couper, Acta Mater. 46 (1998) p.3893.
[2] S.J. Andersen, H.W. Zandbergen, J. Jansen, C. Træholt, U. Tundal and O. Reiso, Acta Mater. 46 (1998) p.3283.
[3] H.S. Hasting, A.G. Frøseth, S.J. Andersen, R. Vissers, J.C. Walmsley, C.D. Marioara, F. Danoix, W. Lefebvre and R. Holmestad, J. Appl. Phys. 106 (2009) p.123527.
[4] C.D. Marioara, S.J. Andersen, H.W. Zandbergen and R. Holmestad, Metall. Mater. Trans. A 36 (2005) p.691.
[5] C.D. Marioara, H. Nordmark, S.J. Andersen, R. Holmestad and R. Holmestad, J. Mater. Sci. 41 (2006) p.471.

[6] R. Vissers, M.A. van Huis, J. Jansen, H.W. Zandbergen, C.D. Marioara and S.J. Andersen, Acta Mater. 55 (2007) p.3815.

[7] S.J. Andersen, C.D. Marioara, R. Vissers, A. Frøseth and H.W. Zandbergen, Mater. Sci. Eng. A 444 (2007) p.157.

[8] S.J. Andersen, C.D. Marioara, A. Frøseth, R. Vissers and H.W. Zandbergen, Mater. Sci. Eng. A 390 (2005) p.127.

[9] K. Matsuda, Y. Sakaguchi, Y. Miyata, Y. Uetani, T. Sato, A. Kamio and S. Ikeno, J. Mater. Sci. 35 (2000) p.179.

[10] C.D. Marioara, S.J. Andersen, T.N. Stene, H. Hasting, J. Walmsley, A.T.J. Van Helvoort and R. Holmestad, Phil. Mag. 87 (2007) p.3385.

[11] D.J. Chakrabarti and D.E. Laughlin, Prog. Mater. Sci. 49 (2004) p.389.

[12] C. Cayron, L. Sagalowicz, O. Beffort and P.A. Buffat, Phil. Mag. A 79 (1999) p.2833.

[13] K. Matsuda, Susumu I., Yasuhiro U. and Tatsuo S., Metall. Mater. Trans A 32 (2001) p.1293.

[14] L. Arnberg and B. Aurivillius, Acta Chem. Scand. 34 (1980) p.1.

[15] R. Bjørge, C.D. Marioara, S.J. Andersen and R. Holmestad, Metall. Mater. Trans A 41 (2010) p.1907.

[16] R. Bjørge, P.N.H. Nakashima, C.D. Marioara, S.J. Andersen, B.C. Muddle, J. Etheridge and R. Holmestad, Acta Mater. 59 (2011) p.6103.

[17] R. Bjørge, S.J. Andersen, C.D. Marioara, J. Etheridge and R. Holmestad, Philos. Mag. 92 (2012) p.3983.

[18] K. Matsuda, K. Kido, T. Kawabata, Y. Uetani and S. Ikeno, J. Jpn. Inst. Light Met. 53 (2003) p.528.

[19] C.D. Marioara, J. Nakamura, K. Matsuda, S.J. Andersen, R. Holmestad, T. Sato, T. Kawabata and S. Ikeno, Philos. Mag. 92 (2012) p.1149.

[20] T. Saito, S. Muraishi, C.D. Marioara, S.J. Andersen, J. Røyset and R. Holmestad, Metall. Mater. Trans. A 44 (2013) p.4124.

[21] S. Wenner, C.D. Marioara, S.J. Andersen and R. Holmestad, Mater. Sci. Eng. A 575 (2013) p.241.

[22] L.K. Berg, J. Gjønnes, V. Hansen, X.Z. Li, M. Knutson-Wedel, G. Waterloo, D. Schryvers and L.R. Wallenberg, Acta. Mater. 49 (2001) p.3443.

[23] G. Sha and A. Cerezo, Acta. Mater. 52 (2004) p.4503.

[24] C.D. Marioara, W. Lefebvre, S.J. Andersen and J. Friis, J. Mater. Sci. 48 (2013) p.3638.

[25] S.J. Andersen, Metall. Mater. Trans. A 26 (1995) p.1931.

[26] S.J. Pennycook and D.E. Jesson, Phys. Rev. Lett. 64 (1990) p.938.

[27] P.D. Nellist and S.J. Pennycook, Adv. Imag. Elect. Phys. 113 (2000) p.147.

[28] G. Svenningsen, M.H. Larsen, J.C. Walmsley, J.H. Nordlien and K. Nisancioglu, Corros. Sci. 48 (2006) p.1528.

[29] M.H. Larsen, J.C. Walmsley, O. Lunder and R.H. Mathiesen, J. Electrochem. Soc. 155 (2008) p.C550.

[30] M. Torsæter, F.J.H. Ehlers, C.D. Marioara, S.J. Andersen and R. Holmestad, Phil. Mag. 92 (2012) p.3833.

[31] T. Saito, C.D. Marioara, S.J. Andersen, W. Lefebvre and R. Holmestad, Phil. Mag. 94 (2014) p.520.

[32] P.H. Ninive, A.S. Strandlie, S. Gulbrandsen-Dahl, W. Lefebvre, C.D. Marioara, S.J. Andersen, R. Holmestad and O.M. Løvvik, Acta Mater. 69 (2014) p.126.

# Paper V

**HAADF-STEM and DFT investigations of the Zn-containing $\beta''$ phase in Al-Mg-Si alloys**

Takeshi Saito, Flemming J.H. Ehlers, Williams Lefebvre, David Hernandez-Maldonado, Ruben Bjørge, Calin D. Marioara, Sigmund J. Andersen and Randi Holmestad

# HAADF-STEM and DFT investigations of the Zn-containing $\beta$" phase in Al-Mg-Si alloys

Takeshi Saito[a,*], Flemming J.H. Ehlers[a], Williams Lefebvre[b], David Hernandez-Maldonado[b], Ruben Bjørge[a], Calin D. Marioara[c], Sigmund J. Andersen[c], Randi Holmestad[a]

[a]*Department of Physics, Norwegian University of Science and Technology, N-7491 Trondheim, Norway*
[b]*Université de Rouen, GPM, UMR CNRS 6634 BP 12, Avenue de IUniversit, 76801 Saint Etienne du Rouvray, France*
[c]*SINTEF Materials and Chemistry, N-7465 Trondheim, Norway*

## Abstract

The Zn-containing $\beta$" phase in Al-Mg-Si alloys has been investigated by aberration corrected high angle annular dark-field scanning transmission electron microscopy (HAADF-STEM), combined with density functional theory (DFT) calculations. The mean intensity of one Si site of the $\beta$" phase is higher than the other Si sites, indicating that this site is partially occupied by Zn atoms. This is in agreement with DFT calculations suggesting that this Si site is preferential for Zn incorporation. The Zn occupancy depends on the region in the precipitate and the Zn distribution along the precipitate needle. DFT calculations predict that the Zn-Zn interaction is weak suggesting that Zn atoms are not clustering but are uniformly distributed along the atomic columns. Zn incorporation has a weak influence on the $\beta$" phase. The unit cell dimensions of the phase do not change.

*Keywords:* aluminum alloys; precipitate; STEM HAADF; DFT; atomic structure; image analysis

## 1. Introduction

Al-Mg-Si alloys are heat-treatable materials used in many industrial applications on the basis of their characteristic properties: high strength-to-weight ratio, good formability and corrosion resistance. The main property of these heat-treatable materials is a significant increase in hardness during a final isothermal heat treatment (artificial aging) at an adequate temperature and time. This is due to the formation of large numbers of nano-sized semi-coherent metastable precipitates, hindering dislocation movement. The precipitates form from a super saturated solid solution (SSSS) and are controlled by the alloy composition and the thermo-mechanical history. The materials strength ultimately depends on the precipitate structure and the microstructures they produce (sizes, numbers and orientations). Further, composition, morphology and aspect ratio for a precipitate may be affected by small amounts of a different type of solute atoms. This could be triggered by direct incorporation of these additional solute atoms in the existing precipitate, either in the bulk (change of cell dimensions) or at the interface (change of interfacial energies). Such alloy modifications are of growing interest due to increasingly specific industrial requirements for materials properties.

The precipitation sequence of Al-Mg-Si alloys is as follows [1-9]:

---

*Corresponding author
*Email address:* `takeshi.saito@ntnu.no` (Takeshi Saito)

$$SSSS \rightarrow atomic\ clusters \rightarrow GP\ zones\ (pre-\beta") \rightarrow \beta" \rightarrow \beta', U1\ (Type-A), U2\ (Type-B), B'\ (Type-C) \rightarrow \beta, Si$$
(1)

The U1, U2 and B' phases are also known as Type A, Type B and Type C, respectively [10].

The $\beta$" phase is the most important metastable phase encountered together with GP zones, leading to the finest microstructure at peak hardness condition [1]. The monoclinic structure of the $\beta$" phase was identified more than a decade ago [2, 9], see Figure 1 (a) and Table 1. By contrast, the composition has been still widely discussed [3, 11-15]. The $\beta$"/Al matrix interface is fully coherent and has {130} and {320} habit planes. The orientation relationships with the face-centered cubic (fcc) Al matrix are:

$$[230]Al//[100]\beta"; [001]Al//[010]\beta"; [-310]Al//[001]\beta".$$
(2)
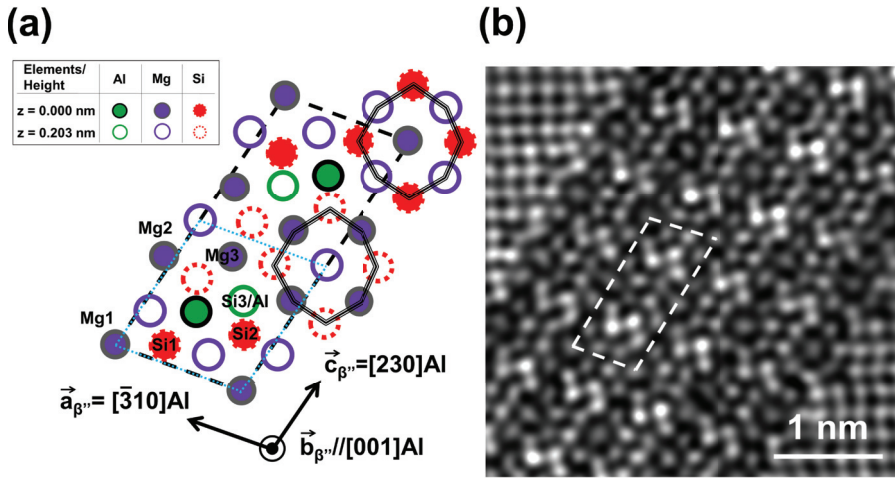


Figure 1. (a) A schematic illustration of the $\beta$" phase. The different sites are labeled. Characteristic eye-like atomic coordination around the Mg1 site can be seen (triple solid black line). The dashed black rectangle (white rectangle in (b)) represents a unit cell of the $\beta$" phase and the dashed blue one a primitive cell used in the DFT calculations. (b) A HAADF-STEM image of $\beta$" precipitate cross section taken along ⟨001⟩Al for alloys with 0.42at%Zn after isothermal heat treatment for 12 hours at 185°C. The image was filtered using Fast Fourier transform (FFT) filtering to reduce noise using a circular band pass mask that removed all periods shorter than 0.15 nm (adopted from Ref. [16]).

Table 1: Structural overview and atomic site positions (x, y, z) in the $\beta$" phase [2, 3].

| Composition | Mg5Al2Si4 |
|---|---|
| Space group | C2/m |
| Lattice parameter (nm) | a=1.516, b=0.405, c=0.674, $\beta$=106° |
| Mg1 site | 0, 0, 0 |
| Mg2 site | 0.347, 0, 0.074 |
| Mg3 site | 0.423, 0, 0.636 |
| Si1 site | 0.054, 0, 0.661 |
| Si2 site | 0.190, 0, 0.232 |
| Si3/Al site | 0.211, 0, 0.626 |

The lattice misfits along these directions are in the order of 3.8%, 0% and 5.3%, respectively [2, 9] from which a needle shaped precipitate, directed along [010]$\beta$", results. Recent extensive experimental atom probe tomography

2

(APT) studies suggested [3, 12, 13] that the Mg/Si ratio is close to 1.1 which differs from the originally proposed $\beta$"-Mg5Si6 phase. Both experimental studies and theoretical density functional theory (DFT) calculations [3, 12-14] have proposed the Mg5Al2Si4 composition as the minimum energy configuration for the $\beta$" phase. The most recent DFT calculations [14] deduced very weak enthalpy differences for $\beta$"-Mg5-xAl2+xSi4 (-1 < x < 1). Further, the $\beta$" phase could have compositional variations within a single precipitate, as suggested by the most recent experimental study [15]. These results imply the possibility of a strong sensitivity for the $\beta$" phase composition, aspect ratio and ultimately the microstructure, to incorporation of foreign solute atom types.

In the present work, we investigate the incorporation of Zn in $\beta$", utilizing a series of experimental and theoretical methods, from the perspective of a general analysis of foreign solute atom types in this phase. It has previously been demonstrated, by high-angle annular dark-field scanning transmission electron microscopy (HAADF-STEM), that Zn is confined to the Si3/Al sites of the $\beta$" phase, see Figure 1 (b). The contrast of these Zn-containing atomic columns was weak, which indicates a low Zn partial occupation in the site [16]. Our main interest in this work is how to extract, to the largest possible degree, further information towards an improved understanding of a well-known phase with foreign solute atom types here, the $\beta$" phase with the Zn incorporation.

It is well known that information acquired from HAADF-STEM images is limited due to the projection of the 3-dimensional (3D) atomic structure and complicated scattering mechanisms [17, 18]. We aim at circumventing this limitation by utilizing both a statistical analysis and simulations of the HAADF-STEM intensities, as well as DFT calculations. This attempt should serve to highlight the present limitations of the general structural analysis, as well as the key areas where further investigations are needed.

## 2. Experimental Procedure

### 2.1. Materials and HAADF-STEM images

An alloy with composition Al-0.52Mg-0.38Si-0.42Zn (at%) was prepared by extrusion from cast billets. This composition is close to the commercial 6060 Al alloy, except for the Zn addition. Other impurities are below 0.01 at%. The alloy was solution heat treated at $540°C$ for 1 h, kept for 4 h at room temperature and isothermally heat treated at $185°C$ for 12 h. This heat treatment procedure induces peak hardness condition. The preparation and heat treatment are identical to the previous work [16]. HAADF-STEM specimens were prepared by electropolishing with a Tenupol 5 machine (Struers, Denmark). The electrolyte consisted of 1/3 HNO3 in methanol and the solution was kept at a temperature between -20$°C$ and -35$°C$. In order to reduce contamination during observation, all specimens were ion-milled by a precision ion polishing system (PIPS Gatan). In addition, all specimens were plasma cleaned before HAADF-STEM imaging in order to reduce the effect of contamination, using a Model 1020 Plasma Cleaner (Fischione Instruments). The HAADF-STEM images were taken by a spherical aberration (Cs) probe-corrected JEOL ARM200F STEM with a Shottky field emitter operating at 200 kV. The probe size was 0.1 nm. The collection angle of the HAADF detector was in the range of 45-150 mrad. The thickness of the specimen was around 50 nm. The HAADF-STEM technique provides atomic number (Z) contrast with the intensity proportional to $Z^{1.7-1.9}$ [17, 18]. This enables to distinguish the heavier Zn ($Z_{Zn} = 30$) enriched atomic columns from those of Mg ($Z_{Mg} = 12$), Al ($Z_{Al} = 13$) and Si ($Z_{Si} = 14$) in the precipitate structures.

### 2.2. Analysis of HAADF-STEM intensity by a statistical approach

The intensities of the atomic column in the precipitates were identified using a statistical analysis [19, 20]. The HAADF-STEM intensity can be approximated as a convolution of an object function and a probe function as follows [18]:

$$I(\vec{R}) = O(\vec{R}) \otimes P(\vec{R}) \tag{3}$$

where $\vec{R}$ is the position of the STEM probe, $O(\vec{R})$ is the objective function and $P(\vec{R})$ is the probe function. The probe function represents the intensity distribution of the convergent scanning beam, which depends on acceleration voltage, objective aperture, convergence angle and defocus [18]. On the other hand, the objective function describes the scattering potential of atomic columns influencing the detector. This is peaked at the atomic column positions and can be modeled as a Gaussian function [19, 20]. The estimated scattered intensity for an atomic column is expected to be identical for columns with the same chemical composition. In this manner, histograms of the estimated peak

3

intensity of the atomic columns can be drawn [19]. This methodology [19, 20] has been developed to count nano-sized particles from HAADF-STEM images. We here apply the method to identify the atom types in the various columns assuming a fixed number of atoms through a column. This has recently been applied to investigate the $\beta$" phase without Zn incorporation, deducing atomic column types [15].

Following the methodology proposed by van Aert et al [19, 20], integrated column intensities were measured for each atomic column in the experimental images (i.e. without any filtering) and histograms of column intensities were fitted with a Gaussian mixture model using a statistical analysis in which the number of Gaussian components are determined from the variation of the ICL (integrated classification likelihood) criterion. This approach enables the intensity distribution of each atomic column to be estimated. Consequently, the intensity distribution of the Gaussian components for each atomic column can be discussed.

### 2.3. HAADF-STEM image simulations

In order to clarify how a partial occupancy of Zn at the Si3/Al site in the $\beta$" phase influences the HAADF-STEM intensity, three different Zn occupancies, 0%, 5% and 10% of the Si3/Al site were simulated. In addition, to investigate how the intensity differs depending on the distribution of Zn along a precipitate needle, three different distributions of Zn along the electron beam direction were considered: even distribution throughout the column, and top and bottom Zn enrichments. These three distributions are illustrated in Figure 2. In this manner, we can extract 3-dimensional information of the precipitate atomic structure from the projected HAADF-STEM images.
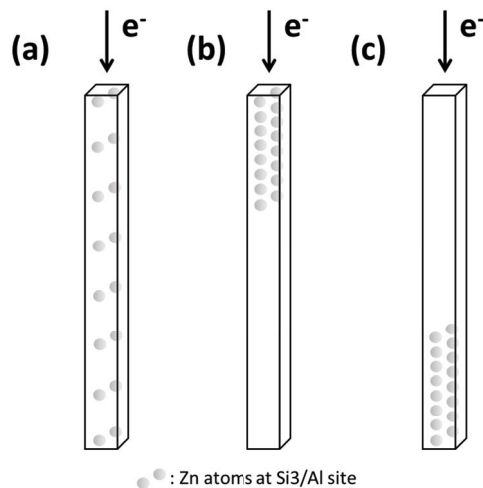


Figure 2. Schematic image of precipitate columns for different distributions of Zn along the electron beam direction: (a) even distribution of Zn atoms throughout the column, (b) top and (c) bottom Zn atom enrichments. The precipitate column represents one primitive unit cell.

The HAADF-STEM image simulations were conducted using the frozen phonon multislice program provided by the QSTEM package [21] with slice thickness of 0.205 nm (half a unit cell, see Table 1). The convergence semi angle of the electron probe was 20 mrad and the HAADF collector angles were between 45 and 150 mrad. These values were the same as in the experiment. The simulated structures were assumed (see Table 1) to adopt the experimentally reported [2] $\beta$" cell dimensions, regardless of the selected phase composition. The HAADF-STEM images were calculated for every two slices. Each simulation was averaged over 30 frozen phonon configurations. The chosen Debye-Waller factors for each site matched those of the elemental phases at 300 K: 0.8333, 1.8837 and 0.5261 Å$^2$ for Al, Mg and Si, respectively [22].

4

## 2.4. Density functional theory (DFT) calculations

The DFT [23, 24] calculations of the Zn containing $\beta$" phase have three key purposes. We attempt to:

- Compute the energy gain for a Zn atom incorporated in $\beta$", as obtained relative to having this atom in solid solution.

- Clarify the level of Zn induced changes to the $\beta$" composition.

- Elucidate the strength of Zn-Zn interactions in $\beta$" (and thus, in turn, the expected degree of Zn clustering in the precipitate)

To capture the state of Zn in the precipitate, calculations on a bulk $\beta$" system are needed. Due to the expected low Zn occupancy in $\beta$", we modelled the precipitate using supercells, comprising $N_a \times N_b \times N_c$ primitive $\beta$" unit cells (see Figure 1(a)) along $\vec{a}_{\beta"}$, $\vec{b}_{\beta"}$, $\vec{c}_{\beta"}$, respectively. Initially, we incorporated one Zn atom in a $1 \times 4 \times 1$ cell, testing the preference for each non-equivalent site in $\beta$", in a manner to be described below. To examine Zn clustering tendencies, we introduced a second Zn atom on an equivalent site, varying the Zn-Zn separation. Those studies involved both the $1 \times 4 \times 1$ cell as well as $1 \times 2 \times 2$ and $2 \times 2 \times 1$ cells. For the description of Zn in solid solution, we included one Zn atom in a 108 atom fcc Al supercell, comprising $3 \times 3 \times 3$ conventional fcc unit cells.

To highlight the drive for Zn incorporation on a given site $\Xi$ in a chosen Zn-free $\beta$" configuration (labelled $\beta$"$_0$ for brevity below), we adopted the following strategy in calculations: whenever  hosted a solute atom in $\beta$"$_0$, we introduced an artificial Al defect on this site, for each primitive cell making up the full supercell. We then considered two possible scenarios:

- One Zn atom removed from the Al supercell and incorporated on site $\Xi$, with the Al atom present here expelled to the Al matrix.

- The same substitution process examined for the solute atom occupying site $\Xi$ before the introduction of the artificial Al defects.

In this manner, we probe not only the drive for Zn incorporation on each given site in $\beta$", but also the level of competition with the solute atom most likely occupying this site when no Zn is present in the alloy. Formally, the system enthalpy change $\Delta H(\beta"_0; X \rightarrow \Xi)$ due to one of these substitution processes may be written as:

$$\Delta H(\beta"_0; X \rightarrow \Xi) = H(\beta"_0; 3 \times \{Al \rightarrow \Xi\}; 1 \times X \rightarrow \Xi) + H(fccAl) - H(\beta"_0 4 \times Al \rightarrow \Xi) - H(fccAl; 1 \times \{X \rightarrow S\}). \quad (4)$$

Here, H denotes the calculated enthalpy for the system described in parenthesis (first argument: host material; remaining arguments: substitution processes, number of processes $\times$ atom $\rightarrow$ site), with X specifying the element incorporated in the precipitate and S denoting a substitutional site in the Al host lattice. For sites $\Xi$ hosting Al in $\beta$"$_0$, the replacement processes Al $\rightarrow \Xi$ have no practical effect. However, even for this situation we consider incorporation of the most likely solute atom Mg/Si on site $\Xi$ for comparison with the Zn incorporation. Following [3, 14], we considered three different (energetically competitive) $\beta$"$_0$ configurations; Mg4Al3Si4 (Al on Mg1, Si3 sites in Figure 1 (a)), Mg5Al2Si4 (Al on Si3 sites), and Mg6AlSi4 (Al on one Si3 site).

All computational studies were performed at 0 K, employing Vanderbilt ultrasoft pseudopotentials [25] as implemented in the plane wave (PW) based Vienna Ab initio Simulation Package (VASP) [26, 27]. For the description of the exchange-correlation functional, the Perdew-Wang generalized gradient approximation [28] was used. The chosen PW cut-off in simulations was 234 eV, with (12, 6, 14) Monkhorst-Pack [29] k-point grids used for the $1 \times 4 \times 1$ $\beta$" supercell, and compatible grids for other cells. Generally, all structural parameters (cell dimensions, basis vector angles and atomic positions) were relaxed. The use of enthalpies over formation energies E in eq. (4) relates to our neglecting the influence of the (small) pressure-volume (PV) term distinguishing these quantities.

## 3. Results

### 3.1. HAADF-STEM intensity distribution of atomic columns by statistical analysis

Figure 3 shows an unprocessed HAADF-STEM image of a $\beta$" precipitate cross section taken along ⟨001⟩Al and the corresponding average HAADF-STEM intensity map. The average HAADF-STEM intensity map shows thickness variation in the matrix surrounding the precipitate, deduced by integrated intensity of a square area larger than the size of a projected column. Figure 4 shows the intensity map of the Si3/Al sites, and intensity distributions for each Mg site and each Si site in the precipitate. The following observations can be made from Figures 3 and 4:

5

- The intensity map shows a strong intensity variation depending on thickness of the scanned area. In addition, the intensity from the bulk precipitate is relatively lower than Al matrix. This is probably attributed to elastic lattice strain in the precipitate [30].

- While the intensity distributions for the Mg sites are similar to each other, those for the Si sites show clear differences among the sites. The mean intensity of the Si3/Al sites is clearly larger than other Si sites. This is in good agreement with a partial occupation of Zn in the Si3/Al sites.

- Intensities in the Si3/Al sites are lower close to the interfaces along [230]Al; the higher intensity comes from the bulk Si3/Al sites, not from either near or at interfaces along [230]Al. Interestingly, this tendency cannot be observed for the interfaces along [-310]Al, but higher intensities do not stand at the Si3/Al sites on the interfaces along [-310]Al.

- One of the interfaces along [230]Al is non-systematically brighter than the bulk (bottom part of the precipitate shown in Figure 4(a)). This might be non-systematical Zn enrichment at the precipitate/matrix interface. Similar observations were made for disordered precipitates examined in previous work [16].

- The width of the intensity distribution for the Si2 and Si3/Al sites is larger than that for the Si1 site.
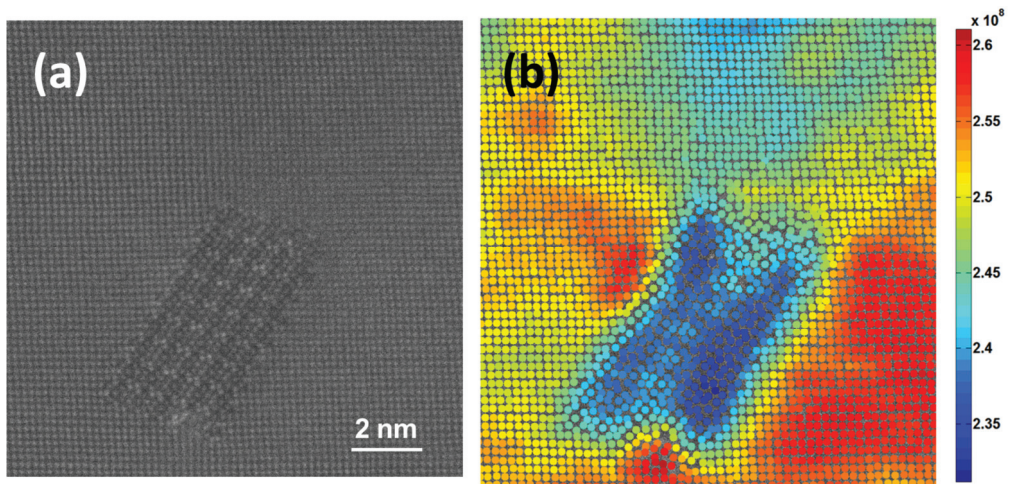


Figure 3. (a) Unprocessed HAADF-STEM image of a Zn-containing $\beta$'' precipitate cross section taken along ⟨001⟩Al and each colored overlay point on atomic columns position in (b) represent the integrated HAADF-STEM intensity of a square area of 1.25 x 1.25 $nm^2$ (i.e. much larger than the size of a projected column). The overlay therefore represents the average thickness variations in the matrix surrounding the precipitate. The HAADF intensity is displayed in arbitrary units.

*3.2. Simulated HAADF-STEM intensity*

Figure 5 shows simulated intensities for the Si3/Al site as a function of thickness for 5% and 10% Zn occupancies with different Zn distributions along the electron beam direction as shown in Figure 2. As a reference, the intensity for all Si sites (Si1, Si2 and Si3) in the $\beta$'' phase without Zn occupation are also shown in Figure 5. As expected, the intensity increases with increasing thickness. Since an intensity variation in a HAADF-STEM image is approximately linear with increasing thickness [18], an intensity gradient was deduced by linear interpolation. Table 2 lists the intensity gradient with thickness, corresponding to Figure 5. The intensities depend on Zn occupancy and the distribution. The following observations can be made from Figure 5 and Table 2:

- The intensity differences between Si sites are negligibly small, compared to the intensity variations in the case with partial Zn occupation.

- The presence of Zn increases the intensity, independent of the Zn distribution imposed along the electron beam direction.

6
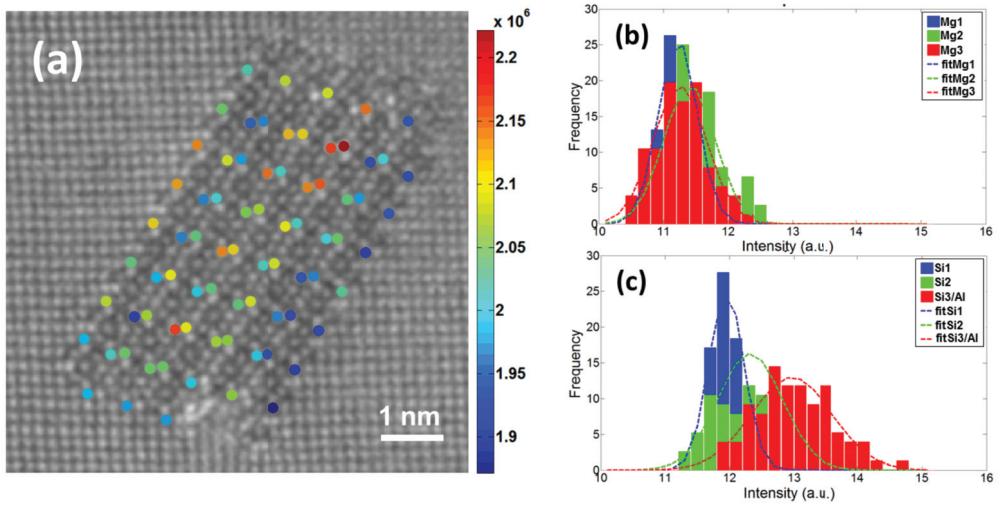
Figure 4. (a) Color mapping of the integrated intensity measured on the atomic Si3/Al sites. The HAADF-STEM intensity is displayed in arbitrary unit. Intensity distributions for (b) Mg sites and (c) Si sites in the precipitate. The non-systematically higher intensity columns (bottom part of the precipitate) are excluded in the statistics of intensity distributions.
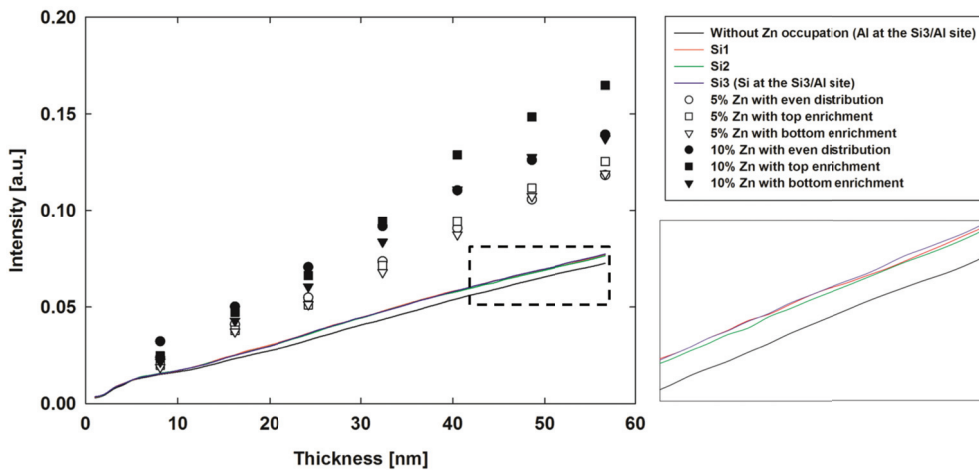


Figure 5. Simulated intensities of the Si3/Al site in the $\beta$" phase (points) as a function of thickness for 5% and 10% Zn occupancies with different Zn distributions along the electron beam direction, as given in the legend. As a reference (solid lines), the intensities of all Si sites (Si1, Si2 and Si3 sites) in the $\beta$" phase without Zn (assuming the conventional Mg5Si6 composition) occupation are also shown for Si atoms at all Si sites and Al atoms at the Si3/Al site (assuming the Mg5Al2Si4 and Mg4Al3Si4 compositions). See Table 2 for the intensity gradient increases with thickness. The right bottom rectangle corresponds the dashed rectangle for thickness above 40 nm.

- The intensity gradient with respect to thickness increases for each distribution the gradient is larger with 10% Zn occupancy than with 5% Zn occupancy.

- Variations of intensity gradients are observed depending on the Zn distribution along the column. These variations are weak in 5% Zn occupancy and lower thicknesses for 10% Zn occupancy. However, for 10% Zn occupancy and a larger thickness (more than around 40 nm), the intensity in top enrichment is higher than that in even distribution and bottom enrichment. These latter results indicate that determining the level of partial Zn occupancy from HAADF-STEM image intensities is not a trivial problem.

Table 2: Intensity gradients with thickness deduced by linear interpolation for 5% and 10% Zn occupancies with different distributions along the electron beam direction, corresponding to the points in Figure 5.

| Si3/Al sites | Gradient ($\times 10^{-3}$) |
|---|---|
| Without Zn occupation | 1.2 |
| 5% Zn with even distribution | 2.0 |
| 5% Zn with top enrichment | 2.2 |
| 5% Zn with bottom enrichment | 2.1 |
| 10% Zn with even distribution | 2.3 |
| 10% Zn with top enrichment | 3.0 |
| 10% Zn with bottom enrichment | 2.5 |

### 3.3. Formation enthalpy of Zn incorporation

Figure 6 shows the calculated energies $\Delta H(\beta''_0; X \rightarrow \Xi)$ obtained when considering incorporation of X = Zn/Mg/Si on the various sites $\Xi$ in an initially Zn free precipitate $\beta''_0$, as described with eq. (4). Given the chosen supercell sizes (see section 2.4), the examined Zn occupancy is 12.5% for all sites but Mg1, where the occupancy is twice as high. The following observations can be made:

- For the Si3/Al sites, where Zn atoms were observed experimentally, theory predicts weak binding (0.18 eV/Zn atom or higher), with little variation for the three different $\beta''_0$ configurations and a minimum at the Mg5Al2Si4 composition.

- Compared to Zn, Mg may occupy the Si3/Al sites at a similar energy gain, but with the Mg1, Mg2, and Mg3 sites clearly favored.

- Compared to the Si3/Al site, Zn is predicted to bind more strongly on the Si1 and Si2 sites. Here, however, the competing Si atom is always binding more favorably. The only exception is the Si1 site in the Mg4Al3Si4 composition where Zn incorporation is competitive.

We draw the following conclusions from these results: according to theory, Zn incorporation on the Si3/Al site in $\beta''$ may be expected, with Zn admitted as a defect in the precipitate, rather than stabilizing a new phase. In particular, this statement reflects the apparent absence of any strong preference of Zn for a particular composition of the $\beta''$ phase.

Additional studies probing the level of Zn-Zn interactions in $\beta''$ were performed only for Zn on Si3/Al sites in $\beta''$Mg5Al2Si4. The results suggest an almost complete indifference of the system energy to the Zn separation, implying that Zn is statistically distributed on the Si3/Al sites, as opposed to clustering, see Figure 7 (a).

The variation in the Zn binding energy as a function of distance from the interface was also examined for Zn on the Si3/Al site in $\beta''$Mg5Al2Si4. Figure 7 (b) shows the results of the binding energy. This indicates that Zn atoms are preferentially incorporated in bulk $\beta''$ - not close to the interface.

## 4. Discussion

Although we see strong intensity variations due to thickness variations and elastic strain, the statistical analysis of the HAADF-STEM image intensities clearly indicates that the Si3/Al sites display a larger mean intensity compared to the Si1 and Si2 sites of the $\beta''$ phase. In addition, the intensity distribution for the Si3/Al sites is broader. The HAADF-STEM image simulations suggest that the intensity difference between Si sites is negligibly small, compared to intensity variations obtained with partial Zn occupations. Furthermore, DFT calculations predicted that the Si3/Al site should be the most favorable site for Zn incorporation in the $\beta''$ phase. These results are in good agreement with a partial occupation of Zn atoms in the Si3/Al sites. Note that the intensity distribution for the Si2 sites is also broader

8
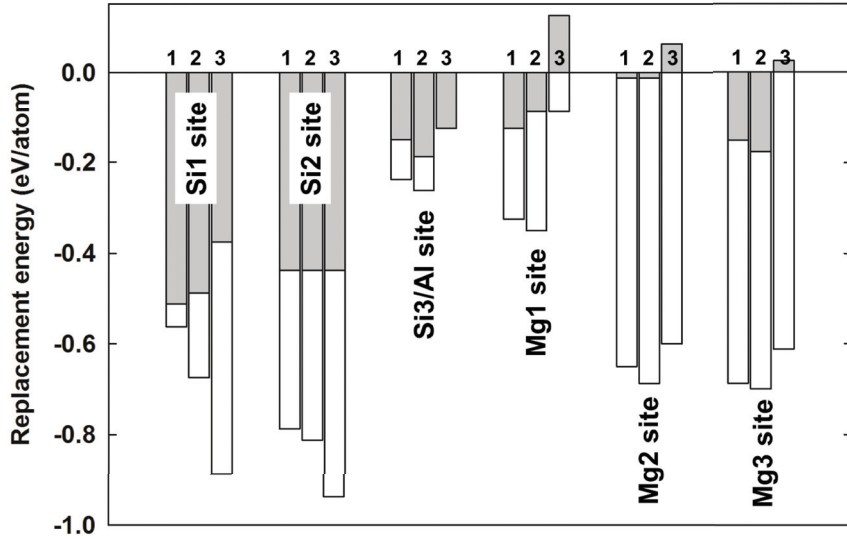
Figure 6.  Calculated bulk formation enthalpies of Zn incorporation in different sites of the $\beta$" phase with different compositions, 1: Mg4Al3Si4, 2:Mg5Al2Si4 and 3: Mg6AlSi4. Gray and white bars represent Zn-containing and Zn-free compositions, respectively.
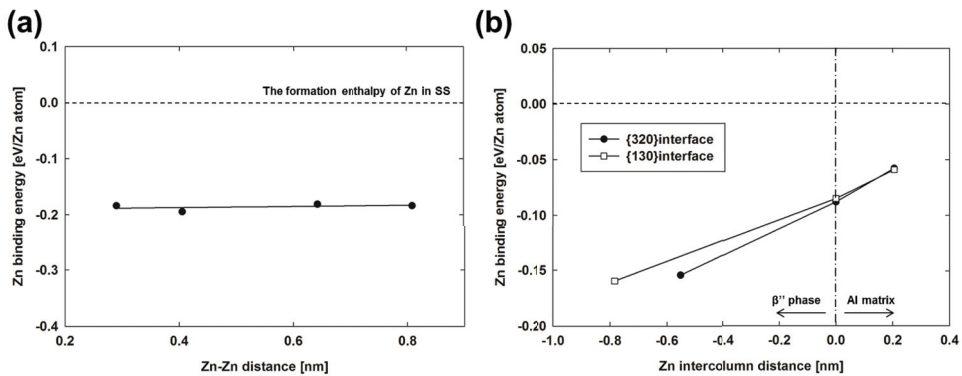


Figure 7. Zn binding energies at the Si3/Al site (a) as a function of distance between the Zn atoms along the precipitate needle direction, and (b) as a function of the intercolumn distance from the interfaces. The Zn binding energy 0 eV/Zn atom represents the formation enthalpy of isolated Zn in solid solution (SS). In (b), 0 nm represents the Si3/Al site at boundary of structural interface [14] and negative and positive values correspond to $\beta$" bulk side and Al matrix side, respectively.

9

127

and has slightly higher intensity than that for the Si1 sites, see Figure 4 (c). However, DFT calculations suggest that Zn is effectively less likely on the Si2 sites, compared to the Si3/Al (and even the Si1) sites. The broader intensity distribution for the Si2 sites might result from the Zn presence on the neighboring Si3/Al sites which are partially occupied by Zn atoms, i.e. the increased intensity is due to electron channeling or cross-talk artefacts [31] between these sites. This could influence intensities along $\langle 001 \rangle$Al for a specimen thickness larger than 50 nm [32] - roughly the specimen thickness in this work. The intensity on the Mg sites was lower than on the Si sites. This suggests that the Mg sites are not occupied by Zn atoms, a conclusion also supported by the DFT calculations.

The higher intensities in Figure 4 (a) come from the bulk Si3/Al sites, as opposed to the precipitate/Al matrix interfaces and their vicinity, in case of the interface along [230]Al. We stress here that the average intensity in the bulk region (Figure 3(b)) is also higher than near the interface. This may be attributed to the elastic lattice strain on the $\beta$" precipitate, see the strain map in Ref [15]. We cannot exclude, on the basis of the present work, that this strain is appreciably affecting the Zn binding energy reduction near the interface. In particular, we note that the DFT results in Figure 7 (b) do not predict differences in the Zn behavior at the two interfaces. Further, the Zn binding energy in $\beta$" is always weak and as such susceptible to remaining errors in the calculations, e.g. finite temperature effects. To clarify whether strain or chemical effects are the more influential, DFT studies on strained supercells (following e.g. the methodology in Ref. [33]) as well as a closer experimental examination of compositional variations within the precipitate of Figure 3 (a) would be of interest.

The DFT results suggest (see Figure 6) that Zn on the Si3/Al site has only very weak preference for a particular $\beta$" composition. Since the Zn-free $\beta$" energy contours are equally weak, we cannot deduce solely from the above information how Zn may affect $\beta$" chemically. However, the results of Figure 6 also suggest that, in addition to the Si3/Al site, the Si1 site could be a competitive site for Zn incorporation in $\beta$"-Mg4Al3Si4. Experimentally, no Zn on the Si1 site is observed. Further, the intensity distributions for the Mg sites in Figure 4 (b) are highly similar. Those two observations suggest that the analyzed $\beta$" is unlikely to dominated by local regions with the Mg4Al3Si4 composition. Even with the significant theoretical incorporation of Zn in $\beta$", the cell dimensions and the structure of this phase change only weakly, preferably along the $\beta$" needle direction. It is inferred that Zn has a weak interaction with the $\beta$" phase, where it can be considered a defect preferentially located at the Si3/Al site.

The precise level of Zn occupancy at the Si3/Al site depends not only on the location within the precipitate, but also on the Zn distribution along the precipitate needle, as seen in the HAADF-STEM intensity analysis and simulations, respectively. The dependence on the distribution is weak at low Zn occupancy (5%). However, if the occupancy is 10% and the specimen thickness exceeds 40 nm, the intensities for top enrichment in Figure 5 are non-negligibly higher than the other distributions. The main reason for this dependence is a large influence of electron channeling (and/or de-channeling). In addition, the HAADF-STEM intensity generally depends on several factors: crystal structure and bonding, Debye-Waller factors, thickness and background intensity. These factors are decoupled influences on the HAADF-STEM intensity. As an example of the remaining complexities present here, a recent study [34] has shown that the HAADF-STEM intensity depends greatly on the Debye-Waller factors. Interestingly, the results indicated that Z-contrast of the HAADF-STEM intensity was no longer valid, but depending on crystal structure and bonding. Other examples of complexities to be considered can be mentioned: an inhomogeneous HAADF detector intensity [35] and static disorder in atomic columns due to occupation of more than one type of atom in the column - so called static atomic displacements [36].

The DFT calculations suggest that the Zn-Zn interactions are weak for the Si3/Al site in the $\beta$" phase. Based on these results, Zn is in favor of a uniform (statistical) distribution throughout the Si3/Al site column, as opposed to the clustering tendencies reflected by the top and bottom enrichment assumed in the HAADF-STEM image simulation, see Figure 2. In previous results [16], Zn was shown to induce only a low increase in Al-Mg-Si alloy precipitate number density, compared to Zn-free alloys, consistent with the suggested weak Zn influence proposed in the present study. Here, one thing has to be considered for the extreme case: in principle, a new superstructure with different symmetry would arise if the Zn atoms were periodically distributed. The Zn distribution could be determined from an HAADF-STEM image taken in the direction normal to the precipitate needle (90 degrees tilted from the present orientation). As the needles are thin (less than 10 nm), however, observation may be difficult due to the huge projected atomic overlap with fcc Al along in this direction.

10

## 5. Conclusions

A combination of statistical analysis and simulations of HAADF-STEM intensities, and DFT calculations has been used to extract further information from HAADF-STEM images of the Zn-containing $\beta$" phase in Al-Mg-Si alloys. Statistical analysis of HAADF-STEM intensities shows that the intensity distribution of the Si3/Al sites in the $\beta$" phase is broader for atomic site columns occupied by Zn. DFT calculations support that the Si3/Al sites are preferential sites for Zn incorporation. The occupancy of Zn atoms in the Si3/Al site is uncertain since it depends on the region in the precipitate and the distribution along the precipitate needle. The HAADF-STEM intensity varies depending on distribution of the Zn atoms in a column along a precipitate needle. As suggested from DFT calculations, Zn atoms may not be clustering since the Zn-Zn interaction is weak. This suggests that the Zn atoms are uniformly distributed throughout the column in the Si3/Al sites. The unit cell dimension does not change due to the Zn incorporation. Zn atoms have a weak influence on the $\beta$" phase in spite of the incorporation.

## Acknowledgement

## References

[1] Edwards GA, Stiller K, Dunlop GL, Couper MJ. Acta Mater 1998;46:3893.
[2] Andersen SJ, Zandbergen HW, Jansen J, Træholt C, Tundal U, Reiso O. Acta Mater 1998;46:3283.
[3] Hasting HS, Frøseth AG, Andersen SJ, Vissers R, Walmsley JC, Marioara CD, Danoix F, Lefebvre W, Holmestad R. J Appl Phys 2009;106:123527.
[4] Marioara CD, Andersen SJ, Zandbergen HW, Holmestad R. Metall Mater Trans A 2005;36:691.
[5] Marioara CD, Nordmark H, Andersen SJ, Zandbergen HW, Holmestad R. J Mater Sci 2006;41:471.
[6] Vissers R, van Huis MA, Jansen J, Zandbergen HW, Marioara CD, Andersen SJ. Acta Mater 2007;55:3815.
[7] Andersen SJ, Marioara CD, Vissers R, Frseth A, Zandbergen HW. Mater Sci Eng A 2007;444:157.
[8] Andersen SJ, Marioara CD, Frseth A, Vissers R, Zandbergen HW. Mater Sci Eng A 2005;2005:127.
[9] Zandbergen HW, Andersen SJ, Jansen JE. Science 1997;277:1221.
[10] Matsuda K, Sakaguchi Y, Miyata Y, Uetani Y, Sato T, Kamio A, Ikeno S. J Mater Sci 2000;35:179.
[11] Derlet PM, Andersen SJ, Marioara CD, Frøseth A. J Phys Cond Matter 2002;14:4011.
[12] Pogatscher S, Antrekowitsch H, Leiner H, Sologubenko AS, Uggowitzer AS. Scr Mater 2013;68:158.
[13] Sha G, Möller H, Stumpf WE, Xia JH, Govender G, Ringer SP, Acta Mater 2012;60:692.
[14] Ehlers FJH, Comput Mater Sci 2014;81:617.
[15] Ninive PH, Strandlie A, Gulbrandsen-Dahl S, Lefebvre W, Marioara CD, Andersen SJ, Friis J, Holmestad R, Løvvik OM. Acta Mater 2014;69:126.
[16] Saito T, Wenner S, Osmundsen E, Marioara CD, Andersen SJ, Røyset J, Lefebvre W, Holmestad R., Philos Mag Accepted 2014 DOI:10.1080/14786435.2014.913819
[17] Pennycook SJ, Jesson DE. Phys Rev Lett 1990;64:938.
[18] Pennycook SJ. Adv Imag Elect Phys 2000;103:147.
[19] van Aert S, de Backer A, Martinez GT, Goris B, Bals S, van Tendeloo G. Phys Rev B 2013;87:064107.
[20] de Backer A, Martinez GT, Rosenauer A, van Aert S. Ultramicroscopy 2013;134:22.
[21] Koch CT. PhD. Thesis. Determination of core structure periodicity and point defect density along dislocations. Arizona State University, 2002.
[22] Gao HX, Peng LM. Acta Cryst A 1999;55:926.
[23] Hohenberg P, Kohn W. Phys Rev B 1964;136:864.

11

[24] Kohn W, Sham LJ. Phys Rev A 1965;140:1133.

[25] Vanderbilt D, Phys. Rev B 1985;32;8412.

[26] Kresse G, Hafner J, Phys Rev B 1993;47:558.

[27] Kresse G, Furthmüller J, Comput Mater Sci 1996;6:15.

[28] Perdew JP, Chevary JA, Vosko SH, Jackson KA, Pederson MR, Singh DJ, Fiolhais C. Phys Rev B 1992;46:6671.

[29] Monkhorst HJ, Pack JD. Phys Rev B 1976;13:5188.

[30] van Helvoort ATJ, Dahl Ø, Soleim BG, Holmestad R, Tybell T. Appl Phys Lett 2005;86:092907.

[31] Nellist PD, Pennycook SJ, Ultramicroscopy 1999;78:111.

[32] van Aert S, Batenburg KJ, Rossell MD, Erni R, van Tendeloo G. Nature 2011;470:374.

[33] Ehlers FJH, Dumoulin S, Marthinsen K, Holmestad R. Model Simul Mater Sci Eng 2013;21: 085018.

[34] Haruta M, Kurata H, Komatsu H, Shimakawa Y, Isoda S. Ultramicroscopy 2009;109:361.

[35] Findlay SD, LeBeau JM, Ultramicroscopy 2013;124:52.

[36] Glas F. Phys Rev B 1995;51:825.

# Part III

# Concluding remarks

# Chapter 5

# Conclusions and outlook

Effects of Cu and Zn as trace elements on precipitation in Al-Mg-Si alloys are investigated and discussed mainly by TEM techniques, including advanced aberration-corrected STEM. In addition, effects of quench rate and pre-deformation are also investigated in connection to the investigation of the effect of Cu as a trace element. The structure of the Zn-containing $\beta''$ phase in the Al-Mg-Si alloy is also investigated. In this chapter, conclusions from the investigations and outlook for the thesis work are described.

## 5.1 Effect of trace elements

In Paper I, the effect of Cu as a trace element on precipitate microstructure is systematically investigated with different additions of Cu (0.001 wt%, 0.01 wt% and 0.1 wt%) in an Al-Mg-Si alloy. In addition to the effect of Cu, effects of slow quench rate after solution heat treatment and 1% pre-deformation are also investigated. In Paper II, following Paper I, the effect of Cu addition (0.1 wt%) on precipitate structures is investigated by aberration uncorrected HAADF-STEM. In Paper III, the precipitate structures are further investigated by aberration-corrected HAADF-STEM. In Paper IV, the effect of Zn is systematically investigated with different additions of Zn (0.000 wt%, 0.001 wt%, 0.01 wt%, 0.1 wt% and 1 wt%). The following is a description of conclusions and outlook.

### 5.1.1 Cu

An addition of Cu ~0.4 wt% in Al-Mg-Si alloys is known to increase strength [63–65], enhance precipitation kinetics [65, 67], make the precipitate microstructure fine [66, 67] and alter the precipitation sequence [69, 70]. However, in the case of low additions (< 0.1 wt%) as a trace element, this will depend on the Cu level.

133

A Cu content of below 0.01 wt% has negligible influence on the hardness. Also, precipitation kinetics is not influenced by Cu additions of 0.01 wt% and below. These conclusions are also valid for alloys with slow quench rate and 1 wt% pre-deformation.

An addition of 0.1 wt% Cu makes precipitate free zones narrower. It is known that slow cooling makes precipitate free zones wider, leading to lower strength. Cu additions can in this way potentially compensate the negative effects of slow cooling.

An addition of 0.1 wt% Cu also leads to higher hardness corresponding to higher number density of shorter precipitates. Precipitation kinetics is also faster. The precipitation sequence in the Al-Mg-Si system does not alter. However, the addition of 0.1 wt% Cu makes precipitates with partially disordered structure. Cu atomic columns are observed only in the disordered part of the precipitates. In addition, the disordered part of the structure consists of specific atomic configurations around the Cu atomic columns. The atomic configurations of Cu can be divided into two types, depending on the Si-network: the Cu atomic columns are 1. *in-between* the Si-network columns and 2: *on* the Si-network columns. It is revealed that the former configuration has the same atomic coordination around the Cu atomic columns as in *fragments* of the C and Q' phases in the Cu-containing (~0.4 wt%) Al-Mg-Si system. Moreover, the latter is the same as for Ag columns in the $\beta'_{Ag}$ phase. In addition, a whole disordered part consists of the Si-network regardless of Cu atomic columns. Fragments of the U2 phase are consisted of the disordered part without Cu atomic columns. These observation are made also for the 10% pre-deformed alloys which in addition show the string-type and B'/Q' precipitates heterogeneously nucleated along dislocation lines. It is concluded that a 0.1 wt% Cu addition makes the precipitates partially disordered, but that the structure consists of *fragments* of "known" metastable precipitate phases in the Al-Mg-Si system and consequently of the Si-network.

The atomic configurations around Cu atomic columns based on the Si-network seem to be energetically favourable, even when the structure is *disordered*. It is plausible that the fragments form during nucleation, and Cu atoms *seek* to be surrounded by Si atoms. This could make clusters more potent, as a higher number density of precipitates is observed in the 0.1 wt% Cu added alloys. As a prospective future work, DFT calculations could support the hypothesis of an energetical preference of Cu atoms in the fragments. In addition, the role of the Si-network for stabilizing the atomic configurations could be revealed.

### 5.1.2   Zn

Zn additions of 0.1 wt% and below do not have a measurable influence on strength, microstructure and corrosion properties. On the other hand, a Zn addition of 1wt% makes hardness slightly higher and conductivity lower during precipitation. The higher hardness is associated with a slightly higher number density with shorter precipitates. Some Zn atoms are still in solid solution which can be drawn by the observation of lower conductivity at the peak hardness condition.

Zn atoms diffuse into grain boundaries during precipitation to make a *Zn film*. This leads to high susceptibility of IGC properties. The effect is more pronounced for peak hardness and over-aged conditions than for under-aged conditions. These observations are made only in an addition of 1 wt% Zn. Additions of 0.1 wt% Zn and below leads to low susceptibility of IGC properties.

Zn is known as the main alloying elements in Al-Zn-Mg alloys (7xxx series) having different types of precipitates from Al-Mg-Si alloys, but no precipitate types in the Al-Zn-Mg system have been observed in the Zn added Al-Mg-Si alloy. Instead, most precipitates have a disordered structures – lacking a unit cell periodicity, but consisting of the Si-network. The disordered structure consists of specific atomic configurations around the Zn atomic columns which is in-between the Si-network or on the Si-network. These observation are analogous to the disordered structures found around Cu atomic columns. However, in Zn case, Zn atomic columns have a weaker preference for the sites they occupy: these are the Ag and Al sites in the $\beta'_{Ag}$ phase, the Cu sites in the C and Q' phases and the Al and Si sites in the U2 phase. It has been concluded that Zn has a weak interaction with these sites.

In the Al-Zn-Mg system, Zn atoms combine with Mg to form the plate-like semi-coherent $\eta'$ metastable precipitates and equilibrium $\eta$-MgZn$_2$ precipitates on {111} Al planes [92–94]. These precipitates do not form when 1 wt% Zn is added to Al-Mg-Si alloys. Since Si atoms play a key role in stabilizing the Si-network (presented in even disordered structures), it should be possible to find an optimal compositions to *transit* formed precipitates either in the Al-Mg-Si system or in the Al-Zn-Mg system. For future prospective work, it could find the *transiting composition* for further microstructural modelling and understanding of precipitate growth mechanism. This can be done by optimizing compositions and heat treatment.

## 5.2   Zn-containing $\beta''$ phase

Although most precipitates are disordered in 1 wt% Zn added Al-Mg-Si alloys, perfect $\beta''$ precipitates can be observed in peak hardness condition. Analysis of

HAADF-STEM images shows that the Si3/Al site in the $\beta''$ phase is partially occupied by Zn. DFT calculations can support that the Si3/Al site is the preferential site for Zn incorporation. Calculations suggest that Zn atoms are not clustering, but that they have a weak interaction with other Zn atoms.

A certain amount of Zn atoms stay in solid solution. The estimation of Zn concentration in the solid solution enables occupancies of the partial Zn atoms in the Si3/Al site to be estimated. This would give more insight to the complicated processes of atomic diffusion and precipitate nucleation and growth. The concentrations could be estimated by APT.

# Appendix

# Appendix A

# Parameters of STEM simulations

As described in section 3.7 and in Paper V, STEM image simulations have been conducted using the multislice frozen phonon simulations provided by QSTEM software package [148]. The simulations have been conducted by a primitive cell of the $\beta''$ phase shown in Figure A.1 (i). The structure and the atomic positions are provided in Tables 2-2 and 2-3. Figure A.1 (ii) shows an example of simulated image for the primitive unit cell of the $\beta''$ phase. Numerical parameters of the STEM simulations used in Paper V are shown in Table A.1. The microscope parameters are the same as in the experiment in Paper V. The slice thickness is chosen to be half a unit cell. The chosen Debye-Waller factors for each site match those of the elemental phases at 300K [169]. The geometrical aberrations are chosen to be zero. Hence, the probe width is derived by the diffraction limit. The $\beta''$ phase has a monoclinic unit cell while scan area can be chosen as rectangle area. Hence, the scan area is chosen so that it covers the primitive cell. The pixel size of the scan area is chosen by the criteria described in [170].
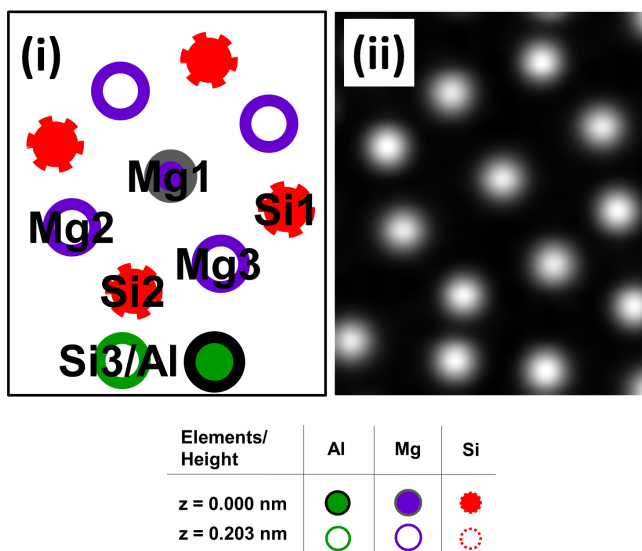
Figure A.1: (i) A primitive cell of the $\beta''$ phase and (ii) an example of simulated image. The composition of the $\beta''$ phase is assumed to be $Mg_5Al_2Si_4$. In (ii), the image is shown with oversampling for a presentation purpose.

Table A.1: Parameters of STEM simulations used for the $\beta''$ phase in Paper V.

| | |
|---|---|
| Acceleration voltage | 200 kV |
| Slice thickness | 0.205 nm |
| Convergence semi angle | 20 mrad |
| HAADF detector collection angle | 45 – 150 mrad |
| Debye-Waller factors | Mg: 1.8837 Å$^2$<br>Al: 0.8334 Å$^2$<br>Si: 0.5261 Å$^2$<br>Zn: 1.1782 Å$^2$ |
| Temperature | 300 K |
| Number of phonon configurations | 30 |
| Probe array | $400 \times 400$ pixels |
| Resolution | $0.0375 \times 0.0375$ Å |
| Defocus spread | 0.015 nm |
| Probe width | 0.077 nm |
| Dimension of scan area | $7.25 \times 9$ Å$^2$ |
| Pixel size of scan area | $48 \times 58$ pixels |

# References

[1] G. E. Totten and D. S. MacKenzie. *Handbook of Aluminum*. Marcel Dekker, Inc., 2003.

[2] J. A. S. Green. *Aluminum recycling and processing for energy conservation and sustainability*. ASM International, 2007.

[3] M. E. Schlesinger. *Aluminum recycling: second edition*. CRC Press, 2014.

[4] D. B. Williams and C. B. Carter. *Transmission electron microscopy: A text book for materials science, second edition*. Springer, 2009.

[5] P. D. Nellist and S. J. Pennycook. The principles and interpretation of annular dark-field Z-contrast imaging. *Adv. Imag. Elect. Phys.*, 113:147–203, 2000.

[6] F. Wöhler. Über das Aluminium. *Annalen der Physik und Chemie*, 11:146–161, 1827.

[7] I. J. Polmear. *Light Alloys*. Elsevier, 2005.

[8] Joseph R. Davis. *Aluminum and Aluminum Alloys*. ASM International, 1993.

[9] J. D. Embury. Strength mechanisms in Al alloys - An overview of natural limits and engineering possibilities. *Mater. Sci. Forum*, 217-222:57–70, 1996.

[10] E. O. Hall. The deformation and ageing of mild steel: III Discussion of results. *Proc. Phys. Soc. B*, 64:747–753, 1951.

[11] N. J. Petch. The cleavage strength of polycrystals. *J. Iron Steel Inst.*, 147:25–28, 1953.

[12] A. Deschamps, L. Le Sinq, Y. Bréchet, J. D. Embury, and M. Niewczas. Anomalous strain hardening behaviour of a supersaturated Al-Zn-Mg alloy. *Mater. Sci. Eng., A*, 234-236:477–480, 1997.

[13] R. Bullough and J. R. Hardy. The strain field interaction between vacancies in copper and aluminum. *Philos. Mag.*, 17:833–842, 1968.

[14] P. T. Heald. The preferential trapping of interstitials at dislocations. *Philos. Mag.*, 31:551–558, 1975.

[15] R. Maddin and A. H. Cottrell. Quanch hardening in aluminum single crystals. *Philos. Mag.*, 46:735–743, 1955.

[16] J. D. Embury, D. J. Lloyd, and T. R. Ramachandran. Strstrengthe mechanisms in aluminum alloys. *Treatise on Materials Science & Technology*, 31:579–601, 1989.

[17] J. Friedel. *Dislocations in crystals*. Pergamon Press, 1964.

[18] F. R. N. Nabarro. *Theory of crystal dislocations*. Oxford, 1967.

[19] O. R. Myhr, Ø. Grong, and S. J. Andersen. Modeling of the age hardening behaviour of Al-Mg-Si alloys. *Acta Mater.*, 49:65–75, 2001.

[20] W. J. Poole, X. Wang, D. J. Lloyd, and J. D. Embury. The shearable-non-shearable transition in Al-Mg-Si-Cu precipitation hardening alloys: implications on the distribution of slip, work hardening and fracture. *Philos. Mag.*, 85:3113–3135, 2005.

[21] A. Guinier. Structure of age-hardening aluminum-copper alloys. *Nature*, 142:569–570, 1938.

[22] G. D. Preston. The diffraction of X-rays by an age-hardening alloy of aluminum and copper. *Philos. Mag.*, 26:855–871, 1938.

[23] J. D. Verhoeven. *Fundamentals of Physical Metallurgy*. Wiley, 1975.

[24] E. Orowan. Discussion on internal stresses. *The Institute of Metals, London*, Symposium on internal stresses in metals and alloys:451–453, 1948.

[25] A. Bahrami, A. Miroux, and J. Sietsma. An age-hardening model for Al-Mg-Si alloys considering needle-shaped precipitates. *Metall. Mater. Trans. A*, 43:4445–4453, 2012.

[26] D. A Porter, K. E. Easterling, and M. Sherif. *Phase Transformations in Metals and Alloys, Third Edition*. CRC Press, 2009.

[27] H. I. Aaronson, M. Enomoto, and J. K. Lee. *Mechanisms of Diffusional Phase Transformations in Metals and Alloys*. CRC Press, 2010.

[28] Y. Du, Y. A. Chang, B. Huang, W. Gong, J. Zhanpeng, X. Honghui, Z. Yuan, Y. Liu, Y. He, and F.-Y. Xie. Diffusion coefficients of some ssolute in fcc and liquid Al: critical evaluation and correlation. *Mater. Sci. Eng. A*, 363:140–151, 2003.

[29] M. Mantina, Y. Wang, L. Q. Chen, Z. K. Liu, and C. Wolverton. First principles impurity diffusion coefficients. *Acta Mater.*, 57:4102–4108, 2009.

[30] L. F. Mondolfo. *Aluminum Alloys: Structure and Properties*. Butterworth, 1976.

[31] L. Lodgaard and N. Ryum. Precipitation of dispersoids containing Mn and/or Cr in Al-Mg-Si alloys. *Mater. Sci. Eng., A*, 283:144–152, 2000.

[32] K. Matsuda, H. Gamada, K. Fujii, Y. Uetani, T. Sato, A. Kamio, and S. Ikeno. High-resolution electron microscopy on the strcuture of Guinier-Preston zones in an Al-1.6 mass pct $Mg_2Si$ alloy. *Metall. Mater. Trans. A*, 29A:1161–1167, 1998.

[33] C. D. Marioara, S. J. Andersen, J. Jansen, and H. W. Zandbergen. Atomic model for GP-zones in a 6082 Al-Mg-Si system. *Acta Mater.*, 49:321–328, 2001.

[34] G. A. Edwards, K. Stiller, G. L. Dunlop, and M. J. Couper. The precipitation sequence in Al-Mg-Si alloys. *Acta Mater.*, 46:3893–3904, 1998.

[35] M. Murayama and K. Hono. Pre-precipitate clusters and precipitation processes in Al-Mg-Si alloys. *Acta Mater.*, 47:1537–1548, 1999.

[36] J. H. Chen, E. Costan, M. A. van Huis, and H. W. Zandbergen. Atomic pillar-based nanoprecipitates strengthen AlMgSi alloys. *Science*, 312:416–419, 2006.

[37] H. W. Zandbergen, S. J. Andersen, and J. Jansen. Structure determination of $Mg_5Si_6$ particles in Al by dynamic electron diffraction studies. *Science*, 277:1221–1225, 1997.

[38] S. J. Andersen, H. W. Zandbergen, J. Jansen, C. Træholt, U. Tundal, and O. Reiso. The crystal structure of the $\beta''$ phase in Al-Mg-Si alloys. *Acta Mater.*, 46:3283–3298, 1998.

[39] H. S. Hasting, Anders G. Frøseth, S. J. Andersen, Rene Vissers, J. C. Walmsley, Calin D. Marioara, Frédéric Danoix, Williams Lefebvre, and Randi Holmestad. Composition of $\beta''$ precipitates in Al-Mg-Si alloys by atom probe tomography and first principles calculations. *J. Appl. Phys.*, 106:123527–9, 2009.

[40] S. Pogatscher, H. Antrekowitsch, H. Leiner, A. S. Sologubenko, and P. J. Uggowitzer. Influence of the thermal route on the peak-aged microstructures in an Al-Mg-Si aluminum alloy. *Scr. Mater.*, 68:158–161, 2013.

[41] F. J. H. Ehlers. Ab initio interface configuration determination for $\beta''$ in Al-Mg-Si: Beyond the constraint of a preserved precipitate stoichiometry. *Comput. Mater. Sci.*, 81:617–629, 2014.

[42] G. Sha, H. Möller, W. E. Stumpf, J. H. Xia, G. Govender, and S. P. Ringer. Solute nanostructures and their strengthening effects in Al-7Si-0.6Mg alloy F357. *Acta Mater.*, 60:692–701, 2012.

[43] P. H. Ninive, A. Strandlie, S. Gulbrandsen-Dahl, W. Lefebvre, C. D. Marioara, S. J. Andersen, J. Friis, R. Holmestad, and O. M. Løvvik. Detailed atomic insight into the $\beta''$ phase in Al-Mg-Si alloys. *Acta Mater.*, 69:126–134, 2014.

[44] C. Cayron and P. A. Buffat. Transmission electron microscopy study of the $\beta'$ phase (Al-Mg-Si alloys) and qc phase (Al-Cu-Mg-Si alloys): Ordering mechanism and crystallographic structure. *Acta Mater.*, 48:2639–2653, 2000.

[45] K. Matsuda, Y. Sakaguchi, Y. Miyata, Y. Uetani, T. Sato, A. Kamio, and S. Ikeno. Precipitation sequence of various kinds of metastable phase in Al-1.0mass%Mg$_2$Si-0.4mass%si alloy. *J. Mater. Sci.*, 35:179–189, 2000.

[46] R. Vissers, M. A. van Huis, J. Jansen, H. W. Zandbergen, C. D. Marioara, and S. J. Andersen. The crystal structure of the $\beta'$ phase in Al-Mg-Si alloys. *Acta Mater.*, 55:3815–3823, 2007.

[47] S. J. Andersen, C. D. Marioara, R. Vissers, A. G. Frøseth, and H. W. Zandbergen. The structural relation between precipitates in Al-Mg-Si alloys, the Al-matrix and diamond silicon, with emphasis on the trigonal phase U1-MgAl$_2$Si$_2$. *Mater. Sci. Eng., A*, 444:157–169, 2007.

[48] A. G. Frøseth, R. Høier, P. M. Derlet, S. J. Andersen, and C. D. Marioara. Bonding in MgSi and Al-Mg-Si compounds relevant to Al-Mg-Si alloys. *Phys. Rev. B: Condens. Matter Mater. Phys.*, 67:224106–11, 2003.

[49] K. Matsuda, S. Tada, S. Ikeno, T. Sato, and A. Kamio. Crystal system of rod-shaped precipitatesin an Al-1.0mass%$Mg_2$Si-0.4mass%Si alloy. *Scripta Metallurgica et Materialia*, 32:1175–1180, 1995.

[50] S. J. Andersen, C. D. Marioara, A. G. Frøseth, R. Vissers, and H. W. Zandbergen. Crystal structure of the orthorhombic U2-$Al_4Mg_4Si_4$. *Mater. Sci. Eng. A*, 390:127–138, 2005.

[51] K. Matsuda, S. Ikeno, T. Sato, and A. Kamio. A metastable phase having the orthorhombic crystal lattice in an Al-1.0mass%$Mg_2$Si-0.4mass%si alloy. *Scr. Mater.*, 34:1797–1802, 1996.

[52] C. D. Marioara, H. Nordmark, S. J. Andersen, and R. Holmestad. Post-$\beta''$ phase and their influence on microstructure and hardness in 6xxx Al-Mg-Si alloys. *J. Mater. Sci.*, 41:471–478, 2006.

[53] S. D. Dumolt, D. E. Laughlin, and Williams J. C. Formation of a modified $\beta'$ phase in aluminum alloy 6061. *Scr. Metall.*, 18:1347–1350, 1984.

[54] R. Vissers, C. D. Marioara, S. J. Andersen, and R. Holmestad. Crystal structure determination of the B' phase in Al-Mg-Si alloys by combining quantitative electron diffraction and Ab initio calculations. *Proceedings of ICAA11*, Vol. 2, Aachen Germany, ISBN 9978-3-527-32367-8:1263–1269, 2008.

[55] C. D. Marioara, S. J. Andersen, H. W. Zandbergen, and R. Holmestad. The influence of alloy composition on precipitates of the Al-Mg-Si system. *Metall. Mater. Trans. A*, 36:691–702, 2005.

[56] J. Banhart, M. D. H. Lay, C. S. T. Chang, and A. J. Hill. Kinetics of natural aging in Al-Mg-Si alloys studied by positron annihilation lifetime spectroscopy. *Phys. Rev. B*, 83:014101, 2011.

[57] M. Murayama, K. Hono, M. Saga, and M. Kikuchi. Atom probe studies on the early sstage of precipitation in Al-Mg-Si alloys. *Mater. Sci. Eng. A*, 250:127–132, 1998.

[58] A. Serizawa, S. Hirosawa, and T. Sato. Three-demensional atom probe characterization of nanoclusters responsible for multistep aging behaviour of an Al-Mg-Si alloy. *Metall. Mater. Trans. A*, 39:243–251, 2008.

[59] M. Torsæter, H. S. Hasting, W. Lefebvre, C. D. Marioara, J. C. Walmsley, S. J. Andersen, and R. Holmestad. The influence of composition and natural aging on clustering during preaging in Al-Mg-Si alloys. *J. Appl. Phys.*, 108:073527, 2010.

[60] F. A. Martinsen, F. J. H. Ehlers, M Torsæter, and R. Holmestad. Reversal of the negative natural aging effect in Al-Mg-Si alloys. *Acta Mater.*, 60:6091–6101, 2012.

[61] J. Røyset, T. Stene, J. A. Sæter, and O. Reiso. The effect of intermediate storage temperature and time on the age hardening response of Al-Mg-Si alloys. *Mater. Sci. Forum*, 519-521:239–244, 2006.

[62] T. Sato, S. Hirosawa, K. Hirose, and T. Maeguchi. Roles of microalloying elements on the cluster formation in the initial stage of phase decomposition of Al-based alloys. *Metall. Mater. Trans. A*, 34:2745–2755, 2003.

[63] D. K. Chatterjee and K. M. Entwistle. A study of the effect of magnesium loss and of the addition of copper on the ageing of aluminum-magnesium-silicon alloys. *J. Inst. Met.*, 101:53–59, 1973.

[64] H. Suzuki, M. Kanno, Y. Shiraishi, and K. Hanawa. Effect of Cu addition on aging phenomena in Al-Mg-Si alloys. *J. J. I. L. M.*, 29:575–581, 1979.

[65] R. J. Livak. Effect of copper and chromium on the aging response of dilute Al-Mg-Si alloys. *Metall. Trans. A*, 13:1318–1321, 1982.

[66] W. F. Miao and D. E. Laughlin. Effect of Cu content and preaging on precipitation characteristics in aluminum alloy 6022. *Metall. Mater. Trans. A*, 31:361–371, 2000.

[67] M. Murayama, K. Hono, W. F. Miao, and D. E. Laughlin. The effect of Cu additions on the precipitation kinetics in an Al-Mg-Si alloy with excess Si. *Metall. Mater. Trans. A*, 32:239–246, 2001.

[68] V. Massardier and T. Epicier. Study of the influence of a low copper addition and of an excess of silicon on the precipitation kinetics ad on the precipitation sequence of Al-$Mg_2$Si alloys. *Mater. Sci. Forum*, 369-402:851–856, 2002.

[69] D. J. Chakrabarti and D. E. Laughlin. Phase relation and precipitation in Al-Mg-Si alloys with Cu additions. *Progress in Materials Science*, 49:389–410, 2004.

[70] C. D. Marioara, S. J. Andersen, T. N. Stene, H. S. Hasting, J. C. Walmsley, A. T. J. Van Helvoort, and R. Holmestad. The effect of Cu on precipitation in Al-Mg-Si alloys. *Philos. Mag.*, 87:3385–3413, 2007.

[71] M. Torsæter, F. J. H. Ehlers, C. D. Marioara, S. J. Andersen, and R. Holmestad. Applying precipitate-host lattice coherency for compositional determination of precipitates in Al-Mg-Si-Cu alloys. *Philos. Mag.*, 92:3833–3856, 2012.

[72] M. Torsæter, W. Lefebvre, C. D. Marioara, S. J. Andersen, J. C. Walmsley, and R. Holmestad. Study of intergrown L and Q' precipitates in Al-Mg-Si alloys. *Scr. Mater.*, 64:817–820, 2011.

[73] C. D. Marioara, S. J. Andersen, J. Røyset, O. Reiso, S. Gulbrandsen-Dahl, T. E. Nicolaisen, I. E. Opheim, J. F. Helgaker, and R. Holmestad. Improving thermal stability in cu-containing Al-Mg-Si alloys by precipitate optimization. *Metall. Mater. Trans. A*, In press:DOI: 10.1007/s11661–014–2250–0, 2014.

[74] C. Cayron, L. Sagalowicz, O. Beffort, and P. A. Buffat. Structural phase transition in Al-Cu-Mg-Si alloys by transmission electron microscopy study on an Al-4wt%Cu-1wt%Mg-Ag alloy reinforced by SiC particles. *Philos. Mag. A*, 79:2833–2851, 1999.

[75] K. Matsuda, Y. Uetani, T. Sato, and S. Ikeno. Metastable phase in an Al-Mg-Si alloy containing copper. *Metall. Mater. Trans. A*, 32:1293–1299, 2001.

[76] M Torsæter, R. Vissers, C. D. Marioara, S. J. Andersen, and R. Holmestad. Simulation and modelling: Cry structure determination of the Q' and C-type plate precipitates in Al-Mg-Si-Cu (6xxx) alloys. *Proceedings of ICAA11*, Vol. 2, Aachen Germany, ISBN 9978-3-527-32367-8:1263–1268, 2008.

[77] Y. Baba and A. Takashima. Effects of composition on the two-step ageing of Al-Mg-Si alloys. *J. J. I. L. M.*, 19:90–98, 1969.

[78] K. Matsuda, K. Kido, T. Kawabata, Y. Uetani, and S. Ikeno. Effects of Cu, Ag and Au addition on total elongation and fracture morphology in Al-Mg-Si alloys. *J. J. I. L. M.*, 53:528–533, 2003.

[79] J. Nakamura, K. Matsuda, T. Kawabata, T. Sato, Y. Nakamura, and S. Ikeno. Effect of silver addition on the $\beta$'-phase in Al-Mg-Si alloy. *Mater. Trans.*, 51:310–316, 2010.

[80] C. D. Marioara, J. Nakamura, K. Matsuda, S. J. Andersen, R. Holmestad, T. Sato, T. Kawabata, and S. Ikeno. HAADF-STEM study of $\beta$'-type precipitates in an over-aged Al-Mg-Si-Ag alloy. *Philos. Mag.*, 92:1149–1158, 2012.

[81] J. Kim, C. D. Marioara, R. Holmestad, E. Kobayashi, and T. Sato. Effects of Cu and Ag additions on age-hardening behaviour during multi-step aging in Al-Mg-Si alloys. *Mater. Sci. Eng., A*, 560:154–162, 2013.

[82] S. Wenner, C. D. Marioara, Q. M. Ramasse, D. Kepaptsoglou, F. S. Hage, and R. Holmestad. Atomic-resolution electron energy loss studies of precipitates in an Al-Mg-Si-Cu-Ag alloy. *Scr. Mater.*, 74:92–95, 2014.

[83] A. Lutts. Pre-precipitation in Al-Mg-Ge and in Al-Mg-Si. *Acta Metall.*, 9:577–586, 1961.

[84] S. Ceresara and P. Fiorini. Clustering in Al-Mg-Ge alloy. *Mater. Sci. Eng.*, 3:170–174, 1968.

[85] K. Matsuda, S. Ikeno, and T. Munekata. HRTEM study of precipitates in Al-Mg-Si and Al-Mg-Ge. *Mater. Sci. Forum*, 519-521:221–226, 2006.

[86] K. Matsuda, T. Munekata, and S. Ikeno. Effect of Mg content on the precipitation in Al-Mg-Ge alloys. *Mater. Sci. Forum*, 561-565:2049–2052, 2007.

[87] R. Bjørge, C. D. Marioara, S. J. Andersen, and R. Holmestad. Precipitation in two Al-Mg-Ge alloys. *Metall. Mater. Trans. A*, 41:1907–1916, 2010.

[88] R. Bjørge, P. N. H. Nakashima, C. D. Marioara, S. J. Andersen, B. C. Muddle, J. Etheridge, and R. Holmestad. Precipitates in an Al-Mg-Si alloy studied by aberration-corrected scanning transmission electron microscopy. *Acta Mater.*, 59:6103–6109, 2011.

[89] R. Bjørge, C. Dwyer, M. Weyland, P. N. H. Nakashima, C. D. Marioara, S. J. Andersen, J. Etheridge, and R. Holmestad. Aberration-corrected scanning transmission electron microscopy study of $\beta$' like-precipitates in an Al-Mg-Si alloy. *Acta Mater.*, 60:3239–3246, 2012.

[90] R. Bjørge, S. J. Andersen, C. D. Marioara, J. Etheridge, and R. Holmestad. Scanning transmission electron microcopy investigation of an Al-Mg-Si-Ge-Cu alloy. *Philos. Mag.*, 92:3983–3993, 2012.

[91] S. Wenner, C. D. Marioara, S. J. Andersen, and R. Holmestad. How calcium prevents precipitation hardening in Al-Mg-Si alloys. *Mater. Sci. Eng., A*, 575:241–247, 2013.

[92] L. K. Berg, J. Gjønnes, V. Hansen, X. Z. Li, M. Knutson-Wedel, G. Waterloo, D. Schryvers, and L. R. Wallenberg. GP-zones in Al-Zn-Mg alloys and their role in artificial aging. *Acta Mater.*, 49:3443–3451, 2001.

[93] G. Sha and A. Cerezo. Early-stage precipitation in Al-Zn-Mg-Cu alloy (7050). *Acta Mater.*, 52:4503–4516, 2004.

[94] C. D. Marioara, W. Lefebvre, S. J. Andersen, and J. Friis. Atomic structure of hardening precipitates in an Al-Mg-Zn-Cu alloy determined by HAADF-STEM and first principles calculations: relation to $\eta$-MgZn. *J. Mater. Sci.*, 48:3638–3651, 2013.

[95] T. Saito, C. D. Marioara, S. J. Andersen, W. Lefebvre, and R. Holmestad. Aberration-corrected HAADF-STEM investigations of precipitate structures in Al-Mg-Si alloys with low Cu additions. *Philos. Mag.*, 94:520–531, 2013.

[96] T. Saito, S. Wenner, E. Osmundsen, C. D. Marioara, S. J. Andersen, J. Røyset, W. Lefebvre, and R. Holmestad. The effect of Zn on precipitation in Al-Mg-Si alloys. *Philos. Mag.*, In press:DOI: 10.1080/14786435.2014.913819, 2014.

[97] M. H. Jacobs. The structure of the metastable precipitates formed during ageing of an Al-Mg-Si alloy. *Philos. Mag.*, 26:1–13, 1972.

[98] L. Arnberg and B. Aurivillius. The crystal structure of $Al_xCu_2Mg_{12-x}Si_7$, (*h*-AlCuMgSi). *Acta Chem. Scand. A*, 34:1–5, 1980.

[99] L. A. Girifalco and H. Herman. A model for the growth of Guinier-Preston zones the vacancy pump. *Acta Metall.*, 13:583–590, 1965.

[100] S. Hirosawa, T. Sato, J. Yokota, and A. Kamio. Comparison between resistivity changes and Monte Carlo simulation for GP-zone formation in Al-Cu base ternary alloys. *Mater. Trans., JIM*, 39:139–146, 1998.

[101] H. S. Zurob and H. Seyedrezai. A model for the growth of solute clusters based on vacancy trapping. *Scr. Mater.*, 61:141–144, 2009.

[102] S. Pogatscher, H. Antrekowitsch, H. Leiner, T. Ebner, and P. J. Uggowitzer. Mechanisms controlling the artificial aging of Al-Mg-Si alloys. *Acta Mater.*, 59:3352–3363, 2011.

[103] J. W. Evancho and J. T. Staley. Kinetics of precipitation in aluminum alloys during continuous cooling. *Metall. Trans.*, 5:43–47, 1974.

[104] K. Strobel, M. A. Easton, L. Sweet, and N. C. Parson. The effect of natural aging on quench sensitivity in Al-Mg-Si alloys. *Proceedings of ICAA13*, Pittsburgh Pennsylvania USA, ISBN 978-1-118-45804-4:1187–1192, 2012.

[105] J. L. Cavazos and R. Colás. Quench sensitivity of a heat treatable aluminum alloy. *Mater. Sci. Eng. A*, 363:171–178, 2003.

[106] H. J. Rack. The influence of prior strain upon precipitation in high-purity 6061 aluminum alloy. *Mater. Sci. Eng.*, 29:179–188, 1977.

[107] H. L. Lee, W. H. Lu, and S. L. Chan. Effect of cold rolling on the aging kinetics of $Al_2O_3$/6061 Al composite by differential scanning calorimetric technique. *Scripta Metall. Mater.*, 25:2165–2170, 1991.

[108] K. Matsuda, H. Gamada, Y. Uetani, S. Rengakuji, F. Shinagawa, and S. Ikeno. Specific precipitates in Al-$Mg_2$Si alloys aged after deformation. *J. J. I. L. M.*, 48:471–475, 1998.

[109] K. Matsuda, S. Shimizu, H. Gamada, Y. Uetani, F. Shinagawa, and S. Ikeno. Effect of deformation on the precipitates in Al-$Mg_2$Si alloys containing silicon in excess. *J. Soc. Mater. Sci. Jpn.*, 49:10–15, 1999.

[110] K. Teichmann, C. D. Marioara, S. J. Andersen, K. O. Pedersen, S. Gulbrandsen-Dahl, M. Kolar, R. Holmestad, and K. Marthinsen. HRTEM study of the effect of deformation on the early precipitation behaviour in an AA6060 Al-Mg-Si alloy. *Philos. Mag.*, 91:3744–3754, 2011.

[111] K. Teichmann, C. D. Marioara, S. J. Andersen, and K. Marthinsen. The effect of preaging deformation on the precipitation behaviour of an Al-Mg-Si alloy. *Metall. Mater. Trans. A*, 43:4006–4014, 2012.

[112] R. S. Yassar, D. P. Field, and H. Weiland. The effect of predeformation on the $\beta$" and $\beta$' precipitates and the role of Q' phase in an Al-Mg-Si alloy; AA6022. *Scripta Materialia*, 53:299–303, 2005.

[113] R. S. Yassar, D. P. Field, and H. Weiland. The effect of cold deformation on the kinetics of the $\beta$" precipitates in an Al-Mg-Si alloy. *Metall. Mater. Trans. A*, 36:2059–2065, 2005.

[114] G. K. Quainoo and S. Yannacopoulos. The effect of cold work on the precipitation kinetics of AA6111 aluminum. *J. Mater. Sci.*, 39:6495–6502, 2004.

[115] Y. Birol. Pre-straining to improve the bake hardening response of a twin-roll cast Al-Mg-Si alloy. *Scr. Mater.*, 52:169–173, 2005.

[116] Y. Birol and M. Karlik. The interaction of natural ageing with straining in a twin-roll cast AlMgSi automotive sheet. *Scr. Mater.*, 55:625–628, 2006.

[117] K. Matsuda, Y. Takaki, T. Sakurai, and S. Hirosawa. Combined effect of pre-straining and pre-aging on bake-hardening behaviour of an Al-0.6mass%Mg-1.0mass%Si alloy. *Mater. Trans.*, 51:325–332, 2010.

[118] A. Serizawa, T. Sato, and M. K. Miller. Effect of cold rollng on the formation and distribution of nanoclusters during pre-aging in an Al-Mg-Si alloy. *Mater. Sci. Eng. A*, 561:492–497, 2013.

[119] http://www.world aluminium.org/. Global aluminum recycling: A cornerstone of sustainable development. Technical report, International Aluminum Institute, 2009.

[120] K. Grjotheim and B. J. Welch. *Aluminum smelter technology*. Aluminum-Verlag, 1980.

[121] G. Liu, C. E. Bangs, and Müller. Stock dynamic and emission pathways of the global aluminum cycle. *Nature Clim. Change*, 3:338–342, 2013.

[122] G. Gaustad, E. Olivetti, and R. Kirchain. Improving aluminum recycling: A survey of sorting and impurity removal technologies. *Resour. Conserv. Recy.*, 58:79–87, 2012.

[123] A. N. Løvik, R. Modaresi, and D. B. Müller. Long-term strategies for increased recycling of automotive aluminum and its alloying elements. *Environ. Sci. Technol.*, In press:DOI: 10.1021/es405604g, 2014.

[124] G. Rombach. Limits of metal recycling. *Sustainable Metals Management*, 19:295–312, 2006.

[125] R. Modaresi and D. B. Müller. The role of automobiles for the future of aluminum recycling. *Environ. Sci. Technol.*, 46:8587–8594, 2012.

[126] A. Gesing and R. Wolanski. Recycling light metals from end-of-life vehicle. *JOM*, 53:21–23, 2001.

[127] J. I. Goldstein, D. E. Newbury, D. C. Joy, C. E. Lyman, P. Echlin, E. Lifshin, L. Sawyer, and J. R. Michael. *Scanning electron microscopy and X-ray microanalysis*. Springer, 2003.

[128] M. F. Chung and L. H. Jenkins. Auger electron energies of the outer shell electrons. *Surf. Sci.*, 22:479–485, 1970.

[129] J. F. Watts and J. Wolstenholme. *An introduction to surface analysis by XPS and AES*. Wiley, 2003.

[130] E. Rutherford. The scattering of $\alpha$ and $\beta$ particles by matter and the structure of the atom. *Philos. Mag.*, 21:669–688, 1911.

[131] C. Kittel. *Introduction to solid state physics*. Wiley, 2004.

[132] L. Reimer and H. Kohl. *Transmission Electron Microscopy*. Springer, 2008.

[133] R. Erni. *Aberration-corrected imaging in transmission electron microscopy*. Imperial College Press, 2010.

[134] E. J. Kirkland. *Advanced computing in electron microscopy: second edition*. Springer, 2010.

[135] Z. L. Wang. *Elastic and inelastic scattering in electron diffraction and imaging*. Plenum Press, 1995.

[136] D. van Dyck and A. F. de Jong. Ultimate resolution and information in electron microcopy: general principles. *Ultramicroscopy*, 47:266–281, 1992.

[137] A. F. de Jong and D. van Dyck. Ultimate resolution and information in electron microscopy II. The information limit of transmission electron microscopes. *Ultramicroscopy*, 49:66–80, 1993.

[138] R. H. Wade and J. Frank. Electron microscope transfer functions for partially coherent axial illumination and chromatic defocus spread. *Optik*, 49:81–92, 1977.

[139] O. Scherzer. The theorerical resolution limit of the electron microscope. *J. Appl. Phys.*, 20:20–29, 1949.

[140] R. F. Egerton. Electron energy-loss spectroscopy in the TEM. *Rep. Prog. Phys.*, 72:016502, 2009.

[141] S. J. Andersen. Quantification of the $Mg_2Si$ $\beta''$ and $\beta'$ phases in AlMgSi alloy by transmission electron microscopy. *Metall. Mater. Trans. A*, 26:1931–1937, 1995.

[142] E. Okunishi, I. Ishikawa, H. Sawada, F. Hosokawa, M. Hori, and Y. Kondo. Visualization of light elements at ultrahigh resolution by STEM annular bright field microscopy. *Microsc. Microanal.*, 15:164–165, 2009.

[143] S. D. Findlay, N. Shibata, H. Sawada, E. Okunishi, Y. Kondo, T. Yamamoto, and Y. Ikuhara. Robust atomic resolution imaging of light elements using scanning transmission electron microscopy. *Appl. Phys. Lett.*, 95:191913, 2009.

[144] P. D. Nellist and S. J. Pennycook. Incoherent imaging using dynadynamic scattered coherent electrons. *Ultramicroscopy*, 78:111–124, 1999.

[145] S. J. Pennycook. Structure determination through Z-contrast microscopy. *Adv. Imag. Elect. Phys.*, 123:173–206, 2002.

[146] K. Ishizuka. A practical approach for STEM image simulation based on the FFT multislice method. *Ultramicroscopy*, 90:71–83, 2002.

[147] R. F. Loane, P. Xu, and J. Silcox. Thermal vibrations in convergent-beam electron diffraction. *Acta Crystallogr.*, A47:267–278, 1991.

[148] C. T. Koch. *Determination of core structure periodicity and point defect density along dislocations*. PhD thesis, Arizona State University, 2002.

[149] M. Born and E. Wolf. *Principles of optics: Electromagnetic theory of propagation interference and diffraction of light, 7th edition*. Cambridge University Press, 1999.

[150] S. Uhlemann and M. Haider. Residual wave aberrations in the first spherical aberration corrected transmission electron microscope. *Ultramicroscopy*, 72:109–119, 1998.

[151] O. L. Krivanek, N. Dellby, and A. R. Lupini. Towards sub-å electron beams. *Ultramicroscopy*, 78:1–11, 1999.

[152] H. Rose. Outline of a spspherical corrected semiaplanatic medium-voltage transmission electron microcope. *Optik*, 85:19–24, 1990.

[153] M. Haider, H. Müller, S. Uhlemann, J. Zach, U. Loebau, and R. Hoeschen. Prerequisites for a $c_c/c_s$-corrected ultrahigh-resolution TEM. *Ultramicroscopy*, 108:167–178, 2008.

[154] O. L. Krivanek, G. J. Corbin, N. Dellby, B. F. Elston, R. J. Keyse, M. F. Murfitt, C. S. Own, Z. S. Szliagyi, and J. W. Woodruff. An electron microscope for the aberration-corrected era. *Ultramicroscopy*, 108:179–195, 2008.

[155] H. Chandler. *Hardness Testing*. ASM International, 1999.

[156] F. M. Smits. Measurement of sheet resistivities with the four-point probe. *Bell System Technical Journal*, 37:711–718, 1958.

[157] P. L. Rossiter. *The electrical resistivity of metals and alloys*. Cambridge University Press, 1991.

[158] B. Raeisinia, W. J. Poole, and D. J. Lloyd. Examination of precipitation in the aluminum alloy AA6111 using electrical resistivity measurements. *Mater. Sci. Eng. A*, 420:245–249, 2006.

[159] H. Kaesche. *Corrosion of metals: Physicochemical principles and current problems*. Springer, 2003.

[160] G. Svenningsen, M. H. Larsen, J. C. Walmsley, J. H. Nordlien, and K. Nisancioglu. Effect of artificial aging on intergranular corrosion of extruded AlMgSi alloy with small Cu content. *Corros. Sci.*, 48:1528–1543, 2006.

[161] M. H. Larsen, J. C. Walmsley, O. Lunder, R. H. Mathiesen, and K. Nisancioglu. Intergranular corrosion of copper-containing AA6xxx AlMgSi aluminum alloys. *J. Electrochem. Soc.*, 155:550–556, 2008.

[162] P. Hohenberg and W. Kohn. Inhomogeneous electron gas. *Phys. Rev. B*, 136:864–871, 1964.

[163] W. Kohn and L. J. Sham. Self-consistent equations including exchange and correlation effects. *Phys. Rev. B*, 140:1133–1138, 1965.

[164] G. Kresse and J. Hafner. Ab initio molecular ddynamic for liquid metals. *Phys. Rev. B*, 47:558–561, 1993.

[165] G. Kresse and J. Furthmüller. Efficiency of ab-initio total energy calculations for metals and semiconductors using a plane-wave basis set. *Comput. Mater. Sci.*, 6:15–50, 1996.

[166] D. Vanderbilt. Optimally smooth norm-conserving pseudopotentials. *Phys. Rev. B*, 32:8412–8415, 1985.

[167] J. P. Perdew, J. A. Chevary, S. H. Vosko, K. A. Jackson, M. R. Pedersen, D. J. Singh, and C. Fiolhais. Atoms, molecules, solid and surface: Applications of the genegeneral gradient approximation for exchange and correlation. *Phys. Rev. B*, 46:6671–6687, 1992.

[168] C. Ravi and C. Wolverton. First-principles study of crystal structure and stability of Al-Mg-Si(-Cu) precipitates. *Acta Mater.*, 52:4213–4227, 2004.

[169] H. X. Gao and L. M. Peng. Parameterization of the temperature dependence of the debye-waller factors. *Acta Cryst.*, A55:926–932, 1999.

[170] C. Dwyer. Simulation of scanning transmission electron microscope iimage on desktop computers. *Ultramicroscopy*, 110:195–198, 2010.